Angular correlations of dijets in ultra-peripheral Pb+Pb collisions at $\sqrt{s_{NN}} = 5.02$ TeV

By

Samuel Steed Boren

Submitted to the graduate degree program in Department of Physics and Astronomy and the Graduate Faculty of the University of Kansas in partial fulfillment of the requirements for the degree of Doctor of Philosophy.

Committee members

Dr. Daniel Tapia Takaki, Chairperson

Dr. Phil S. Baringer

Dr. Estela A. Gavosto

Dr. John P. Ralston

Dr. Stephen J. Sanders

Date defended: July 11th, 2018

The Thesis Committee for Samuel Steed Boren certifies
that this is the approved version of the following thesis :

Angular correlations of dijets in ultra-peripheral Pb+Pb collisions at $\sqrt{s_{NN}} = 5.02$ TeV

Dr. Daniel Tapia Takaki, Chairperson

Date approved: July 27th, 2018

Abstract

One of the most remarkable predictions of the physics of strong interactions, and quantum chromodynamics (QCD) in particular, is gluon saturation. It is observed that the gluon density in hadrons, such as the proton, grows with energy, or equivalently with decreasing Bjorken-x (the fraction of the hadron momentum carried by the parton). At some point this growth exceeds the unitarity limit and some new phenomena such as non-linear effects must set in. Data on the proton structure function, and on exclusive vector-meson photoproduction from the electron-proton collider HERA, which ended operations in 2007, have been inconclusive on whether or not gluon saturation has been observed. The search for non-linear QCD effects such as gluon saturation in both the proton and the nucleus is one of the main lines of research in high energy nuclear physics today.

In nuclei the quantum fluctuations ought to be stronger than in protons. Recently, it has been found that the Quark Gluon Plasma (QGP) created in nucleus-nucleus collisions at RHIC and LHC expands with very little dissipation. The quantum fluctuations of the initial state described by the overlap of two highly Lorentz-contracted nuclei traveling on light-cone trajectories are probably imprinted upon the distribution of particles created in the QGP. Without assessing these quantum fluctuations in nuclei, fundamental properties of the QGP such as its viscosity-to-entropy ratio cannot be determined to a high precision.

In this thesis we have studied, for the first time, the angular correlations of photoproduced dijets in ultra-peripheral Pb+Pb collisions at $\sqrt{s_{NN}} = 5.02$ TeV. This process has been suggested as a way to extract information of the nuclear gluon density in the

Pb target, and thus provide information about the initial state of high energy nucleus-nucleus collisions.

Acknowledgements

I would like to thank my family, friends, professors, and fellow graduate students for helping me to complete this work. Without all of you, I never would have finished.

This material is based upon work supported by the U.S. Department of Energy, Office of Science, Office of Nuclear Physics, to the University of Kansas.

Contents

List of Figures

List of Tables

Chapter 1

Introduction

Microseconds after the big bang, the universe was filled with a hot, dense state of strongly interacting subnuclear particles [1]. There is evidence that this phase of matter, the quark gluon plasma (QGP), is recreated in the high energy densities reached by ultra-relativistic heavy-ion collisions [2]. Measurements at the Relativistic Heavy Ion Collider (RHIC) and the Large Hadron Collider (LHC) are consistent with the QGP having the sheer viscosity of a perfect fluid [3]. At present the field of ultra-relativistic heavy-ion collisions focuses on measuring the QGP properties in detail. In particular, initial state properties of the nucleus at high energies must be rigorously measured to distinguish between the effects of the QGP and of the inherent properties of the nucleus.

This thesis seeks to further knowledge of initial state phenomena in heavy-ion collisions by measuring the gluon distribution within the nucleus. We have studied coherent dijet photoproduction in ultra-peripheral collisions (UPC), as the distribution of the so-called "elliptic" gluons is encoded in the angular correlation of the dijets [4]. In UPCs all interactions between nuclei are from electromagnetic or electroweak processes, thus initial state physics are easily accessible [5]. Such photo-nuclear interactions are described via the equivalent photon approximation from the Weizacker-Williams formalism [6, 7], as discussed in Chapter 2.

Before discussing the physics of ultra-peripheral collisions and that of UPC dijets, we will give an overview of the standard model of high energy physics, followed by an introduction to relativistic heavy-ion collisions and how these are connected to photon-induced interactions.

1.1 The Standard Model

At the turn of the last century, Ernst Rutherford probed the gold atom by bombarding a gold sheet with alpha-particles. The angular distribution of the scattered alpha-particles demonstrates that the mass of the atom is concentrated in a small volume, i.e, the atom is mostly empty space. Further experiments revealed that the atomic nuclei consisted of separate positively and neutrally charged particles: protons and neutrons.

Today, the Standard Model describes the fundamental particles of the universe in terms of fermions and bosons. Fermions are particles with half-integer spin, while bosons have integer-spin. Fermions must obey the Pauli Exclusion Principle: only one fermion at a time can occupy a given state. However, multiple bosons can simultaneously occupy a specific state [8]. Protons and neutrons, as subnuclear particles, contain large numbers of both fermions and bosons. Fermions and bosons have different statistical properties. Fermi-Dirac statistics describe the energy distribution of fermions. Likewise, the boson energy distribution is described by Bose-Einstein statistics [9].

Among the fermions are the leptons and the quarks. The leptons consist of the electron, muon, and tau, as well as their anti-particles. The leptons are believed to be fundamental: high energy experiments have yet to observe internal lepton-structure. Neutrinos are weakly interacting particles detected primarily through the precise measuring of missing transverse energy in the products of particle collisions. Quarks are the constituent particles of baryons, which contain three valence quarks, and mesons, which contain two valence quarks. In addition to the valence quarks are the sea quarks, which appear and disappear as quark-antiquark pairs within hadrons. The hadrons are particles made of quarks and gluons. Gluons are particles that mediate the strong nuclear force; likewise, photons mediate the electromagnetic force, and weak-gauge bosons mediate the weak nuclear force. A fourth boson, the graviton, is expected to transmit the gravitational force, but this particle has not been observed [10].

The behavior of fundamental particles is best described within the framework of quantum field theory (QTF). QFT defines a Lagrangian for fundamental particles. This Lagrangian then predicts the outcome of particle collisions. Different terms in the Lagrangian correspond to the various interactions between particles. The Standard Model Lagrangian, $\mathscr{L}_{StandardModel}$ can be broken down into three basic terms:

$$\mathscr{L}_{StandardModel} = \mathscr{L}_{EW} + \mathscr{L}_{QCD} + \mathscr{L}_{Higgs} + ..., \tag{1.1}$$

where $\mathscr{L}_{EW}$ is the electroweak Lagrangian, $\mathscr{L}_{QCD}$ is the QCD Lagrangian, and $\mathscr{L}_{Higgs}$ is the Higgs Lagrangian [10]. The most accessible approach to quantum field theory is through the use of Feynman diagrams. First, one imagines an interaction between particles. Then, one draws this process into a Feynman diagram, which is essentially a pictorial representation of exchanges between particles. The Lagrangian can be interpreted into Feynman rules. These rules describe how the Feynman diagram translates into a calculation for the quantum mechanical amplitude of the process. The quantum mechanical amplitude, in turn, is proportional to the cross section of the process. This is important because, sense the cross section is invariant between experiments, one can use it to effectively test for invariant quantities in the Lagrangian [11].

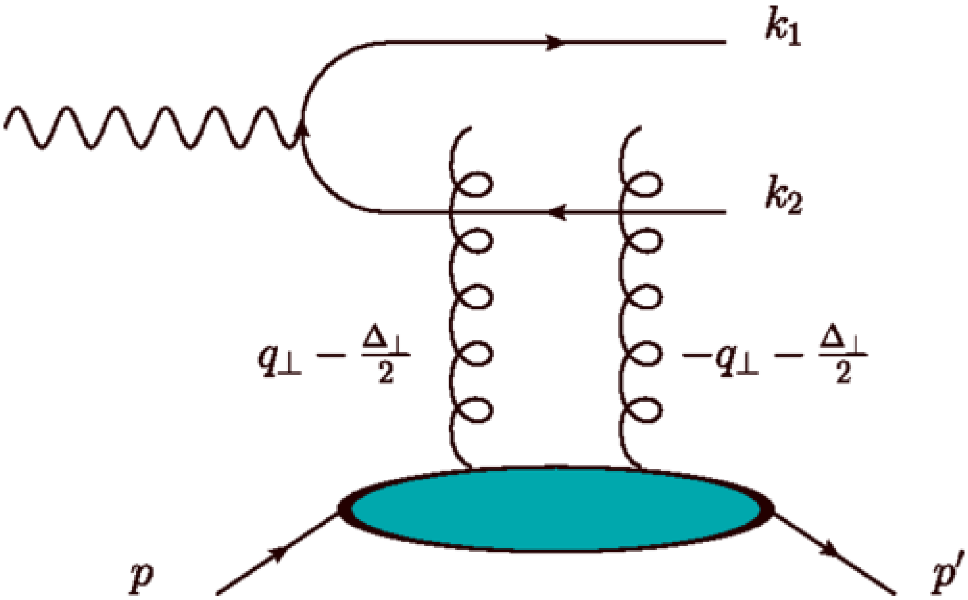

Figure 1.1: Feynman diagram of coherent dijets in dipole framework [12].

Figure 1.1 is the Feynman diagram of coherent dijet photoproduction in an photon-proton interaction. k_1 and k_2 are the four vectors of the dijets. $q_\perp$ is the average momentum of the dijets, and $\Delta_\perp$ is the proton recoil momentum. This is the Feynman diagram of the physics analysis presented in this thesis and the physics motivation for this process is discussed in Chapter 2.

1.2 Quantum electrodynamics

Quantum electrodynamics (QED) is a theory of electromagnetic interactions in terms of relativistic quantum field theory. The QED Lagrangian is

$$\mathscr{L} = \bar{\psi}(i\gamma^{\mu}D_{\mu} - m)\psi - \frac{1}{4}F_{\mu\nu}F^{\mu\nu}, \tag{1.2}$$

where ψ is spin-$\frac{1}{2}$ field, γ^{μ} are the Dirac matrices, D_{μ} is the gauge covariant derivative, m is the electron mass, and $F_{\mu\upsilon}$ is the electromagnetic field tensor [11].

QED addresses three specific processes: photon motion, electron motion, and the emission or absorption of a photon by an electron. First a Lagrangian is established based on Maxwell's laws and quantum mechanics. The photon constitutes a spin-1 solution to the differential equations derived from the QED Lagrangian. Likewise electrons are described, at non-relativistic scales, by the Schrödinger equation, and at relativistic scales by the Dirac equation. There are three processes allowed by QED: the translation of an electron, the translation of a photon, and the scattering of a photon off an electron [13].

The QED coupling constant α_{em} is approximately 1/137 at perturbative scales [14]. In general, the cross section of a given process is proportional to the $(\alpha_{em})^n$ where n is the number of vertices in the Feynman diagram. The more complex the Feynman diagram, the smaller its cross section. However, at small scales, i.e., non-perturbative momentum transfers Q^2, the coupling constant increases. α_{QED} is defined as

$$\alpha_{QED}(Q^2) = \frac{\alpha_{em}}{(1 - \frac{\alpha_{em}}{3\pi})\ln(\frac{Q^2}{m^2})}, \tag{1.3}$$

where $\alpha_{QED}(Q^2)$ is the QED coupling constant at high Q^2, and m is the electron mass [15]. High values of Q^2 are non-perturbative because, at small scales and high momentum, the fluctuation of photons into electron-positron pairs begins to saturate. Particle and anti-particle pairs can pop into existence for a short time and then annihilate so long as quantum numbers are conserved.

1.3 Quantum chromodynamics

Quantum chromodynamics (QCD) is a quantum field theory of strong interactions. The parton model, first proposed by Richard Feynman, posits that hadrons in general, and nucleons in particular, are made of more fundamental constituent particles which may or may not be the quarks implied by the SU(3) symmetry. In addition to the quarks, the partons also include any field quanta associated with nuclear forces. These field quanta are named "gluons" [16].

The quarks are a family of fermions that compose the baryons and the mesons. Baryons consist of three quarks in a color neutral state, while mesons consist a quark and an antiquark in a color neutral state. "Color" in this context refers to the six kinds of strongly interacting charge available to quarks: red and anti-red, blue and anti-blue, and green and anti-green. Color charge has no relation to optical phenomena, but provides a useful analogy for the stable combinations of quarks. The net color-charge of a baryon or meson is colorless. By way of analogy, a red quark, green quark, and blue quark can together form a hadron, in the way that conventional red, green, and blue colors can together form the color white [17].

Gluons are the QCD analogues of the photons in QED. Gluons are spin-1 and massless, but unlike photons, which do not carry electromagnetic charge, gluons carry strongly-interacting charge [18]. The QCD Lagrangian, which encodes the interactions of gluons and quarks, is

$$\mathscr{L}_{\mathrm{QCD}} = \bar{\psi}_i \left(i(\gamma^\mu D_\mu)_{ij} - m\,\delta_{ij} \right) \psi_j - \frac{1}{4} G^a_{\mu\nu} G^{\mu\nu}_a, \tag{1.4}$$

where m here represents the quark mass, the δ_{ij} is the delta function and $G^a_{\mu\nu}$ is gluon field tensor,

$$G^a_{\mu\nu} = \partial_\mu \mathscr{A}^a_\nu - \partial_\nu \mathscr{A}^a_\mu + g f^{abc} \mathscr{A}^b_\mu \mathscr{A}^c_\nu. \tag{1.5}$$

The SU(3) symmetry group of the quarks is indexed as $i, j, \ldots$; the adjoint SU(3) group, for the gluons, is indexed a, b, c. $\mathscr{A}^a_\nu$ is the gluon field, f^{abc} are the SU(3) structure constants, and g is the strong coupling [19].

Unlike QED, the QCD coupling increases with distance [20]. Figure 1.2 shows the running of the QCD coupling with Q^2:

$$\alpha_{QCD}(Q^2) = \frac{4\pi}{(11 - \frac{2}{3} n_f) \ln(\frac{Q^2}{\Lambda^2_{QCD}})}, \tag{1.6}$$

where n_f is the number of quark flavors, Q^2 is the momentum transfer, and Λ^2_{QCD} is the mass scale [21]. The running coupling has the practical consequence of the strong interactions being stronger in high momentum transfer collisions. The direct results of the running QCD coupling include the dual phenomena of asymptotic freedom and color confinement. At large distances, string tension describes the binding force of the quarks. At short distances, however, Coulomb-like interactions dominate [22]. The QCD coupling constant can be measured via the cross-section of inelastic proton-proton collisions, and also the cross section of electron-positron collisions into triple jets [23].

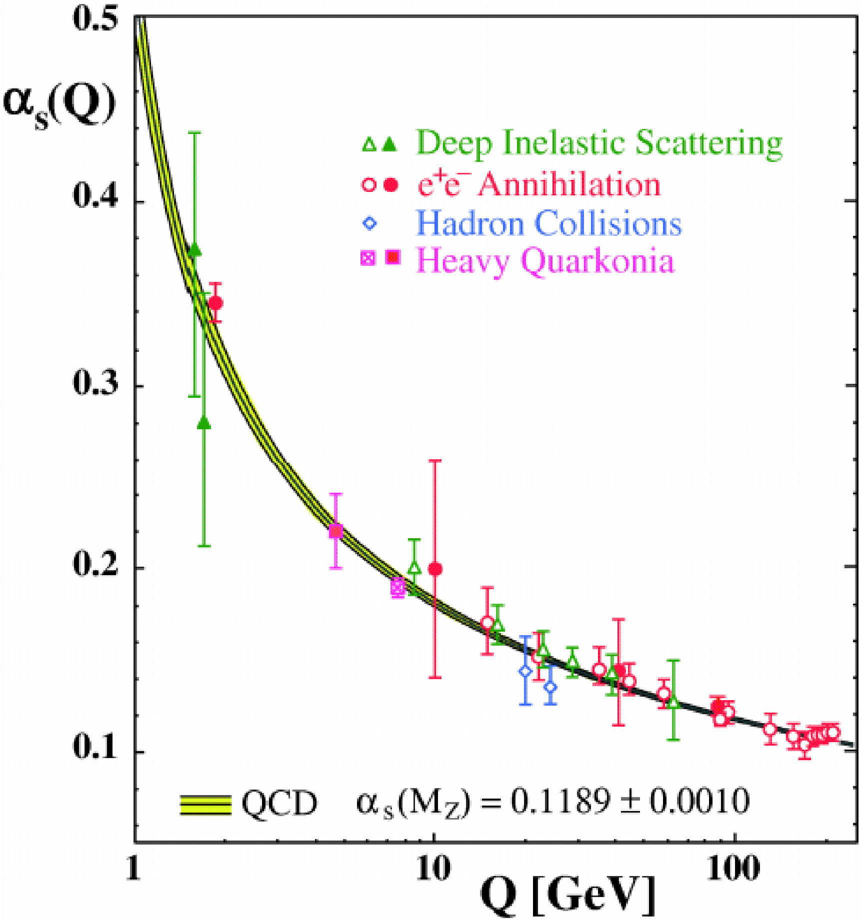

Figure 1.2: QCD coupling constant as a function of Q^2 [20].

The existence of jets is a direct result of color confinement. In hadron collisions, it is possible for the hadron's constituent partons to fragment. However, quark confinement demands that only colorless objects can independently exist. Therefore, as the partons separate, they manifest new partons around themselves and screen the color charge. The formation of colorless composites, out of colored partons, is called "hadronization". The process of hadronization continues until the kinetic energy of all the partons drops below the potential energy of the binding strong force. The result is a narrow cone of hadrons fanning out from a common source: a "jet". Analyzing a jet can elucidate the properties of its mother parton [24].

1.4 Deep inelastic scattering (DIS)

Scattering experiments are the basic tool for exploring the nucleus. In particular, DIS commonly refers to the scattering of a lepton off hadrons. For example, experiments at HERA focused on electron-proton collisions. In these collisions, the electron was used as a source of photons and neutrinos. When these particles scatter off the proton, the dependence of the collision cross section, on momentum transfer and scattering angle of the source electron, reflects the structure of the proton. The momentum transferred, Q^2, is an important quantity for characterizing DIS measurements. In addition to Q^2, Bjorken-x is necessary to describe the nuclear phase space. Bjorken-x represents the momentum fraction of partons. In lepton-proton scattering it was observed that at high momentum transfers the structure functions of the proton were functions of Q^2/υ, where Q^2 is the squared four-momentum of the virtual photon emitted by the electron, and υ is the energy lost by the electron in the collision [22]. DIS experiments provided the first evidence of two phenomena: the parton model (discussed in Section 1.3) and Bjorken-scaling.

"Scaling" is an interpretation of the data from DIS. First proposed by James Bjorken, scaling is reflected in the incoherence of photon-proton interactions at photon energies above 1 GeV$/c$ [25]. Predictions from perturbative QCD are in good agreement with DIS data from HERA, as seen in Figure 1.3 [26]. In this graph the Bjorken-x momentum fraction is designated x, and σ_r represents the F_2 structure function, and Q^2 is the transferred momentum from the electron to the proton. The order of magnitude of σ_r is set by the Bjorken-x.

At the small scales probed by high energy photons, the decreasing QCD coupling causes quarks

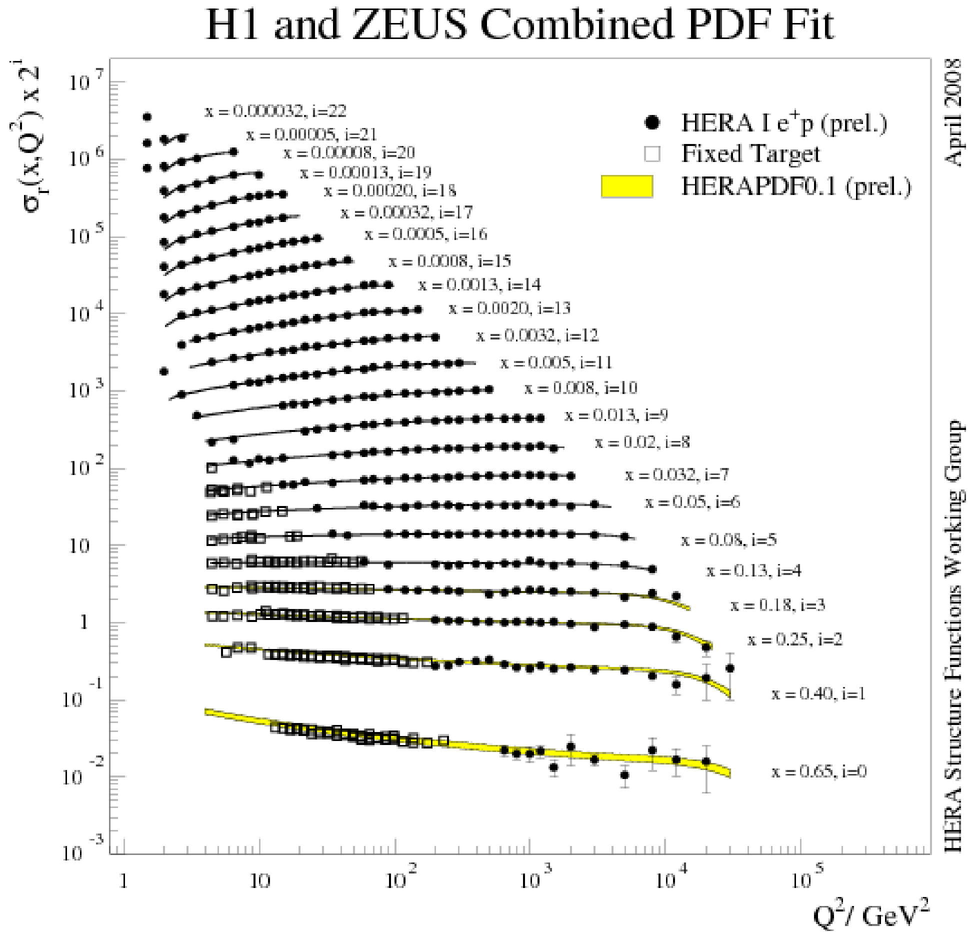

Figure 1.3: Collision cross section as a function of Bjorken-x, with data compared to HERA-PDF calculations [26].

and gluons to interact weakly. This phenomena is called "asymptotic freedom". Because gluons themselves carry color charge, the gluons about a quark tend to have an anti-screening behavior: the gluon color adds to the quark color, increasing the net color charge of the area. At smaller distances to a quark, then, there are fewer and fewer gluons augmenting the color interaction.

As discussed in Chapter 2, in UPCs at RHIC and LHC it is possible to study DIS-like processes. In particular, in the study of coherent dijets in UPCs at the LHC it is possible to access both the Bjorken-x and Q^2 dependence.

1.5 Parton Distribution Functions (PDFs)

QCD describes the interaction between quarks and gluons, but within a nucleon the calculations are too complicated to solve for the behavior of each individual parton. Theorists employ the factorization theorem to use data from DIS experiments to make predictions, as shown in Figure 1.3. The factorization theorem is discussed in greater detail later in Section 2.3. Parton distribution functions (PDFs) are a method of encoding data, mainly from DIS experiments, in the form of probability densities. PDFs give the probability of finding a species of parton with given momentum fraction, x, and a given squared energy scale, Q^2 [27–30].

In electron-proton deep inelastic scattering, the electron interacts with the proton electromagnetically by the emission of a virtual photon. This virtual photon has a four momentum q and a virtuality $Q^2 = -q^2$. When virtuality is low, the virtual photon is approximately "real"; these quasi-photons are discussed in greater detail in Chapter 2. The virtual photon, originating from the electron, interacts with a parton and changes its initial momentum fraction, x. The Q^2 of the probing virtual photon and Bjorken-x of interacting parton are determined from the collision products. The data can be used to fill out a probability density, $F_i(x, Q^2)$, of finding a parton species i at a given momentum fraction x with a probe of virtuality Q^2. The suppression factor R is the ratio of the nucleus PDF to the free proton one, without nuclear effects. Figure 1.4 shows the suppression factor of the nucleus PDF as a function of Bjorken-x [31].

One of the most interesting HERA results is that the parton density rapidly increases as the momentum fraction decreases. Conservation of momentum demands that the splintering of partons must eventually cease. The specific saturation point, where recombination begins to dominate, is a characteristic of high energy gluons within a hadron. The search for gluon saturation effects in the proton and the nucleus is one of the key lines of research in high energy heavy-ion collisions today. The Color Glass Condensate (CGC) model is one approach to describe gluon saturation [32]. Figure 1.5 shows an illustration of how the nucleus appears at varying momentum fractions [33]. In addition, PDFs model the longitudinal momentum distribution of the partons. The study of both proton and nuclear PDFs is essential for understanding final state effects produced in high energy

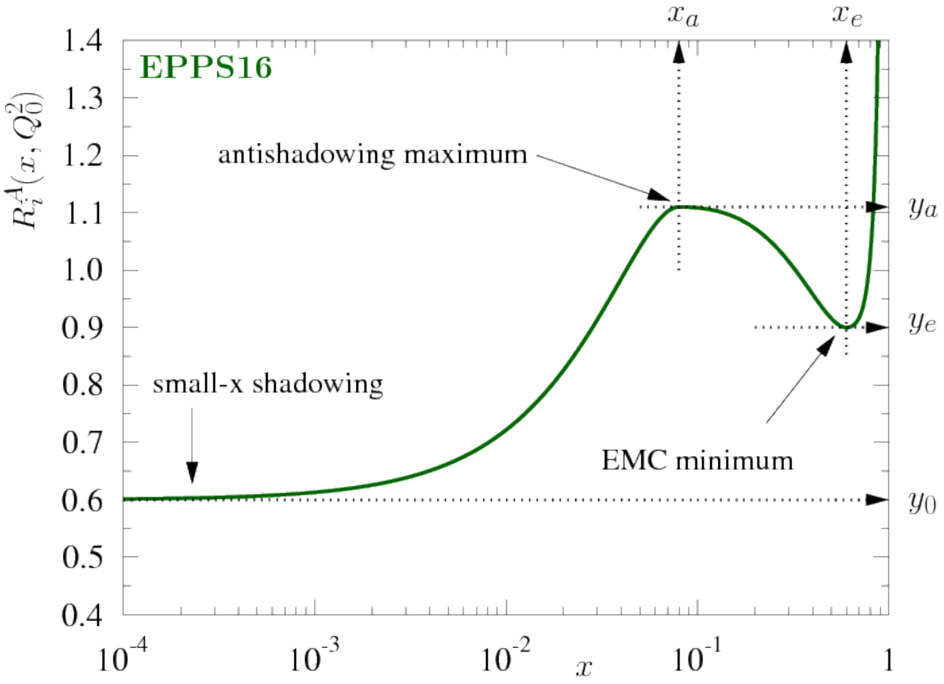

Figure 1.4: Suppression factor of nucleus PDF as a function of Bjorken-x. At different Bjorken-x and Q^2 values various nuclear effects are seen: shadowing, anti-shadowing, EMC, and Fermi motion. [31].

nucleus-nucleus collisions where the Quark Gluon Plasma can be formed. With the advent of more precise data in nuclear collisions, the PDF analyses are now supplemented by transverse momentum distributions (TMDs) and generalized parton distributions (GPDs). In addition to transverse momentum, GPDs describe the transverse spatial distribution. TMDs and GPDs are derived from the final state particles of a collision.

1.6 Quark Gluon Plasma (QGP)

From the 1980's to the 2000's, the Super Proton Synchrotron (SPS) and the Relativistic Heavy-Ion Collider (RHIC) performed heavy-ion experiments to study the possibility of deconfined plasma in a high parton density medium [34–36]. These experiments confirmed the developing model of the QCD phase space; see Figure 1.6 [37].

Essentially, quark matter organizes itself differently depending on temperature and baryon den-

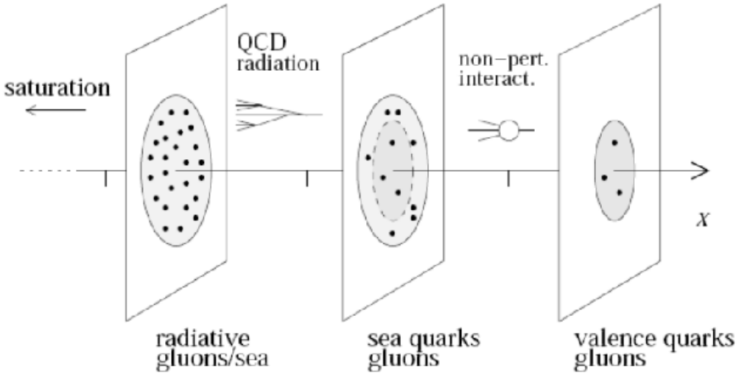

Figure 1.5: Subnuclear tomography. This figure illustrates that at higher energies the substructure of the hadron can be resolved until searching the gluon saturation regime. [33].

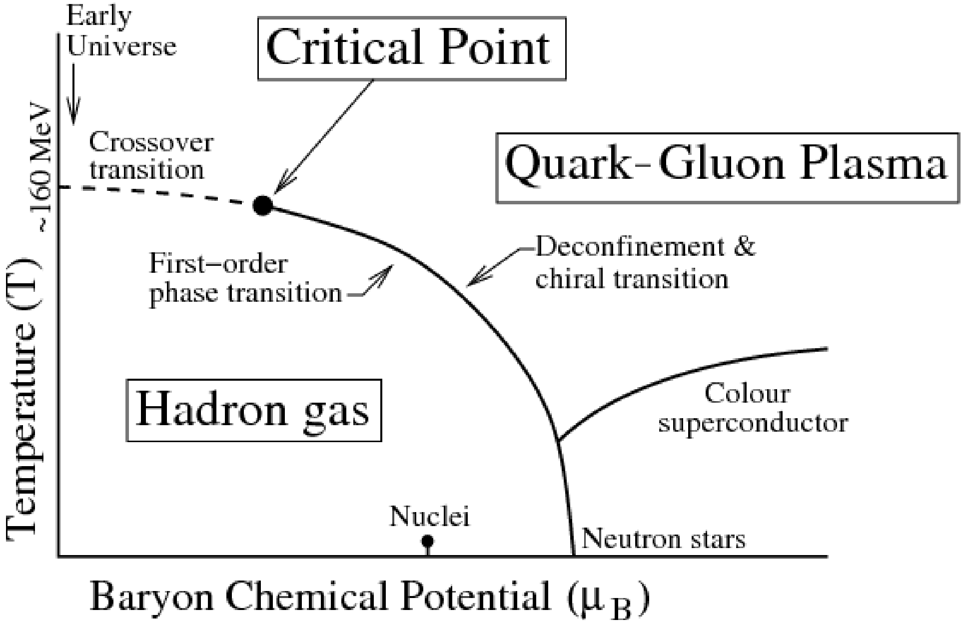

Figure 1.6: QCD phase diagram showing the temperature T as a function of baryon chemical potential μ_B (analogous to baryon density). Different phases such as the critical point, QGP, and hadron gas are seen [37].

sity. At low energies, quark matter exists in bound states: the hadrons. However, in the high energy limit, quarks and gluons take the form of a strongly interacting plasma: QGP. The QGP represents the extreme case of asymptotic freedom; the QCD coupling constant becomes small enough that quarks and gluons no longer behave as bound states. There are two ways of achieving the high energies necessary to form QGP. High baryon densities cause the quarks of separate hadrons to interact at small distances where asymptotic freedom takes effect. It is not currently possible to achieve these densities in laboratory experiments, though this state is thought to occur in neutron stars. By contrast, particle colliders like the LHC increase the energy density by colliding heavy-ions at ultra-relativistic velocities. The high temperature environment produces QGP. The early universe, mere milliseconds after the Big Bang, is thought to have existed as QGP [38].

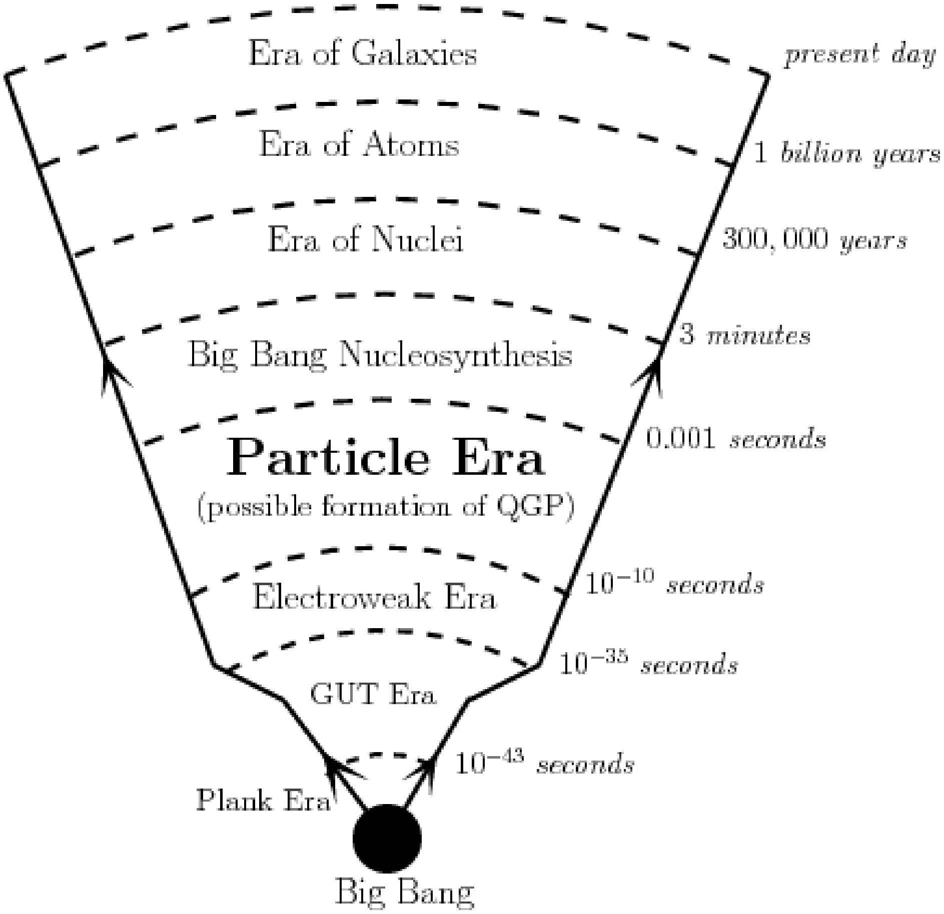

Figure 1.7: Pictorial time-line of the Universe, showing the various phase transitions, including the appearance of the QGP phase where quarks and gluons are present in a deconfined state [39].

Figure 1.7 is a simplified cosmological time-line. In the first hundred or so microseconds after the Big Bang, the universe was small, dense, and highly energetic [39]. The energy density of the early universe would have been in excess of 1 GeV$/(fm)^3$. Note that 1 GeV$/(fm)^3$ is the energy density at which QGP is thought to form. The universe cools and hadrons form out of the quarks and gluons. The protons and neutrons condense into nuclei. The positively charged nuclei gather negatively charged electrons, forming the atoms that in cosmic time become stars [40].

There are a number of experimental signatures of QGP formation. Thermal physics understands phase transitions as occurring at specific temperatures and densities. At the boundary between two phases, one can define a critical point at which there is a discontinuous change in the behavior of observables. For the SPS heavy-ion programs the main observables were charm suppression and strangeness enhancement, while for the RHIC heavy-ion experiments the studies focused on elliptic flow, and jet quenching [41–43].

Figure 1.8 shows the suppression of J/ψ meson production with respect to Drell-Yan scattering in PbPb collisions at the SPS [34]. The QGP is thought to suppress the production of J/ψ mesons in heavy-ion collisions, as seen at SPS, RHIC and LHC, although at the LHC the QGP has also been found via a recombination mechanism to enhance the J/ψ yield at low p_t and forward rapidities.

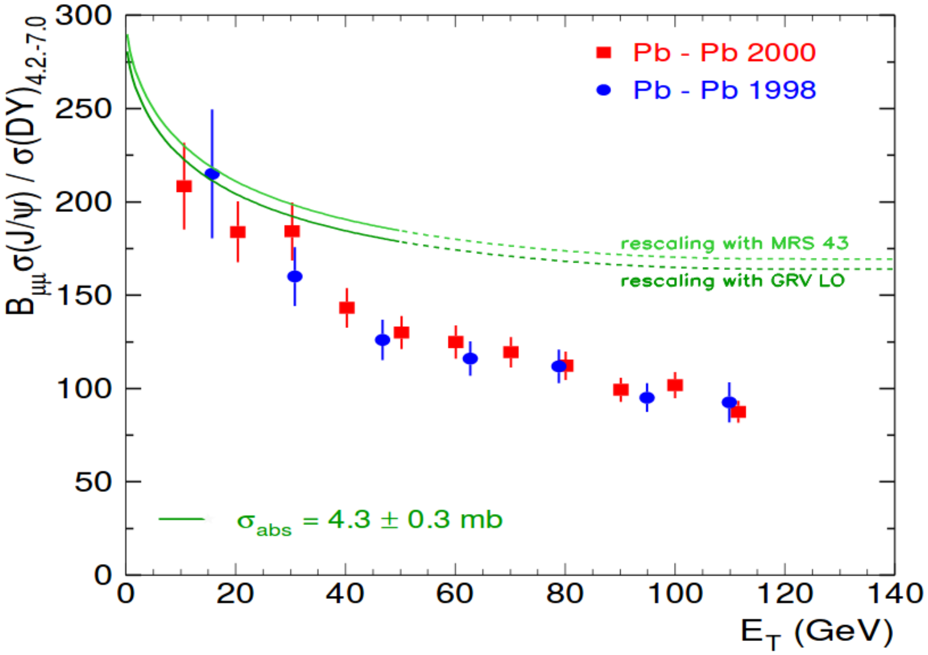

Figure 1.8: J/ψ suppression as a function of transverse energy E_T in Pb-Pb collisions at SPS. Data from different periods are shown and compared to theories that do not incorporate QGP [34].

At RHIC, it was demonstrated that heavy-ion collisions can produce a state of hadronic matter, often referred to as "the medium", that exhibits elliptic flow. The predicted viscosity of the QGP would cause elliptic flow in the overlap region of heavy-ion collisions [44]. The angular correlations of the final state particles, produced by heavy-ion collisions, were analyzed and shown to be consistent with the medium flowing as a nearly ideal fluid [45]. "Ideal fluid" refers to how the high temperature nuclear medium can be modeled by hydrodynamic equations in which the shear viscosity is extremely low [46]. As the QGP is a perfect fluid, the initial state properties of the heavy-ion will propagate through the collision and have a significant effect on the final state particles. The angular distribution of final state particles can be modeled using Fourier series,

$$1+\sum_{n=1}^{\infty} 2v_n \cos\left[n\left(\phi-\Psi\right)\right], \tag{1.7}$$

where n is the order of the Fourier expansion, v_n is the Fourier coefficient, ϕ is the azimuthal angle, and Ψ is the event-plane angle. The second order term, v_2, is referred to as "elliptic flow" and is predicted to quantify the pressure gradient of the overlap-region in the heavy-ion collision. Figure 1.9 is an illustration of the overlap region of a heavy-ion collision. Because the pressure gradient is higher for the short axis than for the long axis, the nuclear medium in the overlap region will flow outward along the short axis, and this is reflected in the alignment of the tracks in the direction of the flow [47–53].

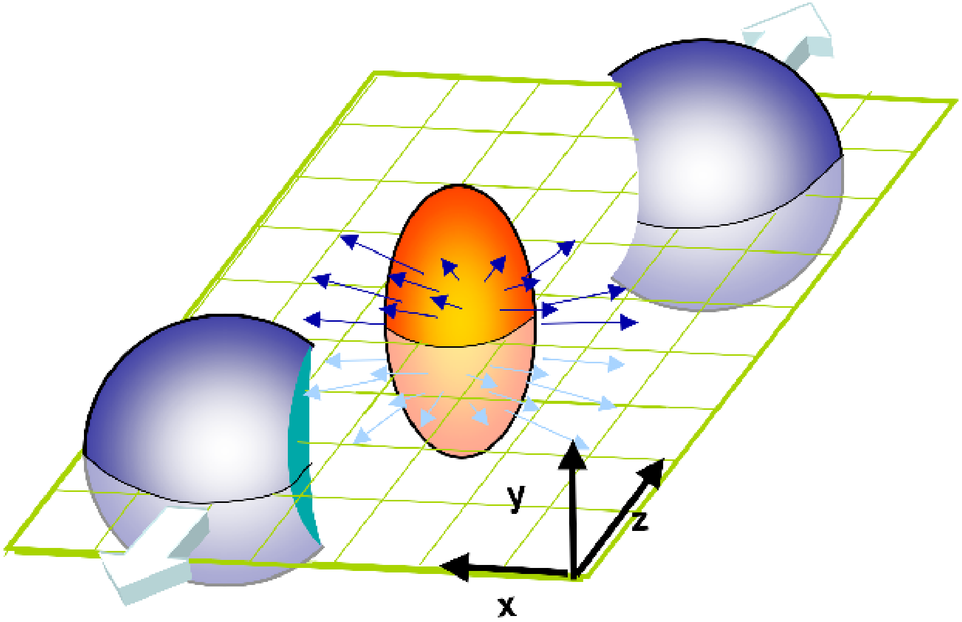

Figure 1.9: Heavy-ion overlap region, showing the elliptic flow produced [54].

A highly viscous medium will resist deformation such that the shape of the overlap region, i.e. its ellipticity, will not necessarily carry over to the final-state tracks. However, because the QGP medium is a nearly ideal liquid, the elliptic correlation of the final-state should arise from that of the initial-state. The RHIC result emphasizes the great importance of a precisely understood heavy-ion initial state. Figure 1.10 compares the v_2 elliptic flow results from various heavy-ion experiments [34].

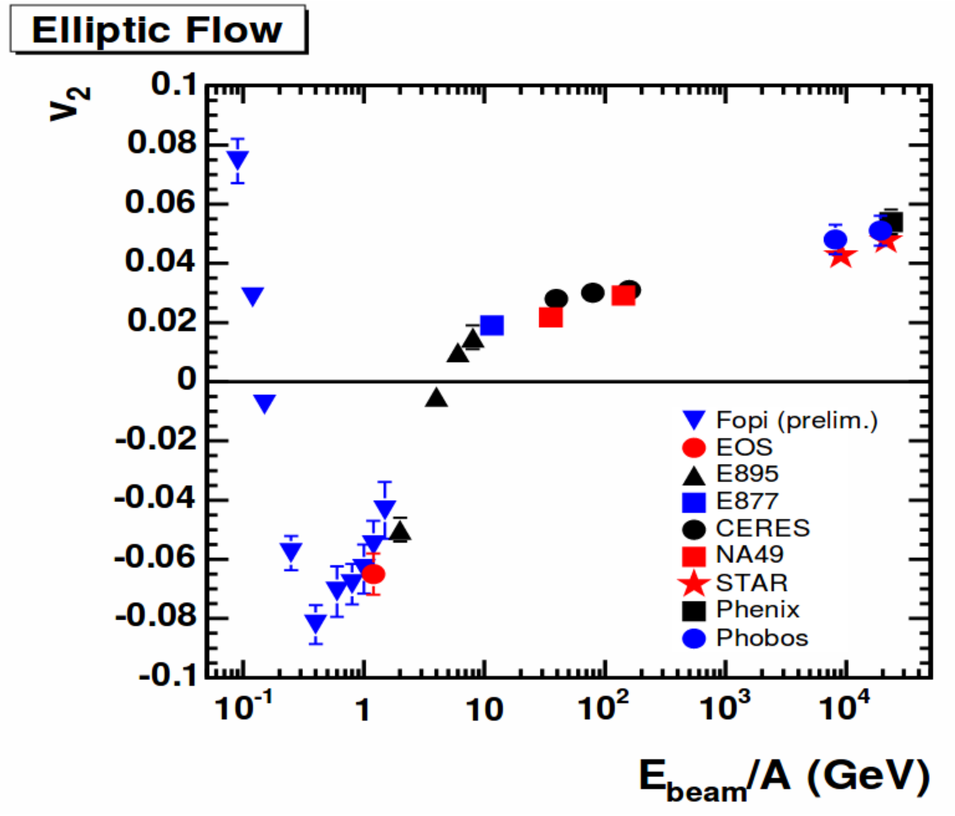

Figure 1.10: v_2 as a function of collision energy for various heavy-ion experiments [34].

The phase transitions from a hot, dense medium to stable hadrons are seen in heavy-ion collisions, as illustrated by Figure 1.11 [55]. The y-axis represents time, and the x-axis represents the longitudinal separation of the ions. Notice that after the ions cross, there is a "cascade" during which the partons take on thermal energy until reaching a critical temperature for QGP formation. The hadron gas passes through two temperature "freeze-outs". Particles stop forming at the chemical freeze-out temperature. These particles stop exchanging kinetic energy after cooling beyond the "kinetic freeze-out" [56].

Lastly, another remarkable signature for the formation of the QGP is that related to “jet quench-

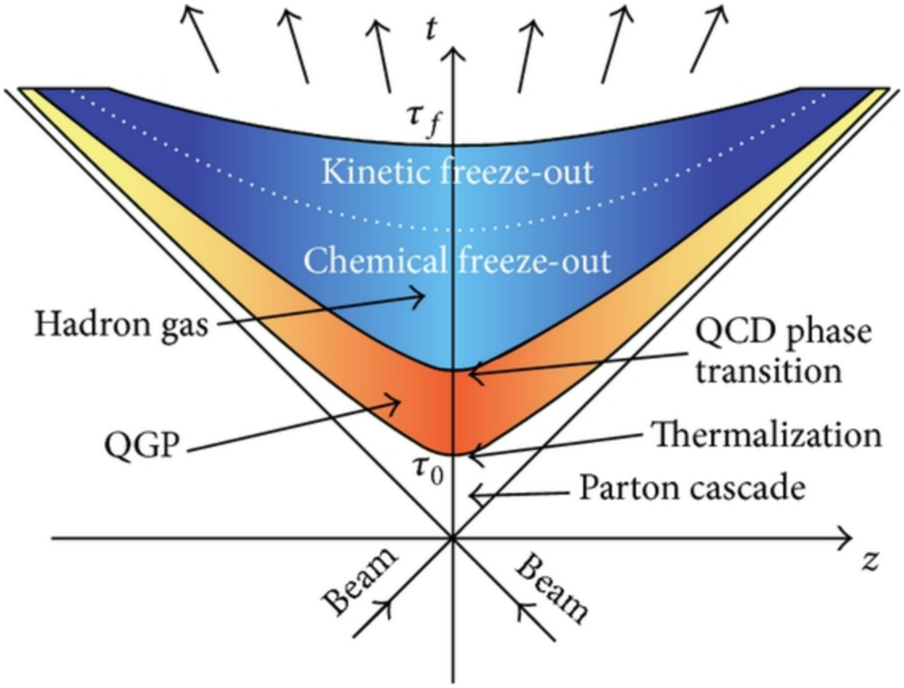

Figure 1.11: Space-time diagram of a heavy-ion collision [55].

ing". Inclusive hadronic jets would interact strongly with the QGP; therefore, dijets will have significant energy imbalance depending on the multiple interactions of the components jet with the QGP. All of these QGP signatures, elliptic flow, quarkonia suppression and even jet quenching require a good understanding of the heavy-ion initial state as a basis for comparison [57], making a compelling case for studying the initial state to a high precision.

The Large Hadron Collider (LHC) stands at the forefront of high energy nuclear physics research. The LHC is capable of reaching heavy-ion collision energies of up to 7 TeV per nucleon, which is sufficient energy for a QGP to be formed and to last long enough to measure its properties [58–60], and a plethora of interesting physics processes are being studied using the various experiments. In the next chapter, we will introduce how the LHC can be used as a photon-induced collider and how that collision model serves to search for high-energy QCD phenomena.

Chapter 2

Ultra-peripheral collisions and photoproduction

In this chapter, we will review recent LHC results on ultra-peripheral collisions (UPCs). First we will discuss the unique features of UPCs, and how they are selected. We then present the results from ALICE and CMS on vector meson photoproduction as an example of how UPCs can probe the nuclear gluon distribution. The final section explains dijet photoproduction in UPCs, and how the factorization theorem informs the interpretation of coherent dijet correlations. Finally, we present the physics motivation to study the angular correlation of UPC dijets, which is the analysis presented in this thesis.

2.1 Ultra-peripheral heavy-ion collisions

Ultra-peripheral collisions occur at impact parameters greater than the sum of the heavy-ion radii. In these collisions, hadronic interactions are strongly suppressed while photonuclear activity is enhanced proportional to the square of the nuclear charge [5]. The electromagnetic field of an incoming heavy-ion, from the perspective of a target, is equivalent to a flux of virtual photons; Figure 2.1 illustrates the Lorentz contraction of the field of a boosted charge [61, 62].

UPC models typically address two elements: the photon flux, $N_{\gamma/Pb}$, and the photoproduction cross-section, $\sigma_{\gamma Pb}$. These quantities are related to the UPC cross-section, σ_{PbPb}, in the following equation

$$\frac{d\sigma_{PbPb}}{dy} = N_{\gamma/Pb}(y,M)\sigma_{\gamma Pb}(y) + N_{\gamma/Pb}(-y,M)\sigma_{\gamma Pb}(-y), \tag{2.1}$$

where there are two terms to reflect that either heavy-ion can be a source of photons [63].

The Weizsacker-Williams approximation (WWA) calculates the density of photons, about the

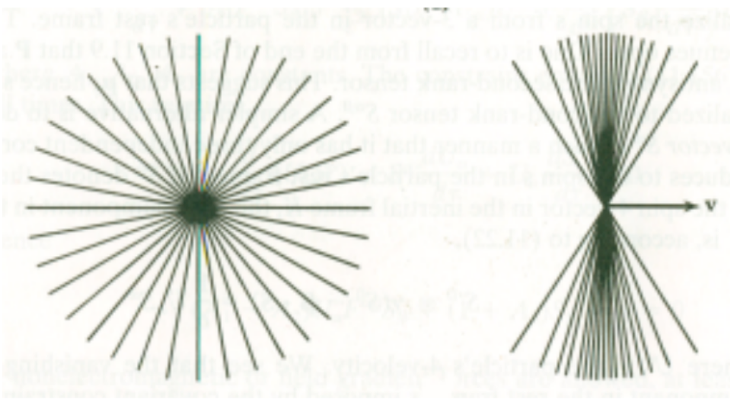

Figure 2.1: (a.) Electromagnetic field of a stationary charge (b.) electromagnetic field of a boosted charge [62].

nucleus, as a function of energy. WWA is a semi-classical formulation. Maxwell's equations are solved for a stationary point charge boosted to an ultra-relativistic velocity. In the target's frame, the Fourier transform of the source field is taken. The Fourier frequency modes are interpreted through the quantum mechanical equation of photon energy. The photon flux as function of energy is given by

$$N(\omega,b)=\frac{\alpha}{\hbar\omega}\left(\frac{Z}{b\beta\pi}\right)^{2}\left(\frac{\omega b}{\gamma v}\right)K_1^2\left(\frac{\omega b}{\gamma v}\right), \tag{2.2}$$

where α is the QED coupling constant, ω is the photon frequency, Z is the atomic number of the nuclei, b is the impact parameter, β is the ratio of the nuclei speed to the speed of light, γ is the Lorentz boost of the nuclei, K_1^2 is a Bessel function, and v is the velocity of the projectile nucleus [62].

For a given final state X, the collision cross section is given as

$$\sigma_X=\int d\omega\frac{n(\omega)}{\omega}\sigma_X^{\gamma}(\omega), \tag{2.3}$$

where $n(\omega)$ is the number of photons emitted at an energy ω, and $\sigma_X^{\gamma}(\omega)$ is the photonuclear cross-section of the photon-nucleon interaction. The Weizacker-Williams approximation provides $n(\omega)$. The integral reflects how a state X can result from the interaction of a quasi-real photon of varying energy [64]. At low momentum transfer, photons interact electromagnetically, i.e. directly, with partons [65]. High energy, "resolved" photons possess a hadronic structure; instead of directly interacting with the nuclei, these photons fluctuate into mediating quark-antiquark pairs.

UPCs can generate a wide variety of particles from photon-hadron interactions. In the next section we will discuss current results on vector meson photoproduction.

2.2 Vector meson photoproduction

The vector mesons (VM) are a subset of the mesons that have spin-1 and negative parity. There are three vector mesons that have recently been studied in UPCS: the ρ^0, the J/ψ, and the $\Upsilon(1S)$. The ρ^0 is an antisymmetric superposition of up and down quark-antiquark pairs, $(1/\sqrt{2})(u\bar{u}-d\bar{d})$. The J/ψ consists of a charm quark and a charm antiquark. The $\Upsilon(1S)$ consists of a bottom quark and a bottom antiquark. J/ψ and its excited states are referred to as charmonia; likewise, $\Upsilon(1S)$ and its excited states are referred to as bottomonia.

The Bjorken-x probed by a specific UPC vector meson is set by the mass M_{VM}, the rapidity y, and collision energy $\sqrt{s}$, such that

$$x = \frac{M_{VM}}{\sqrt{s}} e^{\pm y}. \tag{2.4}$$

The vector meson mass also sets the hard scale, Q^2, of the photoproduction. For example, for the J/ψ:

$$Q^2 = \frac{M_{J/\psi}}{4}. \tag{2.5}$$

The virtual photons present in an UPC can fluctuate into a quark-antiquark pair which can take the form of a low mass meson [66–68]. This meson then interacts with the target nuclei via colorless gluon exchange, emitting a vector meson [69–72]. If the virtual photon interacts coherently with the target nucleus, this is reflected in the transverse momentum of the vector meson [73]. The vector meson decays into a dilepton pair that can be detected by the experiment.

One of the first observations of vector meson photoproduction in UPCs was that of exclusive coherent ρ^0 production at STAR. For this process the source nucleus emits a virtual photon that fluctuates into a ρ^0 meson that scatters elastically off the target nucleus. The ρ^o decays into a pair of oppositely charged pions. These pions leave two back-to-back tracks in the STAR tracker. The Feynman diagrams for the process are seen in Figure 2.2. In exclusive production there are only

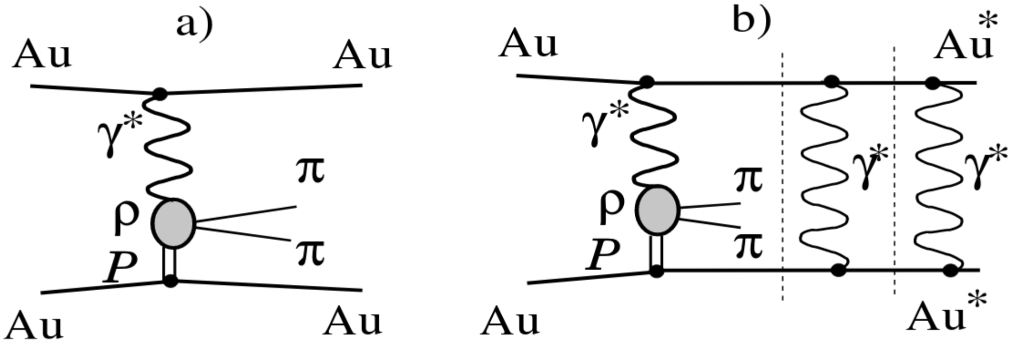

Figure 2.2: $AuAu \rightarrow AuAu\rho^o$, (a.) UPC exclusive ρ^o diagram, (b.) with mutual nuclei excitation [74].

two tracks in the tracker, with the rest of the detector being empty. In mutual nuclei excitation, the further exchange of virtual photons excite both nuclei and produce tracks in addition to those of the dipion system. The exclusive events were selected by STAR using a low-multiplicity trigger, while the mutual excitation events were selected using a minimum bias trigger with the additional requirement of neutron emission detected in both ZDCs [74].

One of the key signatures of coherent ρ^0, and UPC coherent mesons in general is their low p_T. If the virtual photon has k of the order of $1/2R_A$, where R_A is the radius of the nuclei, the photon couples with the whole nucleus. The low momentum corresponds to a large wavelength of the photon with respect to the nuclear radius [75–78]. The p_T spectrum of the ρ^0 detected by the topology and minimum-bias triggers is shown in Figure 2.3, where the low p_T ρ^0 candidates are consistent with coherent photoproduction for the two different triggers. STARLIGHT is a Monte Carlo generator designed to model vector meson photoproduction in UPCs [79].

More recently, ultra-peripheral coherent J/ψ photoproduction was studied by the ALICE and CMS collaborations using the 2011 Pb-Pb data [80]. Figure 2.4 shows the dimuon invariant mass and p_T from the decay of coherent J/ψ from CMS [81]. Before discussing the J/ψ data in UPC PbPb, it is important to notice that the cross section for coherent J/ψ photoproduction, for $\gamma + p \rightarrow J/\psi + p$, has a power-law dependence on the photon-proton center-of-mass energy, as seen in Figure 2.5 [82]. Such data can be sensitive to the gluon distribution in the proton as a function of Bjorken-x [83].

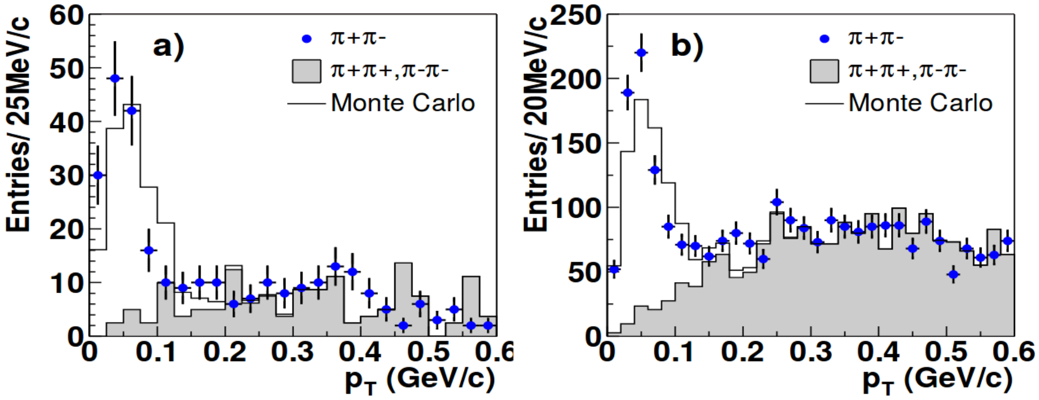

Figure 2.3: UPC exclusive ρ^o p_T from the STAR experiment, (a.) topology triggered (b.) minimum bias triggered [74].

In the nucleus-nucleus collision, the UPC J/ψ photoproduction cross section can be calculated using the impulse approximation of the heavy-ion [85]. The impulse approximation depicts the nucleus as a sum of protons and neutrons by scaling up the photon-nuclear cross section derived from electron-proton collisions at HERA and at the LHC [86].

Studies of UPC J/ψ production by the ALICE and CMS collaborations show that the measured cross section is consistent with models of the nucleus that include moderately strong gluon shadowing, in particular EPSO9 [87, 88]. Figure 2.6 compares the cross sections measured by ALICE and CMS against theoretical models. The data show a clear difference from the impulse approximation prediction. The cross sections indicate that, at the energy scale of the J/ψ mass, the nuclear gluon density is suppressed with respect to that of the proton [89]. Further studies can be done using UPC Υ production; although this is less sensitive to nuclear shadowing due to its higher Q^2 values [90, 91]. Recently, the ALICE and CMS data have been used to calculate the nuclear suppression factor, which is equivalent to the nuclear PDF calculation as a function of Bjorken-x discussed in Section 1.5. The LHC data provide evidence for nuclear gluon shadowing at low Q^2 and low Bjorken-x. Figure 2.7 shows ratio S_{Pb} of the Pb PDF to the proton PDF, as a function of Bjorken-x, with data from ALICE and CMS compared to theoretical models of nuclear shadowing [92]. This is the first experimental evidence that the Pb nucleus presents shadowing effects at high energies.

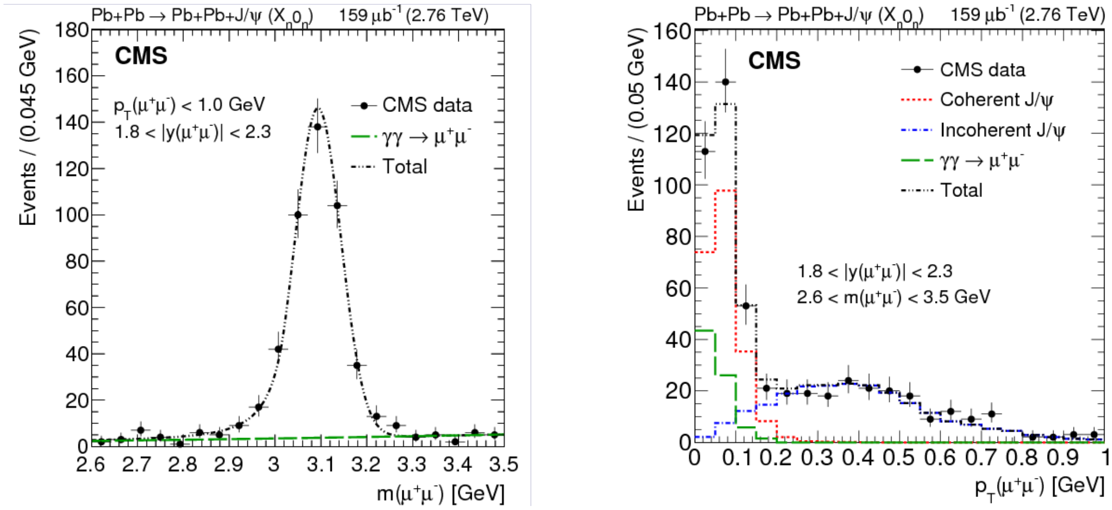

(a) (b)

Figure 2.4: (a) Dimuon invariant mass spectrum, (b) dimuon p_T spectrum for J/ψ candidates. The data has been compared to the STARLIGHT MC [81].

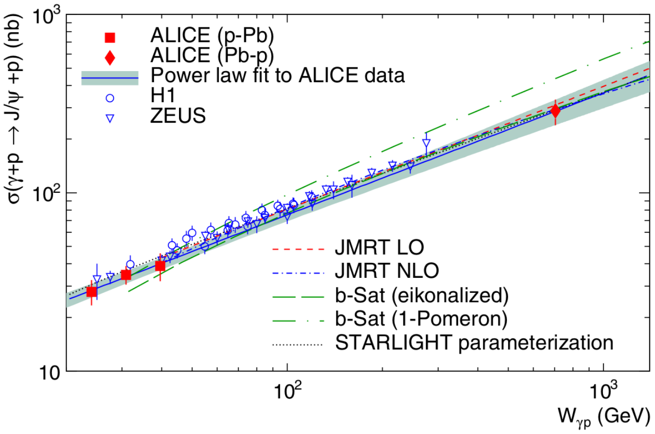

Figure 2.5: γ+proton$\rightarrow$ J/ψ+proton cross section, showing the ALICE and HERA data [84].

It is also interesting to note that the use of forward neutron tagging can be used to separate the coherently and incoherently produced J/ψ mesons [93–99]. This is one of the ongoing lines of research, which is important for measuring the incoherent photoproduction cross section and its energy dependence.

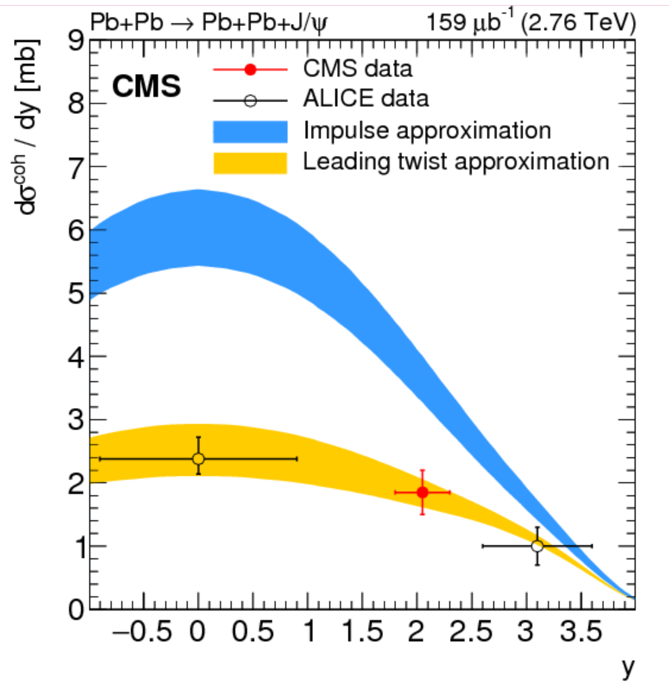

Figure 2.6: Differential cross section versus rapidity for coherent J/ψ photoproduction in ultra-peripheral PbPb collisions at $\sqrt{s_{NN}} = 2.76$ TeV. Data are compared to theories incorporating the impulse approximation and the leading twist approximation [81].

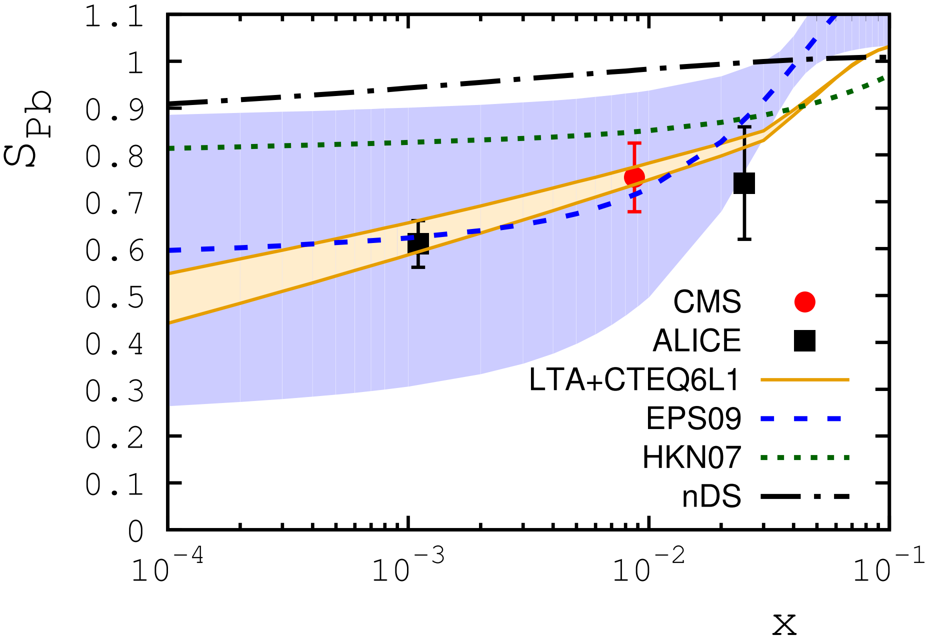

Figure 2.7: Suppression factor of Pb PDF as a function of Bjorken-x. Theoretical models are compared to ALICE and CMS data [92].

2.3 Dijet photoproduction

Preliminary results on inclusive dijet production in ultra-peripheral collisions at $\sqrt{s_{NN}} = 5.02$ TeV by the ATLAS experiment exits, while there are no results on coherent dijet photoproduction. Rather than introducing the preliminary ATLAS data which is not related to this analysis, we will introduce similar studies by the HERA experiment; first, because it will allow us to discuss the difference between direct and resolved photo-induced production, and because it shows that RAPGAP, the Monte Carlo event generator, used in this analysis has been successfully used to describe the HERA data.

Photon-nuclear interactions fall into two groups: direct and resolved. In a direct photon process, the virtual photon Q^2 is low enough that virtuality goes to zero. The virtual photon thus interacts with the nucleus as a real photon. Coherent production is the subset of direct photon production for which the proton remains intact. On the other hand, resolved photon processes have high Q^2 such that the virtual photon manifests a hadronic structure, fluctuating into quarks and gluons before interacting with the target nucleus. Because this virtual photon generates partons, the fraction of the photon's 4-momentum that enters into the hard scattering process is less than in direct production. These two processes have been studied systematically at HERA, finding an experimental evidence for the transition from the soft to the hard diffractive regime. In particular, the photoproduction of dijets has been studied in a systematic manner at HERA to extract information about the proton and photon structure, and for determining the strong running constant α_s.

In electron-hadron collisions, diffractive photoproduction is characterized by the presence of a large rapidity gap in the final state and an intact nucleus [101–103]. The Feynman diagram of electroproduction in lepton-hadron collisions is similar to that of photoproduction in ultraperipheral collisions, as seen in Figure 2.8 [100]. The large rapidity gap here is due to the leading proton [104]. The diffractive dijet cross section is expressed by the convolution of partonic cross sections $d\hat{\sigma}$ and diffractive PDFs $f^D_{i/p}$;

$$d\sigma(ep \to e + 2jets + X^{'} + p) = \sum_i \int dt \int dx_{\mathbb{P}} \int dz_{\mathbb{P}} d\hat{\sigma}_{ei\to 2jets}(\hat{s}, \mu_R^2, \mu_F^2) \times f^D_{i/p}(z_{\mathbb{P}}, \mu_F^2, x_{\mathbb{P}}, t), \tag{2.6}$$

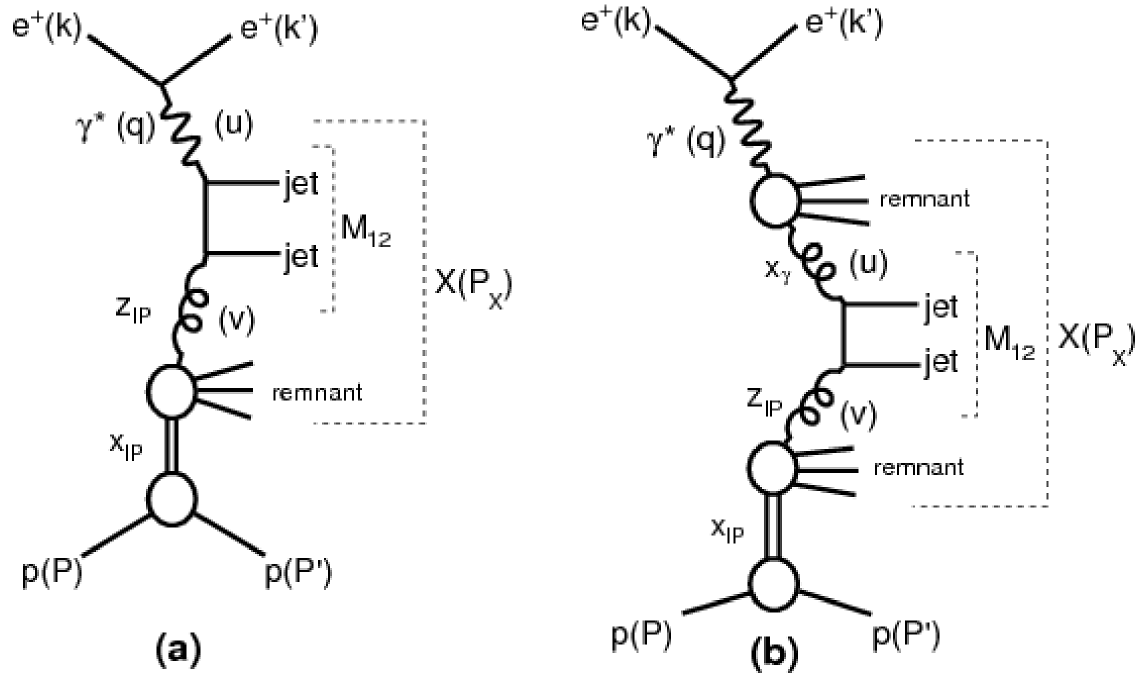

Figure 2.8: Feynman diagrams for coherent jet photoproduction in (a) direct photon in ep interactions, (b) resolved photon in ep interactions. [100].

where $x_{\mathbb{P}}$ is the longitudinal momentum fraction lost by the incoming proton, $d\hat{\sigma}_{ei\rightarrow 2jets}$ is the partonic cross-section for the process, $z_{\mathbb{P}}$ is the longitudinal momentum fraction of the Pomeron entering the hard process, $\hat{s}$ is the squared invariant energy of the subprocess, μ_R^2 is the squared renormalization scale, μ_F^2 is the squared factorization scale, $f_{i/p}^D$ is the diffractive parton distribution, and t is the four-momentum transfer squared at the vertex.

In the proton-vertex factorization hypothesis, the dependence on $x_{\mathbb{P}}$ and $|t|$ is factored out of the dependence on μ_F^2 and $z_{\mathbb{P}}$. Furthermore, $f_{i/p}^D$ is sum of contributions from the Pomeron and Reggeon:

$$f_{i/p}^D(z_{\mathbb{P}},\mu_F^2,x_{\mathbb{P}},t) = f_{\mathbb{P}/p}(x_{\mathbb{P}},t)f_{i/\mathbb{P}}(z_{\mathbb{P}},\mu_F^2) + n_{\mathbb{R}}f_{\mathbb{R}/p}(x_{\mathbb{P}},t)f_{i/\mathbb{R}}(z_{\mathbb{P}},\mu_F^2), \qquad (2.7)$$

where $_{\mathbb{P}/p}$ is the Pomeron flux factor, $f_{\mathbb{R}/p}$ is the Reggeon flux factor, $n_{\mathbb{R}}$ is the normalization factor of the Reggeon, $f_{i/\mathbb{P}}$ is the Pomeron parton distribution, and $f_{i/\mathbb{R}}$ is the Reggeon parton distribution. Figure 2.9 compares the cross-section of H1 data to that predicted by next-to-leading-order QCD [100]. The H1 data were compared to predictions based on NLO-QCD convoluted with diffractive parton distribution functions (DPDFs) from HERA inclusive diffractive deep-inelastic scattering (DDIS) data. For diffractive pp collisions the high transverse momentum jets yield a hard scale for perturbative QCD [105].

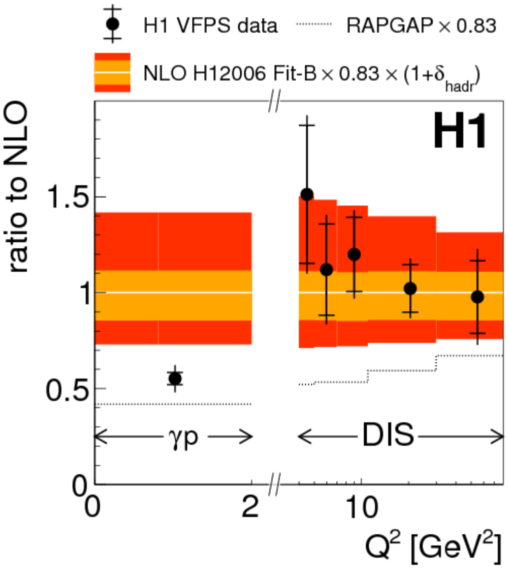

Figure 2.9: Ratio of H1 measured cross section to NLO-QCD cross section [100].

Before concluding with this section, more comments about the HERA analysis are given. First, H1 used their Very Forward Proton Spectrometer (VFPS) to trigger on low Q^2 protons. The VFPS consists of two Roman Pots located 218 m and 222 m from the H1 interaction-point in the forward direction. The VFPS can detect protons scattered at very low transverse momentum, corresponding to $0.008 < x_P < 0.028$ and $|t| < 0.6$. Each of the Roman Pots contains layers of scintillating fibers, which are covered by a layer of scintillator tiles. The fibers readout to photomultipliers, and the tiles both protect the electronics from beam-radiation damage and trigger on protons. The track efficiency of the VFPS is a remarkable 96%, and the background contamination is kept at 1% , making the detector excellent for studying diffractive events [100].

H1 used the RAPGAP MC generator to model diffractive $e + p \rightarrow e + X + p$ processes. The requirement of a leading proton, remaining intact or dissociating into a low energy state, was used to sample diffractive events. The collision product kinematics of data and MC are shown in figure 2.10. Not only are the data in good agreement with predictions from RAPGAP, but the cross section of diffractive $e+p$ scattering is well described by calculations based on DPDFs. For this process, β refers to the fraction of the Pomeron's longitudinal momentum transferred to the parton within the nucleus [104].

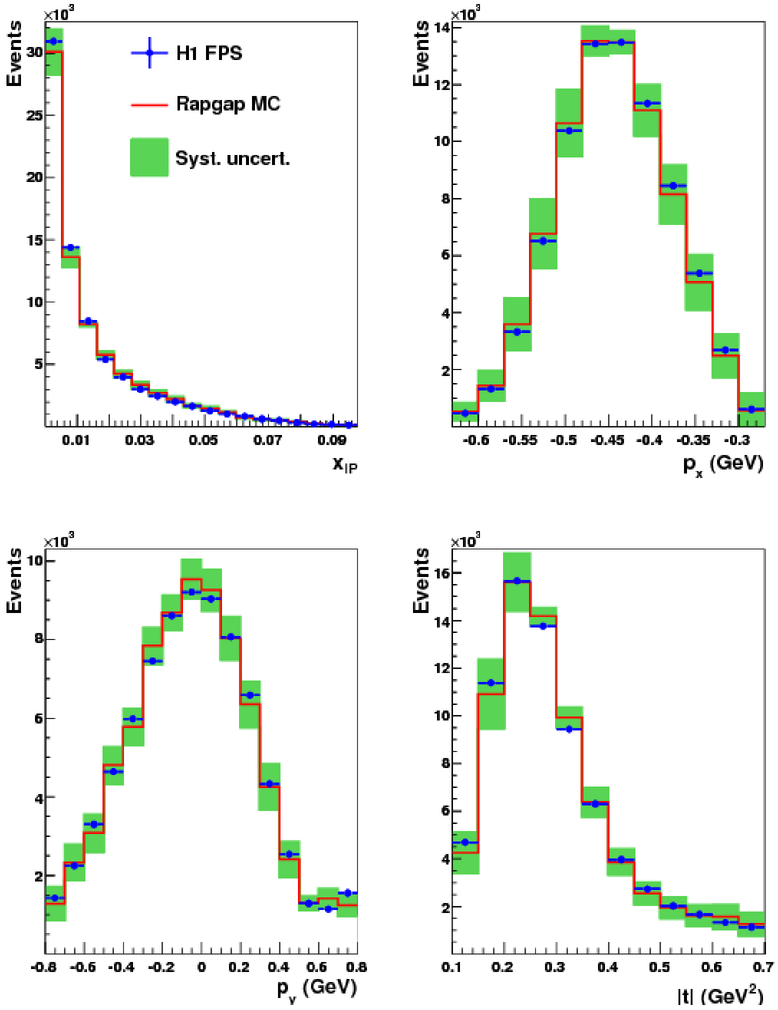

Figure 2.10: H1, diffractive $e+p$ products, kinematics [104].

2.4 Wigner gluon distribution

The coherent dijet data can be used to extract information about the so-called Wigner gluon distribution. The Wigner distribution was first developed as part of an attempt by Eugene Wigner to map solutions to Schrödinger equation into phase probability distributions, yielding a statistical mechanics interpretation of quantum mechanics. Consider the Wigner distribution $P(x,p)$,

$$P(x,p) \overset{\text{def}}{=} \frac{1}{\pi\hbar}\int_{-\infty}^{\infty} \psi^*(x+y)\psi(x-y)e^{2ipy/\hbar}\,dy \tag{2.8}$$

which can be used to calculate the expectation value of any given variable by considering the Wigner transformation $g(x,p)$ of that variable's operator, $\hat{G}$,

$$\langle\hat{G}\rangle = \int dx\,dp\,P(x,p)\;g(x,p)\;. \tag{2.9}$$

Notice that in order to derive expectation values, the probability distribution must be integrated with respect to a function of position or momentum, which are still non-commuting according to the uncertainty principle.

The Wigner distribution is a quantum phase space distribution that describes "elliptic" gluons [106]. Specifically, by considering the color dipole scattering amplitude, the angular correlation of the nucleon recoil momentum and the dijet transverse momentum can provide a three-dimensional, tomographic image of the gluons within a high energy nucleus. This tomographic image takes the form of a Wigner distribution, which contains all the information of both the transverse-momentum-dependent parton distributions (TMDs) and the generalized parton distributions (GPDs) without violating the uncertainty principle. Specifically, the angular correlation directly measures the Fourier transform of the gluons. This is possible because the dipole amplitudes are functions of the impact parameter, and because collinear factorization holds.

TMDs and GPDs manifest non-perturbative QCD effects. The Wigner distribution, at this scale, reflects the relationship between the position and momentum of partons. Integrating the Wigner function over the transverse distance yields the TMD, while integrating over transverse momentum yields a GPD with spatial information. Figure 2.11 shows the relationships of different types of parton distribution function [107]. Yoshitaka Hatta uses the dipole framework to show that the azimuthal angular correlations of coherent dijets are generated by the underlying Wigner distribution of the small-x gluons [108]. Furthermore, these correlations are consistent with predictions based on standard collinear factorization [12]. The diagram depicts a photon interacting with a nucleon. k_1 and k_2 are the transverse momenta of the final state jets. These jets originate from a quark-antiquark pair [4]. It is precisely this angular correlation what will be studied, as discussed in Chapter 5.

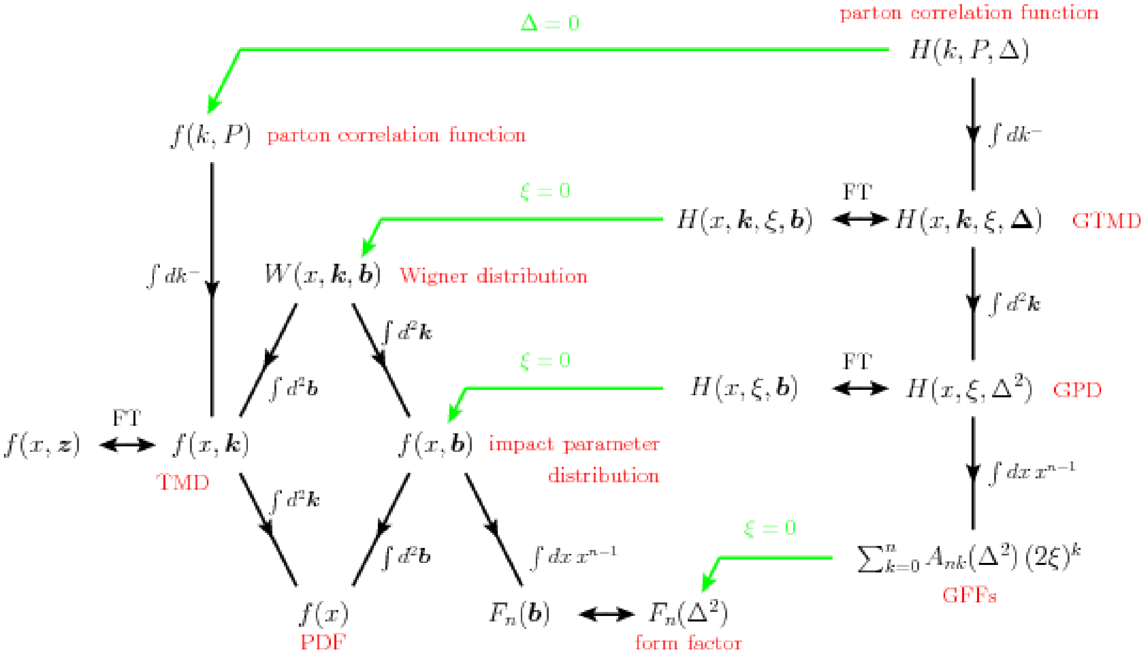

Figure 2.11: Interconnectedness of parton distribution functions [107].

Chapter 3

The CMS experiment at CERN LHC

The analysis presented in this thesis has been carried out using data from the CMS experiment. In this chapter we will first give an overview of the CERN Large Hadron Collider, and then describe the CMS detector in general and justify the reason why the CMS detector is a suitable machine to study this physics process.

3.1 Large Hadron Collider

The Large Hadron Collider (LHC) is a circular collider [109]. LHC has a radius of approximately 27 kilometers; as of this writing, it is the largest machine ever constructed. The initial purpose of the LHC was to discover the Higgs boson, and it is capable of investigating a wide variety of other physics phenomena such as dark matter, extra-dimensions, and heavy-ion physics.

The beams are accelerated along a circular path using radio frequency cavities, gaining energy with each revolution. LHC is a hadron collider, meaning it is designed to collide particles made of quarks and gluons. The proton-proton, proton-Pb, and Pb-Pb collision energies are the largest ever probed experimentally. What follows are brief descriptions of the various experiments utilizing the LHC. These experiments are enumerated to provide context for this analysis.

3.1.1 ATLAS

"ATLAS" stands for "A Toroidal LHC Apparatus". ATLAS was designed as a general purpose detector for LHC physics. Three toroidal superconducting magnets provide the field for particle identification. The looser design constraints of the ATLAS magnets allow for a more efficient, stand-alone measurement of muon momentum [110].

3.1.2 ALICE

"ALICE" stands for "A Large Ion Collider Experiment". ALICE was designed to study the quark-gluon plasma in ultra-relativistic heavy-ion collisions. The primary design consideration was the correct identification of particle species at high multiplicities. ALICE retains excellent particle identification at approximately $dN/d\eta = 4000$ in PbPb collisions, and this over a particle momentum range up to 100 GeV. PID is accomplished through a combination of time-of-flight chambers, muon detectors, and the analysis of specific ionization energy [111].

3.1.3 LHCb

"LHCb" stands for "Large Hadron Collider beauty", reflecting the LHCb's purpose: b-quark ("beauty") studies. By examining CP violation in heavy-quark hadrons, LHCb hopes to elucidate the asymmetry of matter and antimatter. LHCb is asymmetric in the z-axis: b-hadron pairs tend to scatter in the same forward rapidity, so the experiment only covers $1.9 < \eta < 4.9$. A large dipole magnet projects a field in the vertical plane of the LHC. Small asymmetries in the transverse scattering of the b-hadron system are used to test for CP violation [112].

3.1.4 TOTEM

"TOTEM" is a sub-experiment located at CMS. TOTEM uses Roman pots (RPS), placed far forward of CMS, to measure the total proton-proton interaction cross-section. The RPS have high acceptance for the flux very close to the beam. There are two sets of RPS, one on each side of CMS, located approximately 400 meters down the z-axis from the interaction point. The differential cross section of proton-proton scattering grows exponentially with $|t|$ at low values of $|t|$. More precise measurements of this differential cross section can help distinguish between competing models of proton structure. Furthermore, the total interaction cross section is an important benchmark for analyzing cosmic ray showers, and can be used to independently calibrate the beam luminosity measured at other LHC experiments. Diffractive studies at TOTEM complement those at CMS.

3.1.5 CASTOR

CASTOR – Centauro And Strange Object Research – is a calorimeter at CMS covering 5.1 – 6.55 in pseudorapidity. The calorimeters are both electromagnetic and hadronic, and located on either side of CMS, beyond the hadronic forward calorimeters. CASTOR was designed to detect centauro events which are thought to be caused by exotic matter produced in heavy-ion collisions. Typical centauro events are low multiplicity and high transverse momentum of the order of 100 GeV/*c*, with suppressed electromagnetic activity. There is also the possibility of a very high energy, highly penetrating particle in the forward region : the so called "long flying component". Centauro events have already been observed in cosmic-ray experiments, and there are phenomenological models for their production in QGP, and while these events have not been observed at the LHC, CASTOR provided interesting measurements related to very forward inclusive dijets sensitive to saturation physics [113].

3.2 Compact Muon Solenoid

The Compact Muon Solenoid (CMS) is a general-purpose particle detector located at Point-5 of the LHC ring. CMS was designed to precisely measure the momentum of muons. The titular superconducting solenoid magnet was designed to generate a 4 Tesla field and has been operating at 3.8 T to increase its longevity. This field is homogeneous and parallel to the beam line close to the interaction point. The momenta of muons are measured from how they deflect when moving through the magnetic field [114]. Altogether, CMS weighs approximately 12,500 metric tons, with a diameter of 14.6 m and a length of 21.6 meters [115].

The solenoid volume contains a silicon pixel and strip tracker, a lead tungsten crystal elec-

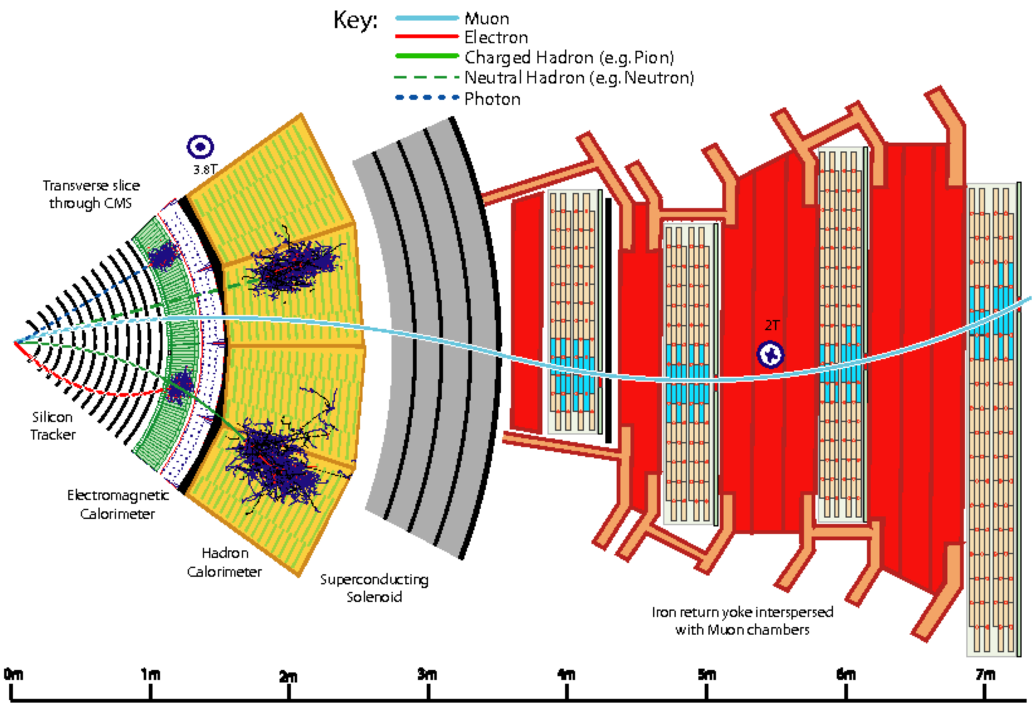

Figure 3.1: Slice of CMS; radial cross section view [116].

tromagnetic calorimeter (ECAL), and a brass and scintillator hadron calorimeter (HCAL), each composed of a barrel and two endcap sections. Fig. 3.1 shows the radial layering of CMS component systems [116].

3.2.1 Tracker

The tracker measures the momentum of charged particles via their trajectory through a homogeneous magnetic field. The tracker consists of two units, the pixel tracker and the strip tracker, both of which are made of silicon. Compared to large-volume gas detectors, which are less expensive, silicon detectors have a faster response time. The number of tracker layers is optimized for the highest penetration by charged particles while minimizing the occurrence of multiple scattering [117].

Multiple scattering reduces the efficiency and resolution of the tracker because of bremsstrahlung and other types of radiation. When a charged particle passes through an electric field, the changes

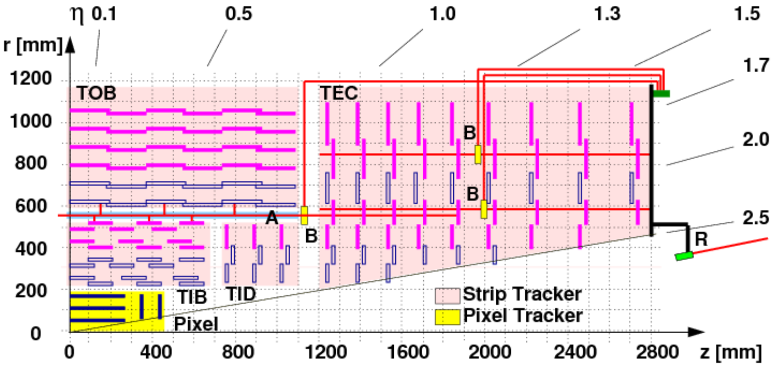

Figure 3.2: Pseudorapidity acceptance of tracker [118].

in acceleration will change the energy of the particle. The particle will release photons that will contaminate the signals read by the tracker.

The high luminosities reached by the LHC in the proton-proton run mode typically achieve some 20 to 30 collisions per bunch crossing, and increasing the number of hits in the tracker improves the pattern recognition of the particle flow algorithm (see section 3.2.6).

A charged particle causes an electrical signal when passing through a silicon pixel or silicon microstrip. CMS reconstructs these electrical signals, taken at specific points of position and time, into tracks. The spatial resolution on the tracks is approximately 10 micrometers. The tracker is meant to have a particle pass all the way through it, with only minimal effect on the particle's trajectory.

The tracker system is designed for high granularity and fast readout, such that each trajectory can be associated with its corresponding bunch crossing. The tracker is resilient enough to withstand the high flux of particles accompanying every bunch crossing; at the design luminosity of 10^{34} per $cm^2 s^1$, some 1000 particles will traverse the tracker every 25 ns. However, the mass of the tracker is minimal enough to suppress multiple scattering off its material that would distort particle trajectories. These design constraints – resistance and transparency – are satisfied by silicon. The tracker has approximately 200 m^2 of silicon surface, making it the largest silicon detector ever constructed. The pseudorapidity coverage of the pixel and strip trackers is shown in figure 3.2 [118].

In addition to excellent track reconstruction capabilities, the tracker provides high precision vertex reconstruction. Vertex reconstruction is a key ingredient in several high-profile LHC studies – Higgs, SUSY, extra-dimensions – because of the use of vertices in distinguishing non-prompt decays of heavy-quarks. The tracker is also instrumental in detecting the leptonic decays of W and Z bosons.

3.2.1.1 Pixel tracker

The first layer of the tracker is made of silicon pixel modules. This layer has a time resolution on the scale of 25 ns, meaning that it can take data for individual bunch crossings. Pixel technology is used because the high flux of particles, present at high beam luminosities, require high spatial resolution for proper pattern recognition. A major design constraint is that the pixel tracker had to be able to separate distinct tracks in high multiplicity environments. Tracks reconstructed by the pixels can be used to cross-check the results from the other parts of the tracker.

Every silicon pixel has a corresponding readout chip. The readout chips are soldered through the bump-bonding method. The readout chip amplifies signals from the pixel. The pixel tracker is precise enough to distinguish the vertices of tracks originating from short-lived particles, such as bottomonia. The innermost elements of the pixel tracker come within 4.4 cm of the CMS interaction point. The pixel tracker covers a pseudorapidity range of $|\eta| < 2.5$ with some 66×10^6 separate pixels.

3.2.1.2 Strip tracker

Outside the pixel tracker are the layers of the strip tracker. They function similarly to the components of the pixel tracker, except the strip tracker consists of thin silicon plates. The strip tracker itself can be broken down into four components: the inner barrel layer, the inner endcaps, the outer barrel layer, and the outer endcaps. In total, these layers cover a pseudorapidity range of $|\eta| < 2.5$ and contain some 9.3×10^6 strips.

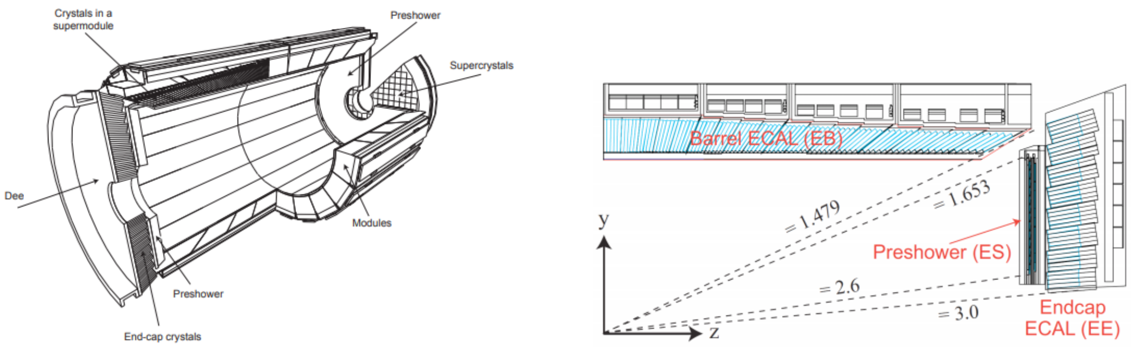

Figure 3.3: ECAL components [119].

3.2.2 Electromagnetic calorimeter

The Electromagnetic Calorimeter (ECAL) is the dedicated CMS calorimeter for detecting electrons and photons. The calorimeter is comprised of lead tungstate ($PbWO_4$) crystals arranged in a cylinder about the beam, including two endcaps, as seen in Figure 3.3 [119]. The granularity of these crystals gives the ECAL excellent energy resolution, angular resolution, and spatial resolution; for example, the ECAL has the resolution suitable for the decay of the Higgs boson into two photons. The ECAL is both hermetic and homogeneous [120].

The data readout is fast enough that CMS can trigger off signals in the ECAL. It takes about 25 ns for an ECAL hit to scintillate 80 percent of its light, putting the calorimeter's rate on the same scale as the bunch crossing. Scintillation in the crystals activates photodetectors that transmit information to the L1 trigger. In the barrel these photodetectors are avalanche photodiodes (APDs). The endcaps use vacuum phototriodes (VPTs). ECAL's energy resolution, as a function of energy, is given by figure 3.4 [121]. The resolution increases with energy because, at large energies, parton showers become more similar as their random fluctuations average-out.

In CMS trigger development, "EG" triggers fire based on energy deposits in the ECAL; Figure 3.5 gives the EG trigger energy resolution [121]. This energy comes primarily from electrons and photons. When these particles strike a tungstate crystal, the particle shower size is approximately that of the crystal. Electrons are distinguished from photons by the correlation of a track to ECAL energy. The L1 trigger does not fire on tracks, which are reconstructed at the HLT level. Thus, L1

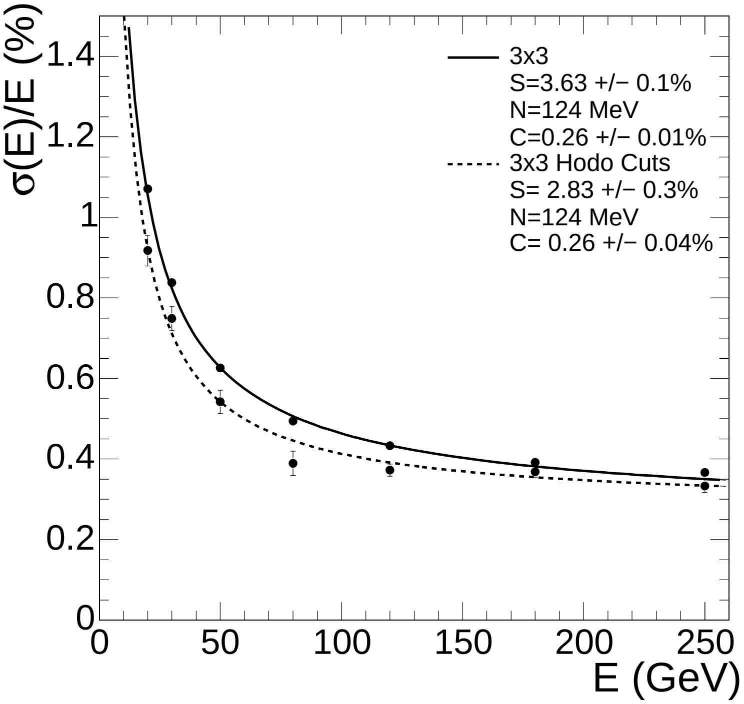

Figure 3.4: Reconstructed data, ECAL energy resolution; the upper data points correspond to events taken by a 20x20 mm^2, and the lower data points correspond to events taken by a 4x4 mm^2 trigger [121].

EG triggers do not distinguish between electrons and photons.

3.2.3 Hadronic calorimeter

The Hadronic Calorimeter (HCAL) is the next layer outside the ECAL. The HCAL absorbs particles and measures their energy and momentum via scintillation. HCAL has such a large acceptance that it can indirectly observe non-interacting particles such as neutrinos. The HCAL is designed to be hermetic, so that imbalances of momentum and energy can be precisely measured [122]. Figure 3.6 plots the HCAL's energy resolution; note that the resolution changes with $|\eta|$ [121].

There are four sub-sections of the HCAL: the inner barrel (HB) and the outer barrel (HO), two endcaps (HE), and two forward calorimeters (HF). The HF are the most relevant to this analysis because of their use in triggering on non-hadronic events. Figure 3.7 shows the HCAL components and their locations [121].

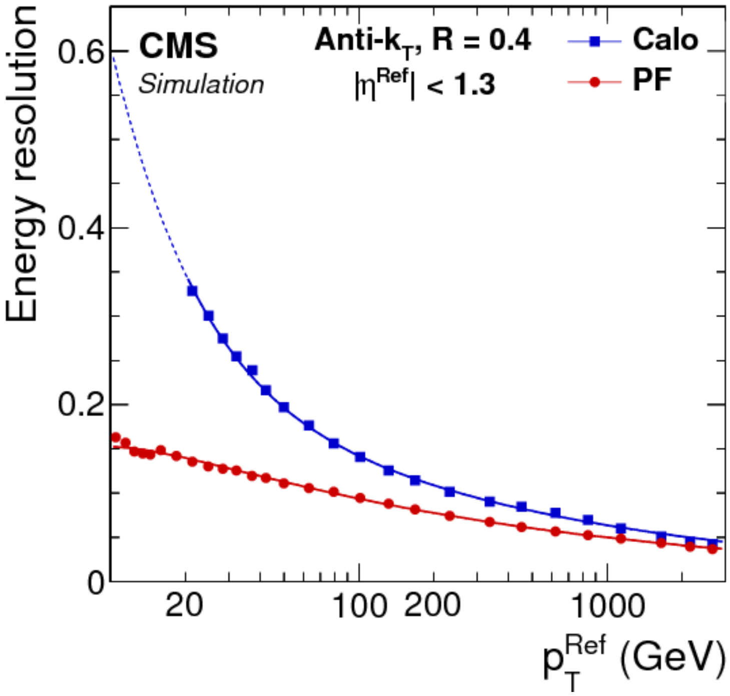

Figure 3.5: ECAL energy resolution, showing the results for calorimetry (calo) and particle flow (PF) approaches [121].

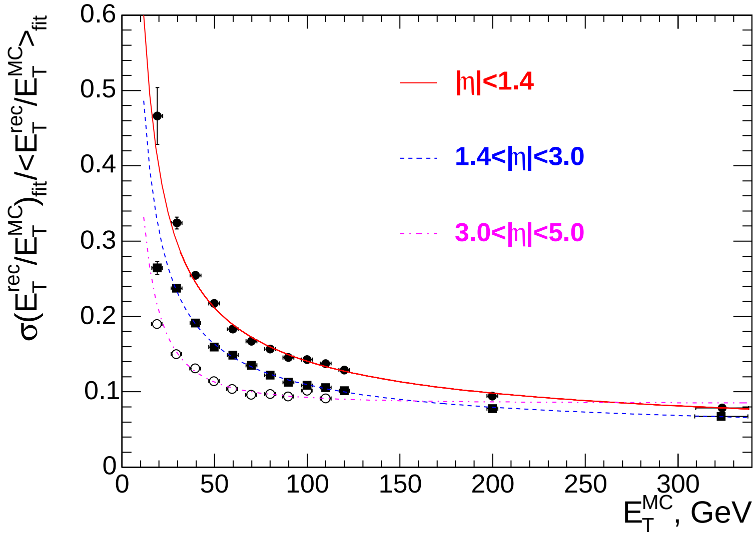

Figure 3.6: HCAL energy resolution as a function of simulated jet energy, binned by pseudorapidity. The jet reconstruction algorithm uses an iterative of cone $R = 0.5$. [121].

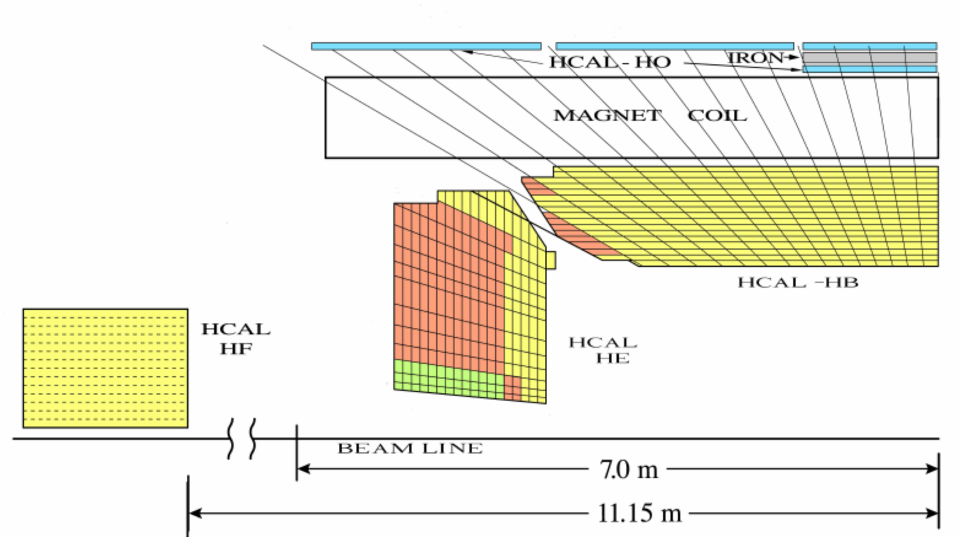

Figure 3.7: HCAL components; HB, HE, and HF [121].

3.2.3.1 Hadronic forward calorimeters

The Hadronic Forward Calorimeters (HF) absorb the greatest portion of energy from collisions. The HF are directly down beam from the interaction point, and when the hadrons dissociate, most of the resulting particles will strike the HF. As named, they are located in the forward region ($3.0 < |\eta| < 5.2$) of CMS and complement the coverage provided by the barrel and endcap detectors.

HCAL is made of quartz fibers and steel absorbers for maximum radiative resistance. When high energy particles pass through the quartz fibers, these particles are moving faster than the speed of light in the medium, depositing energy that causes particle showers. These showers give off light, in the form of Cherenkov radiation, that the fibers transmit to photomultiplier tubes (PMTs). The PMT signals are converted into a digital signal by a charge integration encoder (QIE) chip. Then HCAL trigger and readout boards (HTR) use these digital signals to calculate luminosity. The HTR information is part of the data used for L1-triggering. Triggering on HF can also be done by vetoing on HF activity.

Hits in the HF are used to measure the instantaneous luminosity of CMS. As shown in Figure 3.6, the HF have a finer E_T resolution than the other parts of the HCAL. Furthermore, because HF electronic noise is comparatively small with respect to HF threshold for a minimum bias event,

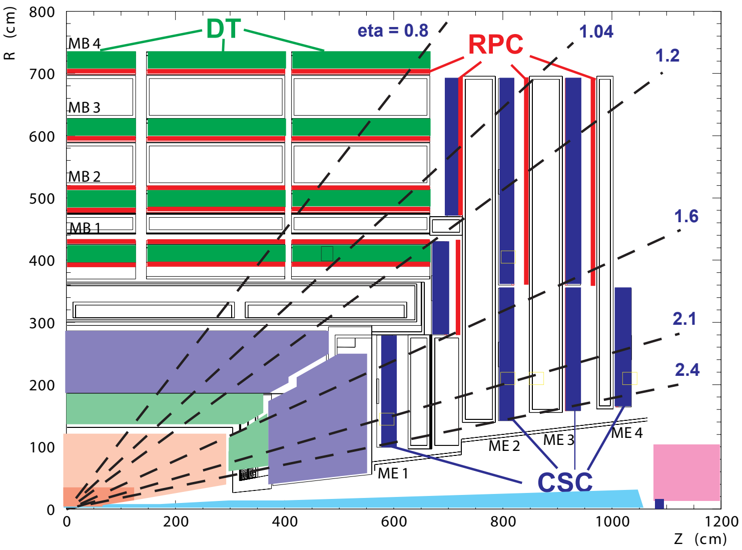

Figure 3.8: Pseudorapidity acceptance of muon detector [121].

applying a veto on the HF threshold is a reliable measure for UPC processes characterized by low event activity.

3.2.4 Muon detector

The outermost layer of CMS consists of the muon detectors, as seen in Figure 3.8 [121]. Muons are particles nearly identical to electrons, except for their mass, which exceeds that of the electron by some two orders of magnitude. High mass particles, like the W and Z boson, often decay into a final state containing muons. The muon detector not only identifies muons, but also measures their momentum. The muon detector has a readout fast enough for triggering on muons [123] [124].

The muon detector consists of three types of component: muon drift tubes (DT), cathode strip chambers (CSC), and resistive plate chambers (RPC). The DTs are gas filled chambers that contain a stretched metal wire. When muons pass through the DT gas, electrons are excited. These electrons escape from the gas atoms and are attracted to the metal wire, which triggers a signal. The CSC, located in the endcaps, operate under similar principles, but contain perpendicular arrays of positively charged and negatively charged wires immersed in gas. The RPC do not use electrode wires to detect excited electrons; instead, high-resistivity plates are used as alternating cathodes and anodes [125].

3.2.5 Zero degree calorimeter

The zero degree calorimeters are located at both sides of CMS, approximately 140 meters from the interaction point. Each ZDC consists of two independent systems: an electromagnetic calorimeter, for detecting very forward photons, and a hadronic calorimeter, for detecting neutrons. Because these neutrons result from the dissociation of nuclei, the ZDC can measure the centrality of heavy-ion collisions. Hadrons in the forward region have energy on the TeV scale, so the ZDC's hadronic calorimeter is made of thick tungsten plates [126]. For a UPC process, the photon emitting nucleus is most likely to remain intact; therefore, ZDC data can determine the photon direction of a process, and by extension its energy. Tagging forward neutrons can also be used as an online luminometer [127].

Chapter 4

Trigger development and performance

4.1 Triggering at CMS

At stable beams, the LHC delivers bunch crossings every 25 nanoseconds. Each bunch crossing in turn will have some 20 hadron collisions. The resulting interaction rate – 10^9 interactions per second – is orders of magnitude greater than the frequency that events can be written to disk, 10^2 events per second. CMS therefore needs a means of filtering out the most interesting 10^2 interactions per second while declining the other 10^9 interactions per second.

CMS uses a two-tiered triggering system. The first tier, the L1 trigger, is hardware based. The second tier, the high-level trigger (HLT), is software based. The L1 trigger receives raw data from the calorimeters and the muon detectors; this determines when the tracker will read out data. The raw data from the tracker, calorimeters, and muon detectors is then passed on to a computer farm running the HLT menu. The HLT then performs a simplistic reconstruction of the raw data into physics objects useful for analysis: jets, tracks, and identifiable particles. If an event passes the HLT, the raw data is permanently stored in preparation for a more complex reconstruction [128] [129].

Figure 4.1 is an outline of the flow of information between the subcomponents of the L1 trigger. The first division is between the calorimeters and the muon detectors. Calorimeter energy deposits are registered by the regional calorimetry trigger. Zero counting information is then sent to the global calorimetry trigger. The muon detector send signals to pattern recognition circuits that associate the detector hits into low resolution tracks; the hits and tracks are then sent to the global muon trigger. The global calorimetry trigger and the global muon trigger then combine at the global trigger, which uses information from the TTC (Timing, Triggering, and Control) system to synchronize signals back to the tracker, ECAL, HCAL, and muon detectors [130].

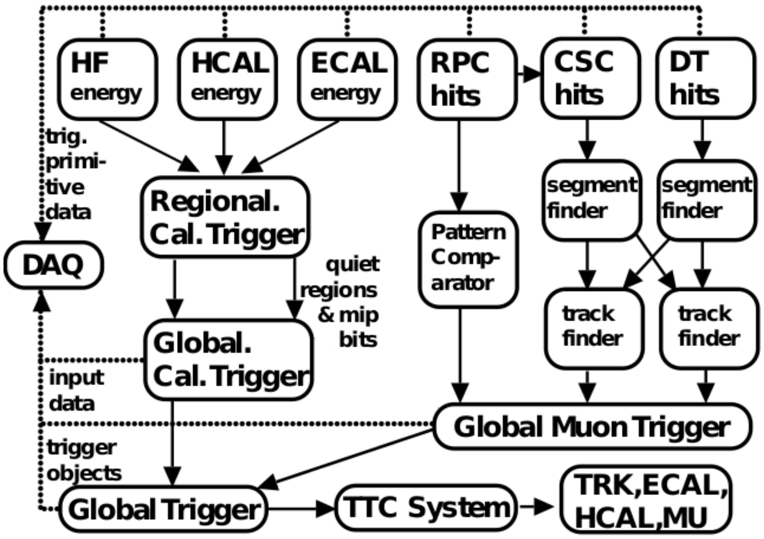

Figure 4.1: Flow of information in L1 trigger [130].

The L1 trigger can only pass some 1 in 1000 interactions to the HLT. The L1 trigger menu has an output rate of approximately 100 kHz. L1 achieves this rate by only considering data of reduced granularity and reduced resolution. A buffer is used to store the full event data while the L1 trigger runs. The HLT menu reduces this to about 100 Hz as required by the limit on disk writing.

The 2015 UPC triggers were for low multiplicity events and low transverse momentum events. Typical heavy-ion collisions are high multiplicity events. Hard scattering dominates. Figure 4.2 is an event display of one of the first heavy-ion collisions at CMS in 2010.

Figure 4.3 is the event display of a UPC upsilon candidate. Notice that there are only two reconstructed tracks, and that CMS is an otherwise empty detector. These events constitute a complement to those passing more conventional heavy-ion triggers.

For this analysis that focuses on coherent dijet photoproduction, the L1 trigger applies two selections. First, it checks that at least one of the HF calorimeters is empty. This is the most important part of the trigger as it suppressed the hadronic contamination of the data set. Then, if there are at least 5 GeV of energy deposited in the ECAL, the event passes to the HLT.

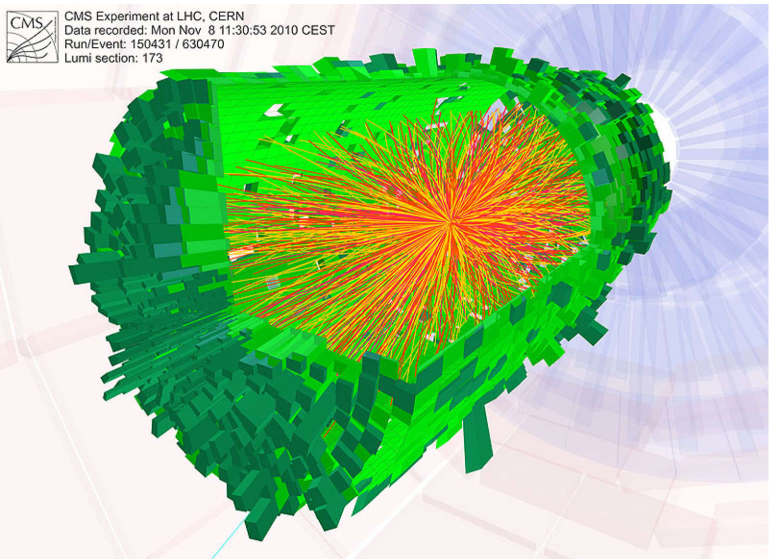

Figure 4.2: High multiplicity PbPb collision.

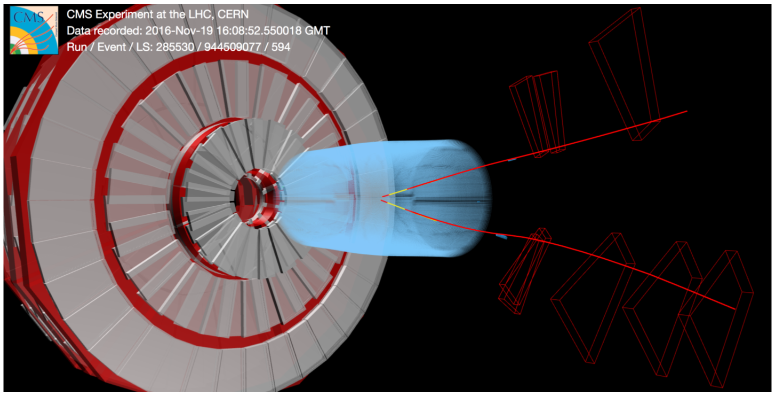

Figure 4.3: UPC Upsilon candidate.

Low multiplicity events are difficult to distinguish from background. To compensate, the HLT in turn requires that there be at least once reconstructed track from the pixel tracker to ensure that there are particles that will be reconstructed by the complete tracker. Only the pixel tracker is used for these HLTs to increase the speed of reconstruction while decreasing needed computer cycles.

4.1.1 Particle flow algorithm

Data from the sub-detectors is combined, for event reconstruction, by the particle-flow (PF) algorithm [131, 132]. The PF takes the data about tracks in the tracker and energy deposits in the calorimeter, and uses them to reconstruct physics-related objects like jets and to identify specific particles, such as photons and muons. The PF algorithm also identifies missing energy and momentum for use in neutrino studies.

Unlike physics-objects in the data of previous experiments, PF physics-objects can fire HLTs. After an event passes the L1 trigger, a partial event reconstruction is performed. Energy deposits in the HCAL that can be associated with a track signify charged hadron candidates; if the track-associated energy deposit is in the ECAL, the corresponding object is an electron candidate. Tracks not associated with a calorimeter deposit are considered muon candidates. Left over energy deposits are used to create neutral hadron candidates, if in the HCAL, or photon candidates, if in the ECAL. Each of these candidates is assigned a four-vector based on the sub-detector information [131].

The collection of basic PF candidates are used to create more complex physics objects. The total transverse momentum of the event is used to locate "missing transverse momentum" (MET). MET candidates have a four-vector, and can be used to construct physics-objects such as neutrinos. The curvature of tracks is used to measure the momentum of the charged hadrons, and thus their particle species. The speed and efficiency of the calculation and combination of PF objects enables CMS to trigger for a wide variety of physics by modifying software.

The PF algorithm is also responsible for implementing the jet reconstruction algorithms of CMS. In the analysis presented in this thesis the anti-kt jet reconstruction algorithm is used. Anti-kt algorithms are sequential algorithms that take into account two quantities: the distance between two given particles i and j, d_{ij}, and the distance between a given particle i and the beam, d_{iB}. For a specific particle i, all the d_{ij} and d_{iB} are calculated. If the smallest quantity in the collection is di_{ij}, the particles i and j are combined as four-vectors. The summed four-vector replaces particle i, and all of the distances are recalculated. If d_{iB} is the smallest quantity, then i is designated a "jet" and removed from the collection. This process iterates until all particles are removed from the collection, replaced by "jets" associated with one or more particles [133]. This analysis uses jets reconstructed with the anti-k_t algorithm with distance parameter $R = 0.4$.

CMS gains significant jet reconstruction efficiency via the PF. At low transverse momentum,

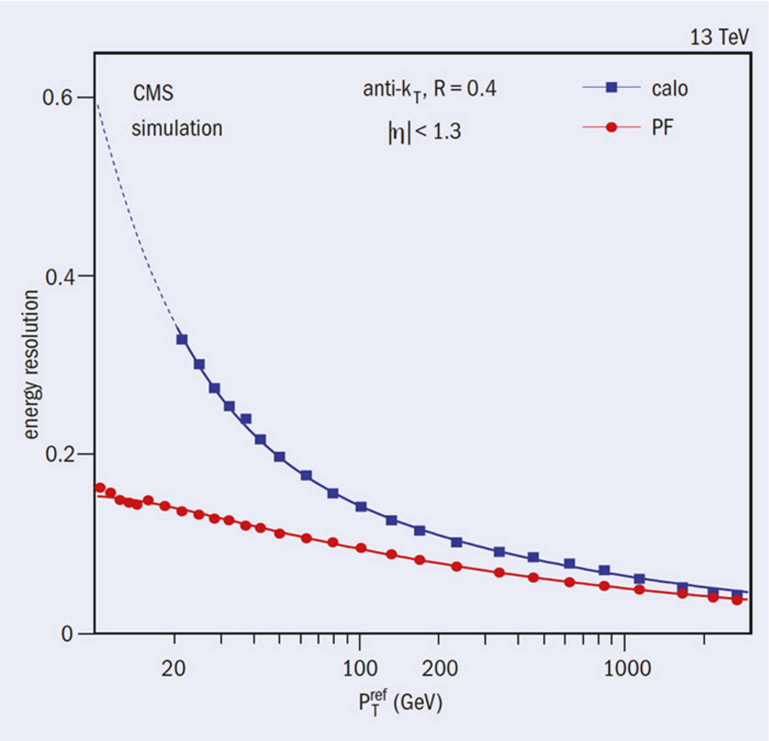

Figure 4.4: Performance of particle flow algorithm compared to simulated calorimeter readout [132].

PF reconstructs jets at nearly twice the resolution of HCAL and ECAL. This increase in efficiency comes from the PF integrating in track data with the calorimeter tower data. Figure 4.4 compares the performance of the PF algorithm to the calorimeter reconstruction [132].

CMS was the first modern collider experiment to replace traditional triggering, based on energy-deposits and tracks, with HLTs leveraging PF-reconstructed particles. This achievement was enabled by the high precision, high accuracy technologies described in this chapter. Experimentalists, now more than ever, prepare their analyses with unprecedentedly accurate analogues to processes calculated by theorists. For a given process, a theorist can determine the properties of the final state particles, and encode these in an MC generator. Experimentalists can then run the MC through a simulation of CMS and compare what the PF reconstructs to the MC-truth. This technique is particularly useful for emulating the performance of trigger menus [131].

4.2 Author's contributions

In preparation for the 2015 heavy-ion run and the 2016 p-Pb run, we prepared high-level trigger menus for the CMS Forward Heavy-Ion group. This trigger menu was optimized for firing on ultra-peripheral collisions. We tested the menu's performance on Monte Carlo generated by STARLIGHT [79] and reconstructed through a GEANT4 [134] simulation of CMS. During the experiment, I was present at CERN to monitor the trigger rates and deliver daily reports on their performance.

The CMS software (CMSSW) includes an emulator for the L1 trigger. This software can re-emulate alternative L1 menus on previously taken CMS data. The performance of a trigger on the 2011 PbPb data, taken at $\sqrt{s_{NN}} = 2.7$ TeV is extrapolated to the higher energy, $\sqrt{s_{NN}} = 5.2$ TeV of the 2015 PbPb run.

The HLT menu was tested on both STARLIGHT MC and on data from the 2011 Pb+Pb run. STARLIGHT is a MC generator for ultra-peripheral collisions, in particular for the vector-meson photoproduction channels. I used STARLIGHT to generate MC sets for $Pb+Pb \rightarrow J/\Psi + Pb + Pb$ and $Pb+Pb \rightarrow \Upsilon(1s) + Pb + Pb$. I then used CMSSW to test the performance of the component bits of the HLT paths with respect to these MC sets.

It was my responsibility to carefully observe the state of the UPC triggers during the heavy-ion run. If the total HLT rate ever drifted above 100 Hz, the HLT menu could crash and CMS lose considerable data. It was important for the trigger contacts to make sure that their HLT paths were behaving in a stable manner. I also analyzed express physics data to test that the vector-meson triggers saw appropriate mass resonances. Table 4.1 shows the L1 rates for a high integrated luminosity run during the 2015 PbPb period. Table 4.2 shows the HLT rates for the same run.

For the 2016 pPb run I prepared a trigger menu similar to that of the 2015 PbPb run. Table 4.3 shows the L1 rates for a high integrated luminosity run during the 2016 pPb period. Table 4.4 shows the HLT rates for the same run.

The UPC HLTs we designed are useful to study a wide variety of physics processes. In addition to the coherent dijet study that is the subject of this thesis, the data gathered through the 2015

Table 4.1: L1 Trigger Average Rates for Run 263757

L1 Type	Pre-DT Rate (Hz)	Pre-DT RMS Rate (Hz)	Post-DT Rate (Hz)	Post-DT RMS Rate (Hz)	Initial Prescale	Final Prescale
Double muon + HF veto (thresh. 1)	7.78	8.39	7.64	8.24	0	0
Double muon + HF veto (thresh. 2)	7.86	8.49	7.71	8.33	0	0
Single muon + HF veto (thresh. 2)	85.58	89.76	84.31	88.53	0	0
Double EG2 + HF veto (thresh. 2)	2.26	2.62	2.19	2.54	0	0
Single EG5 + HF veto (thresh. 2)	13.71	16.13	10.8	13.14	0	0

Table 4.2: HLT Average Rates for Run 263757

HLT Type	L1 Seed	Average Rate of HLT (Hz)
L1 pass through	Double muon + HF veto (thresh. 1)	7.64
Requires pixel track	Double muon + HF veto (thresh. 1)	1.09
L1 pass through	Double muon + HF veto (thresh. 2)	7.71
Requires pixel track	Double muon + HF veto (thresh. 2)	1.11
L1 pass through	Single muon + HF veto (thresh. 2)	22.41
Requires pixel track	Single muon + HF veto (thresh. 2)	11.18
L1 pass through	Double EG2 + HF veto (thresh. 2)	2.19
Requires pixel track	Single EG5 + HF veto (thresh. 2)	3.96

Table 4.3: L1 Trigger Average Rates for Run 285530

L1 Type	Pre-DT Rate Before Prescale (Hz)	Pre-DT Rate After Prescale (Hz)	Post-DT Rate (Hz)
Double muon + HF veto (1 Tower)	5.47	5.47	5.38
Double muon + HF veto (2 Tower)	5.47	5.47	5.38
Single muon + HF veto (1 Tower)	123.31	123.31	121.15
Single muon + HF veto (2 Tower)	123.31	123.31	121.15
Double EG2 + HF veto (1 Tower)	228.22	N/A	N/A
Double EG2 + HF veto (2 Tower)	228.22	N/A	N/A
Single EG5 + HF veto (1 Tower)	211.17	211.17	207.00
Single EG5 + HF veto (2 Tower)	211.17	211.17	207.00

Table 4.4: HLT Average Rates for Run 285530

HLT Type	L1 Seed	Average Rate of HLT (Hz)
L1 pass through	Double muon + HF veto (1 Tower)	5.40
Requires pixel track	Double muon + HF veto (1 Tower)	1.20
L1 pass through	Double muon + HF veto (2 Tower)	5.40
Requires pixel track	Double muon + HF veto (2 Tower)	1.20
L1 pass through	Single muon + HF veto (1 Tower)	121.70
Requires pixel track	Single muon + HF veto (1 Tower)	58.16
L1 pass through	Single muon + HF veto (2 Tower)	121.70
Requires pixel track	Single muon + HF veto (2 Tower)	58.16
L1 pass through	Double EG2 + HF veto (1 Tower)	N/A
Requires pixel track	Double EG2 + HF veto (1 Tower)	N/A
L1 pass through	Double EG2 + HF veto (2 Tower)	N/A
Requires pixel track	Double EG2 + HF veto (2 Tower)	N/A
L1 pass through	Single EG5 + HF veto (1 Tower)	208.18
Requires pixel track	Single EG5 + HF veto (1 Tower)	159.79
L1 pass through	Single EG5 + HF veto (2 Tower)	208.18
Requires pixel track	Single EG5 + HF veto (2 Tower)	159.79

trigger menu can address UPC photoproduction of coherent and incoherent J/ψ, coherent $\psi(2s)$, coherent ρ^0, possible ρ^0 excited states, and light-by-light scattering. The 2016 trigger menu is uniquely suited for studying exclusive vector meson photoproduction off the proton in pPb UPC and it is also possible to study UPC jets. All of these studies have the potential for expanding our knowledge of the nuclear gluon PDFs at small-x, from 10^{-2} to 10^{-5}.

Chapter 5

Monte Carlo and CMS data analysis

The analysis presented in this thesis focuses on the study of angular correlations of dijet events in ultra-peripheral PbPb collisions at $\sqrt{s_{NN}} = 5.02$ TeV. The dijets are produced by the interaction of a photon with the lead nuclear target, where the photon is emitted from one of the two colliding particles. Since this is an exclusive reaction (having only two jets in the event) we have used a trigger from ultra-peripheral collisions and apply a series of analysis selections offline to select the events. In this Chapter, first we present the Monte Carlo generator used for this analysis. Second, we present the analysis selections and discuss the relevant information and physics conclusions obtained. In the next chapters, the assessment of the systematic uncertainties and the presentation and discussion of the results will be given.

5.1 Monte Carlo sample

In this analysis we compare RAPGAP [135] to data. RAPGAP generates Monte Carlo (MC) of exclusive dijets based on next-to-leading-order (NLO) QCD matrix elements. RAPGAP was originally designed to model photoproduction in electron-proton collisions, where the electron is a source of virtual photons. For this analysis, RAPGAP was configured to model boson-gluon fusion (BGF) in its electron-proton collision mode. RAPGAP generates events using the F2 structure function to describe the interaction between the low-virtuality photon and the quark. As discussed in Section 2.3, RAPGAP has been found to correctly describe the diffractive dijet distributions at HERA energies.

RAPGAP uses diffractive PDFs obtained by the H12006 fit-A model. Diffractive PDFs are obtained by requiring the proton to remain intact and use fits to electron-proton data by the H1 collaboration. The MC study indicates that the cross section of diffractive dijets predominantly falls within Bjorken-x < 0.01 and $Q^2 < 0.05$ GeV^2. The F2 structure function is well described within this phase-space. Because of the low Q^2, F1 is negligible. The RAPGAP version 3.2.2 is used.

In order to compare RAPGAP [135] to data, its photon energy spectrum has to be modified since RAPGAP was not designed for nuclear targets. We have reweighted the RAPGAP events by the photon-energy distribution computed by STARLIGHT [136] to correct for this difference. Such a model is referred to as RAPGAP + STARLIGHT in this analysis.

STARLIGHT is a Monte Carlo generator that models two-photon and photon-hadron interactions at ultra-relativistic energies. It is based on the equivalent-photon approximation (EPA) [136]. For a given impact parameter b and a photon energy k, the number density of the photons is

$$N(k,b) = \frac{Z^2\alpha}{\pi^2}\frac{k}{(\hbar c)^2}\frac{1}{\gamma^2}\left[K_1^2(x) + \frac{1}{\gamma^2}K_0^2(x)\right] \tag{5.1}$$

where K_1 and K_0 are modified Bessel functions.

The MC output of RAPGAP is then fitted to the STARLIGHT photon distribution by calculating the weight of an event by the following ratio

$$w(E) \equiv \frac{dN_\gamma^{STARLIGHT}}{dE} / \frac{dN_\gamma^{RAPGAP}}{dE}. \tag{5.2}$$

After the fit to the photon distribution, the RAPGAP+STARLIGHT MC is converted to hepMC format and run through a GEANT4 simulation of CMS to account for particle transport and detector response. The resulting AOD files are then skimmed into “hiforest ntuples".

RAPGAP requires PYTHIA [137] and LHAPDF [138] as additional packages. This analysis uses PYTHIA v6.413 and LHAPDF v5.31. The MC event-record is given in the form of PYJET, a common block from PYTHIA. This event record contains the photon energy fraction in the RAPGAP common block. Some additional details about the MC generation used in this analysis are given in Appendix A.

5.2 Data selection

As mentioned in Chapter 5, this analysis uses a data sample collected in PbPb collisions with the CMS detector in 2015, corresponding to an integrated luminosity of 0.38 nb^{-1}. The integrated luminosity is calibrated using data from van der Meer scans. The events are selected with the “HLT_HIUPCSingleEG5NotHF2Pixel_SingleTrack" trigger optimized to select dijets from ultra-peripheral PbPb collisions. This trigger has three elements: a transverse energy of at least 5 GeV must be deposited in one tower of the electromagnetic calorimeter (ECAL); at least one HF must have no signal above the noise threshold, and at least one track must be reconstructed in the pixel detector. This means that this trigger selects exclusive-type events where there is no activity in both HF detectors (the topic of this analysis), or inclusive photonuclear dijets where there is no activity on one side of the detector. Note that for all of the analysis presented in this thesis both HF calorimeters have been required to be empty using the selections discussed below.

Events from UPCs have much lower multiplicity than typical nuclear PbPb collisions. In order to maximize the track finding efficiency the events are reconstructed using the standard CMS track reconstruction and the particle-flow algorithm [132] used for proton-proton collisions.

The z position of the primary vertex is required to be within $\pm$ 20 cm of the beam spot center (see Figure 5.1). The length of the pixel clusters must be consistent with tracks originating from this vertex. This requirement removes beam-background events that produce elongated pixel clusters.

The leading jet p_t is required to be above 20 GeV, while the subleading jet p_t is required to be above 15 GeV. The dijets are required to have an invariant mass of at least 35 GeV to be consistent with the jet energy resolution. In addition, both the leading and subleading jets are required to have $-1.8 < \eta < 1.8$, where η is the pseudorapidity of each jet. Figure 5.2 shows the transverse momentum p_t distribution for the leading and subleading jets.

Figure 5.3 shows the HF leading tower energy distribution for both the HF+ and HF- calorimeters, after requiring at the analysis (offline) level that both HF detectors have their energy thresholds below the electronic noise. These thresholds have been obtained from analyzing events triggered

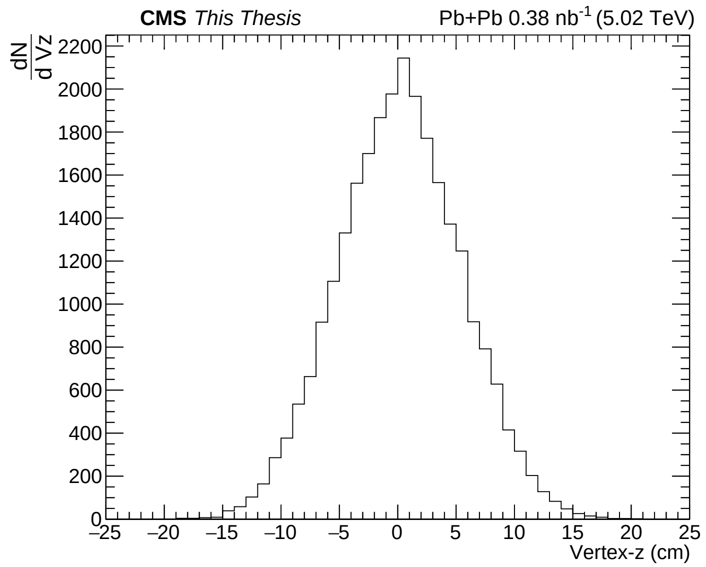

Figure 5.1: Measured vertex-z distribution for events that passed the trigger and dijet selection.

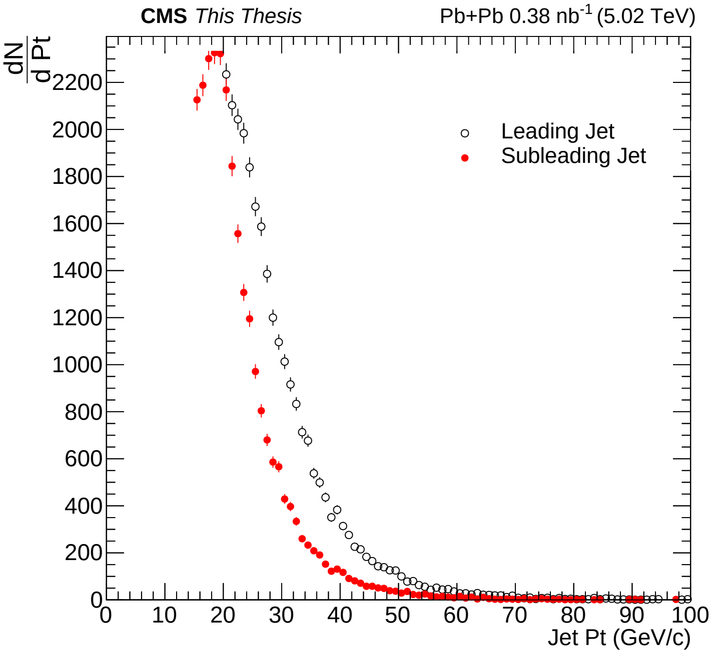

Figure 5.2: Transverse momentum distribution for the leading (open points) and subleading jet candidates (red full points).

when at least one of the beams did not collide at the interaction point. The energy threshold is 3.6 GeV for HF- and 3.94 for HF+. For completeness, Figure 5.4 shows the scatter plot between both HF leading tower distributions, indicating that most of the selected events have very low energy deposited in both detectors.

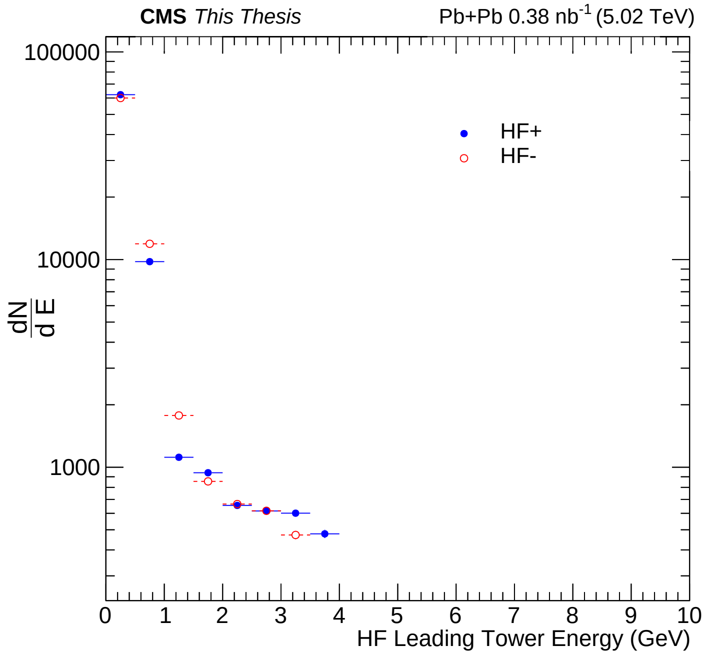

Figure 5.3: Leading tower energy for HF+ and HF- for events that passed the UPC trigger used in this analysis: “HLT HIUPCSingleEG5NotHF2Pixel SingleTrack", after requiring that both HF detectors have their energy thresholds below the electronic noise.

Figure 5.5 shows the jet multiplicity for the events that passed the analysis selection discussed above. It can be seen that most of the selected events have indeed only two jets. It is interesting to study the track multiplicity for the selected events. Figure 5.6 shows such a distribution for events that have exactly one dijet (red points) as well as the distribution without any jet multiplicity requirement (blue points). It can be observed that the average track multiplicity for the events is around 7 for the exactly one dijet sample, which is very similar to the other sample without any jet multiplicity requirement. It is important to emphasize, as mentioned before, that the jet reconstruction in this analysis uses the particle-flow algorithm discussed in Section 4.4 which uses the information from various detectors for jet reconstruction.

We have studied the difference in azimuth between the two jets in the laboratory frame since the ultra-peripheral dijet events typically have a back-to-back topology. Figure 5.7 shows the $\Delta\phi$ distribution for each pair of jets, for events that have exactly two jets (black points), exactly three

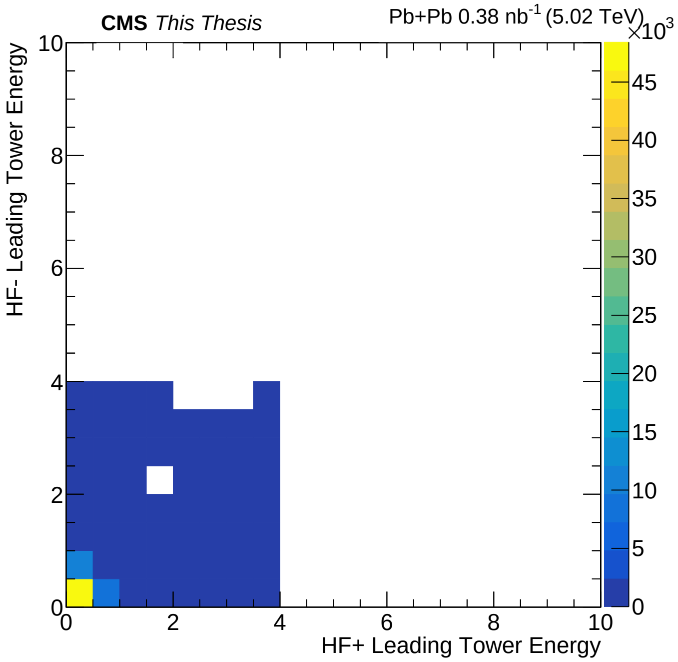

Figure 5.4: Scatter plot between the leading tower energy for HF+ and HF- for events that passed the UPC trigger used in this analysis: “HLT HIUPCSingleEG5NotHF2Pixel SingleTrack", after requiring that both HF detectors have their energy thresholds below the electronic noise.

jets (red points) and more than three jets (blue points). As shown in Figure 5.5 most of the events have exactly two jets, and figure 5.7 shows that as the jet multiplicity increases the $\Delta\phi$ distribution gets wider, as expected. In addition, we can notice that most of the selected events have a $\Delta\phi > 2$, which is consistent with back-to-back jets. For this reason, we have applied the selection that the dijets have precisely $\Delta\phi > 2$. Henceforth, only events that have exactly one dijet are considered because this is one of the characteristic features of UPC dijets we are studying.

Another way to confirm that the selected events are from UPC dijets is to study the momentum imbalance between the leading and subleading jets. This can be studied by measuring the A_j distribution defined as $A_j = \frac{p_{t,1}-p_{t,2}}{p_{t,1}+p_{t,2}}$ (see Figure 5.8), where $p_{t,1}$ corresponds to the transverse momentum of the leading jet, and $p_{t,2}$ is the transverse momentum of the subleading jet. It is interesting to mention here that in the case of inclusive dijet production in high-energy nucleus-nucleus collisions where “jet quenching" has been observed, the A_j distribution is much wider, showing average A_j values much larger than 0.4. The A_j values for the selected events shown

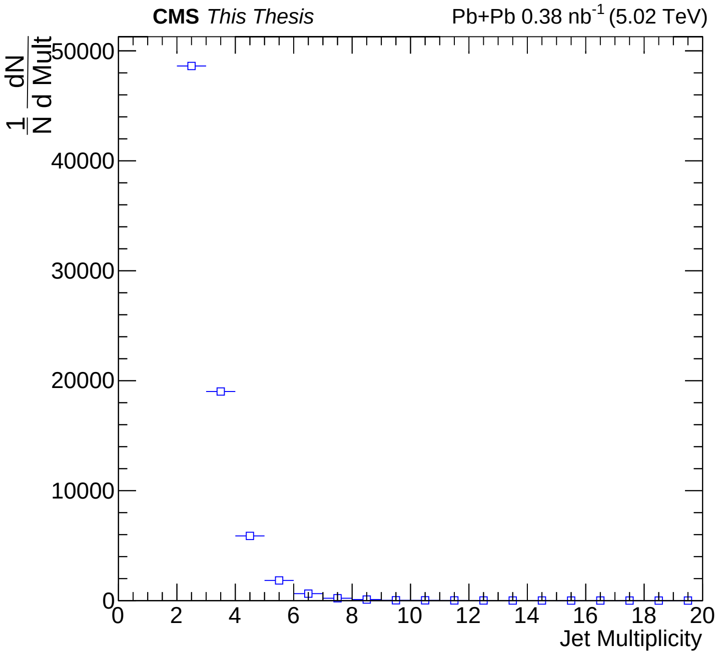

Figure 5.5: Jet multiplicity distribution for events that passed the UPC trigger and basic analysis selection (see text for details).

in Figure 5.8 are consistent with proton-proton collisions where there is no "jet quenching" or momentum imbalance. This again is consistent with UPC dijets. This result is also confirmed by studying the transverse momentum distribution for the UPC dijet events as shown in Figure 5.9. These figure also shows that apart from purely coherent dijets the data sample contains events from hard-scatting processes (DIS-type) that have a larger transverse momentum.

Figure 5.10 shows the invariant mass distribution for the UPC dijet candidates. The dijet system extends to invariant mass values beyond 100 GeV; the mean of the distribution is around 50 GeV. The rapidity distribution for the dijet system is shown in Figure 5.11.

5.2.1 Large rapidity gaps using the tracker

In order to clasify the events as forward-going and backward-going dijets, and so study the energy dependence of these proceses, we have applied a large rapidity gap using the tracker.

Photon-induced events are typically asymmetric in rapidity. Thus, these dijets are produced

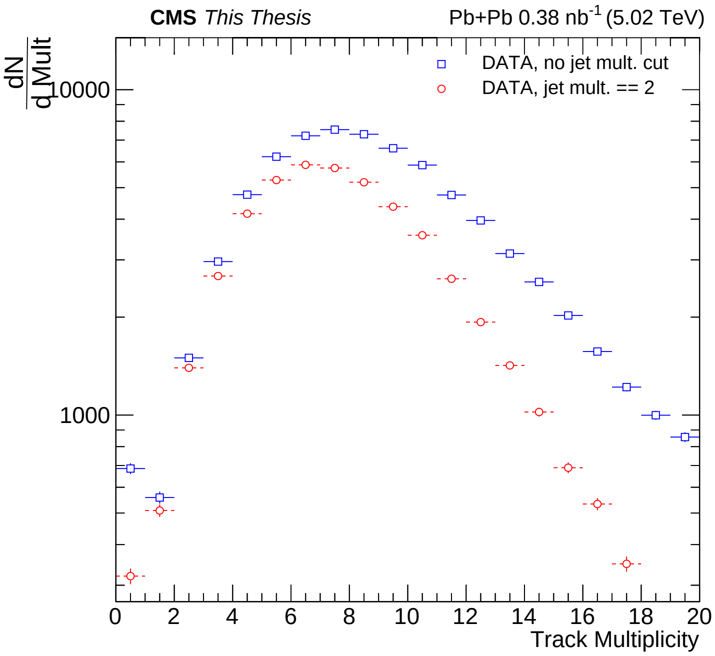

Figure 5.6: Track multiplicity distribution for events that passed the event selections discussed in the text. The distributions with exactly one dijet (points in red) and without any jet multiplicity requirement (points in blue) are shown.

in either the backward or forward hemispheres of CMS, and are characterized by a large forward rapidity gap (FRP), or a large backward rapidity gap (BRP), respectively.

Figure 5.12 is an example of a coherent-type dijet event display. The locations of the jets (in yellow) and the high purity tracks (in blue) are plotted against the azimuthal angle ϕ and pseudorapidity η. A rapidity gap is the range of η between the edge of the pixel tracker and the first high purity track. The gap measured from the forward edge of the tracker ($\eta = 2.5$) is designated "FRP", and likewise the gap measured from the backward edge of the tracker ($\eta = -2.5$) is designated "BRP". Both jets fall within $-1.8 < \eta < +1.8$. Notice that there is a large FRP gap.

Figure 5.13 is an example of a non-coherent dijet event display. Notice that both the BRP and FRP are small, corresponding to tracks covering a wide range of CMS pseudorapidity. This kind of event would be excluded by our rapidity gap selection.

Figure 5.14 shows the rapidity gap distribution for both the BRP and the FRP gaps. We note that

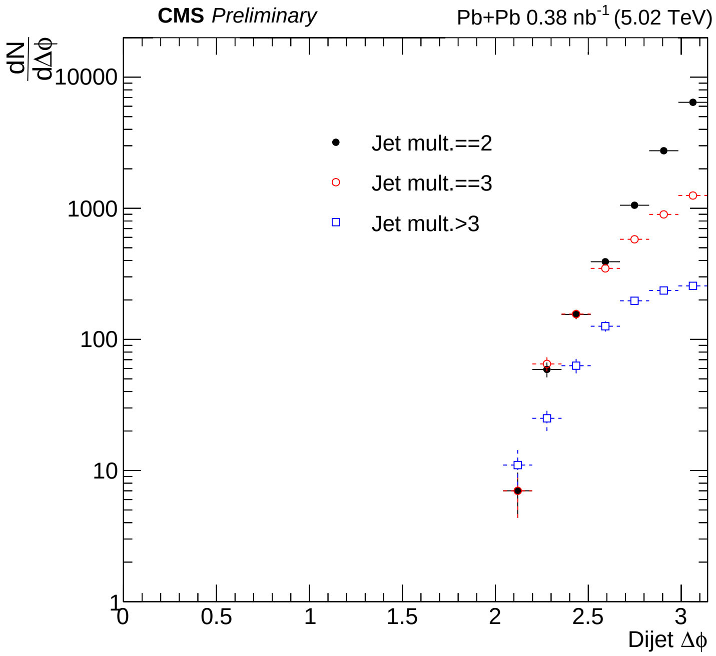

Figure 5.7: $\Delta\phi$ distribution for events that passed the event selection discussed in the text for the case where there is exactly one dijet (black points), exactly three jets (red points) and more than three jets (blue points).

most of the selected events seem to have a small rapidity gap. This comes from the complementary behavior of the BRP and FRP gaps. When the FRP gap is small (around 0 gap-size), the BRP gap will be large (from 1 to 3 gap-size); therefore, low peak in the FRP gap originates from events with a large BRP gap, and vice-versa. Figure 5.14 is thus the 1 dimensional projections of the 2 dimensional scatter plot, figure 5.15. Small rapidity gaps could also originate from two other scenarios: either the dijets are not from an exclusive-type process, or the tracks produced are located very close to the dijets in rapidity (resolved photon case discussed in Section 2.3).

Note that for UPC dijet production the gap will fall on the z+ or z- half of the CMS detector according to the direction of the incoming photon. If the incoming photon is moving towards the z+ direction, the rapidity gap will be on the z+ side of CMS, and vice versa. This can be seen in Figure 5.15 that shows the scatter plot between the BRP and FRP gaps for the coherent dijet sample. One can clearly see that the events are clustered around a larger BRP and a small FRP, or vice versa.

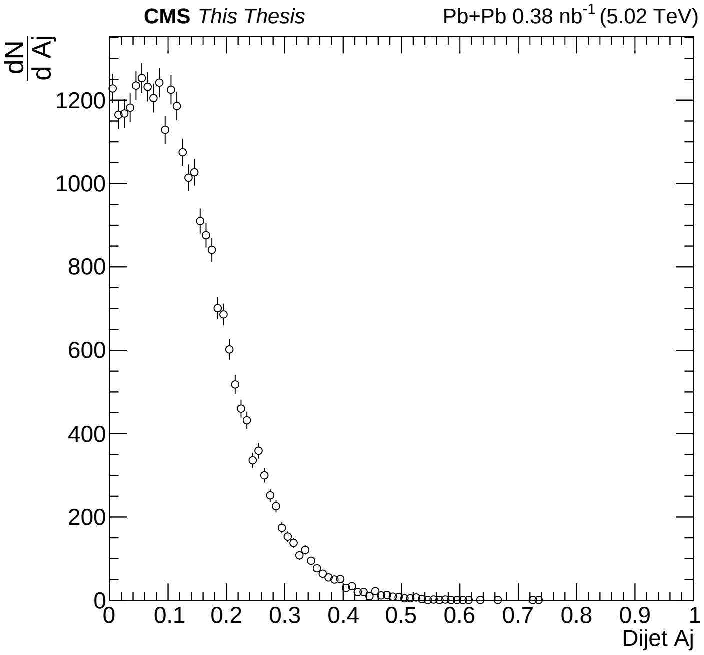

Figure 5.8: Momentum imbalance distribution (A_j) for UPC dijet candidates, *i.e.* events that have exactly one dijet and that have passed the various selections (see text for details).

Based on Figure 5.15, forward-going events are required to have BRP>1.2 and BRP > FRP while backward-going events were required to have FRP>1.2 and FRP>BRP.

The choice of BRP>1.2 can be justified in two ways. First, from a rule of thumb hadronic events are less likely to have a large empty region in the tracker. In a more quantitative way using the simulated response of CMS in the MC-sample discussed in the Monte Carlo Section, the BRP>1.2 selection can be justified since 98% of the reconstructed dijets that pass BRP>FRP also pass BRP>1.2.

Figure 5.16 shows the scatter plot between the BRP and the FRP gaps for the reconstructed coherent dijet events obtained from the RAPGAP + STARLIGHT Monte Carlo, confirming the large rapidity gap selection used in this analysis. Note that in the generated dijet events, only one of the photon directions has been simulated. For this reason, and contrary to Figure 5.15, only one of the two components is shown. For completeness, the projection of the rapidity gaps of the reconstructed MC events is shown in Figure 5.17 .

After applying the BRP and FRP requirements, we have studied the average rapidity distri-

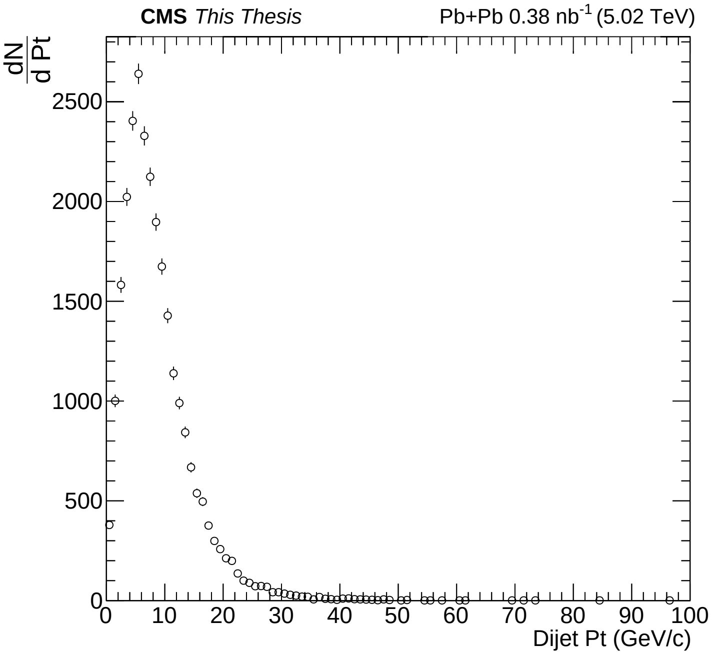

Figure 5.9: Transverse momentum distribution for the UPC dijet candidates (see text for details). This plot is consistent with the momentum imbalance distribution, confirming that the events are back-to-back balanced jets.

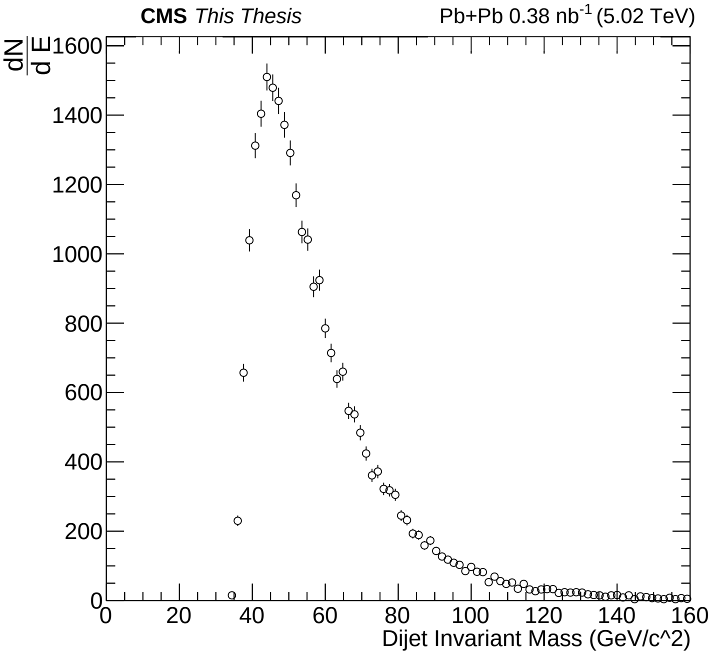

Figure 5.10: Invariant mass distributions for the UPC dijet candidates (see text for details).

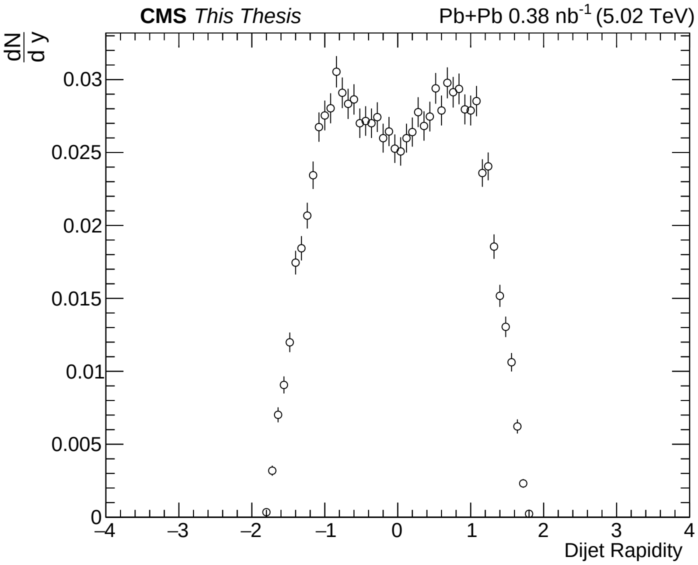

Figure 5.11: Dijet rapidity, after dijet event selection.

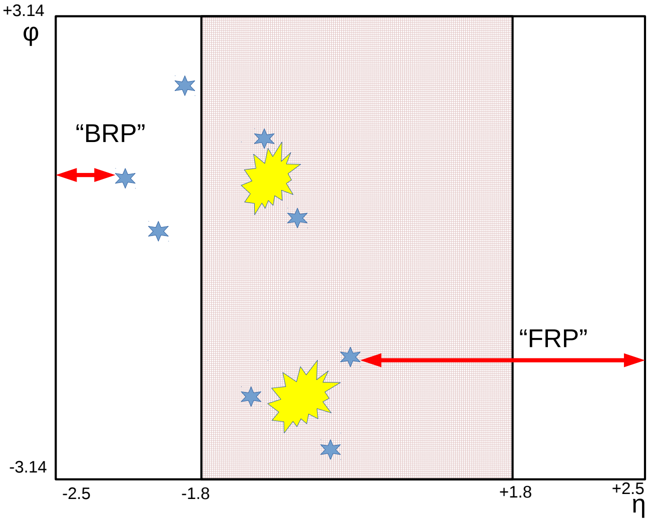

Figure 5.12: An example of an coherent dijet candidate, characterized by a large forward rapidity gap.

bution for the UPC dijets, as shown in Figure 5.18. The forward-going dijets are shown in blue (after applying the BRP gap requirement), while the backward-going dijets are shown in red (after applying the FRP gap requirement). The two distributions are highly symmetric, implying equal efficiency for selecting these events on either side of the CMS detector.

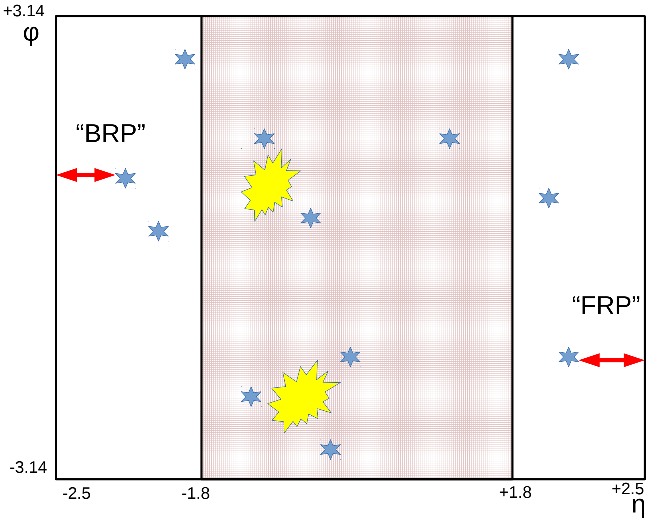

Figure 5.13: An example of a non-coherent dijet candidate, characterized by the absence of a large rapidity gap on either side of CMS.

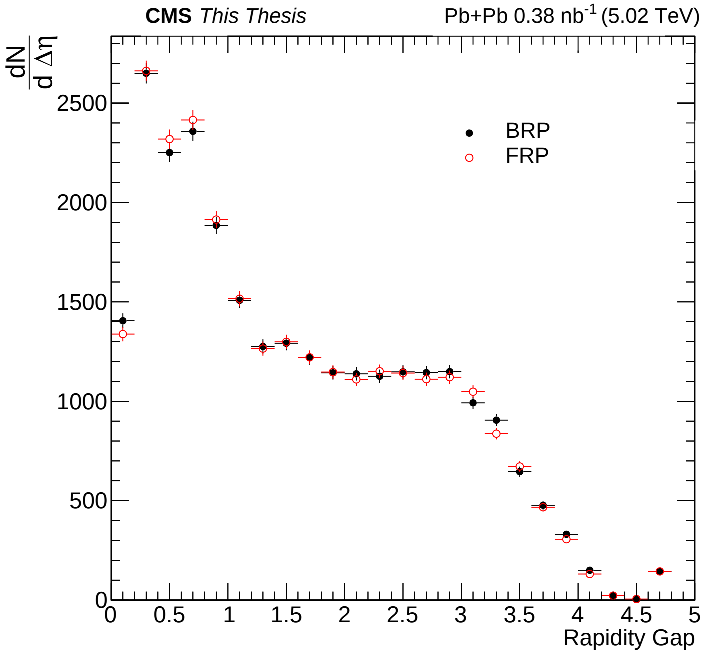

Figure 5.14: Rapidity gap distribution for the UPC dijet events for the backward (black points) and forward (red points) rapidity gaps.

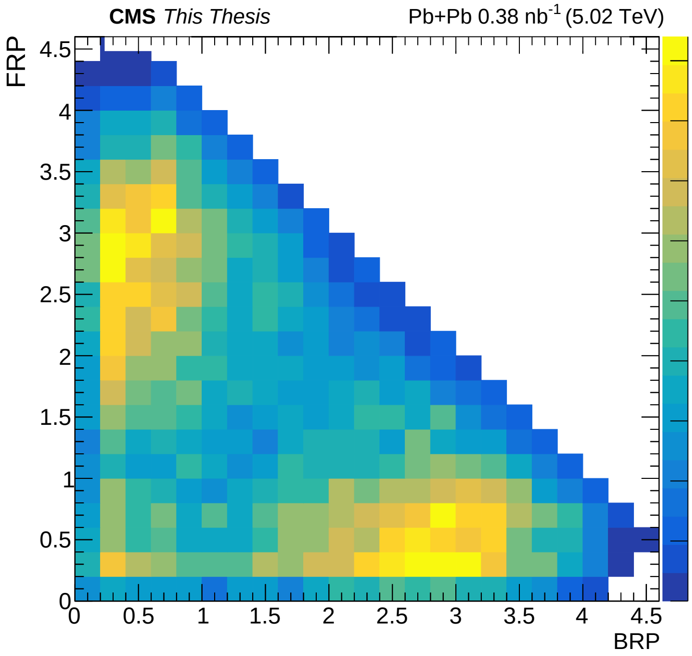

Figure 5.15: Scatter plot of the forward rapidity gap (FRP) versus the backward rapidity gap (BRP) for coherent dijet candidates.

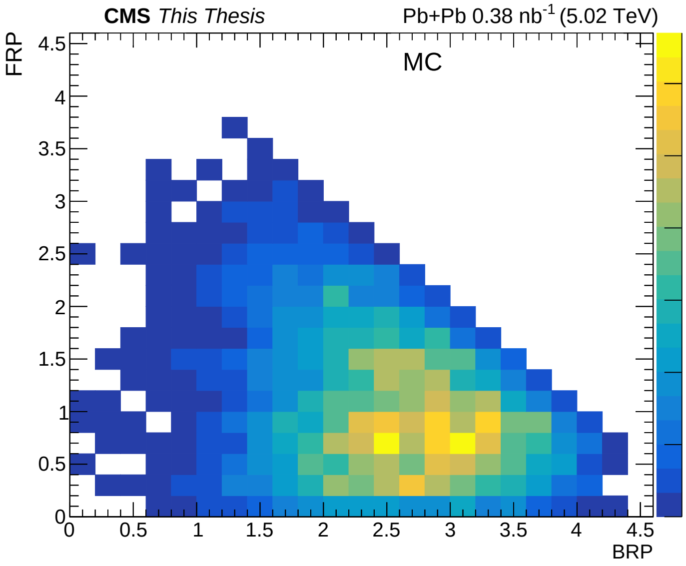

Figure 5.16: Scatter plot between the BRP and FRP for the UPC dijets from the reconstructed RAPGAP + STARLIGHT events. Only one of the two photon directions has been simulated.

5.3 v_2 measurement

To determine v_2, first the vector sum of the leading and subleading jets are defined by

$$\vec{Q}_T = \vec{k}_1 + \vec{k}_2 \tag{5.3}$$

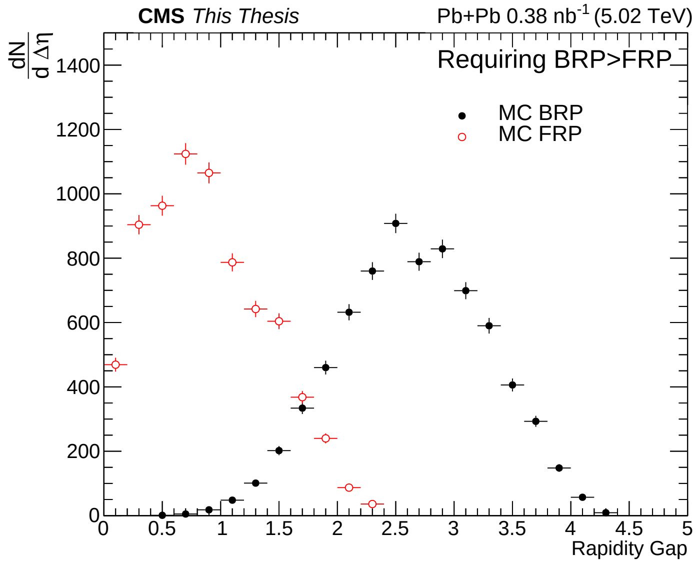

Figure 5.17: Projection of the BRP and FRP gap distributions from Figure 5.16.

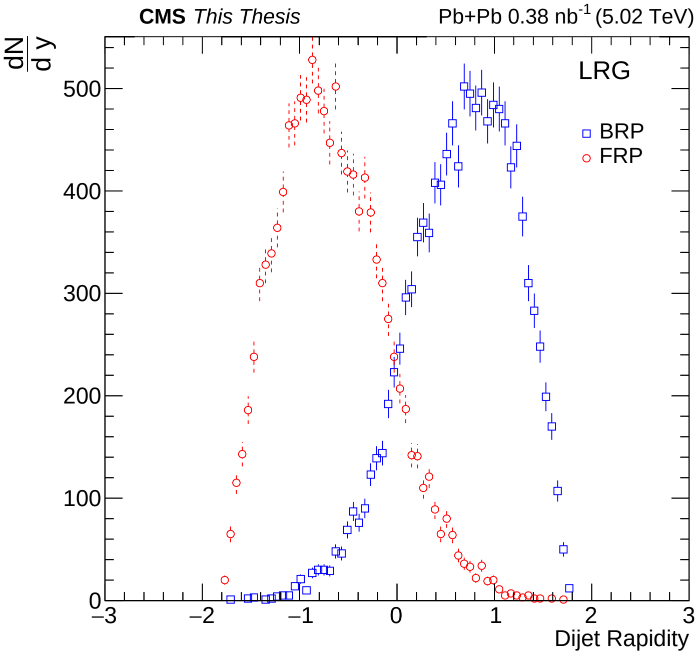

Figure 5.18: Average rapidity for the forward-going (blue points) and backward-going coherent dijets (red points).

and the vector difference by

$$\vec{P}_T = \frac{1}{2}(\vec{k}_1 - \vec{k}_2), \tag{5.4}$$

where $\vec{k_1}$ and $\vec{k_2}$ are the transverse momentum vectors of the leading and the subleading jets, respectively. Here leading jets are defined as the jets with the largest energy. The transverse momentum distributions for the leading and subleading jets after applying the large rapidity gap selection using the tracker are shown in Figure 5.19. The scalar product of both of these vectors determine the cosine of the angle between them

$$\cos(\phi) = \vec{Q}_T \cdot \vec{P}_T / (|| \vec{Q}_T || \cdot || \vec{P}_T ||) \tag{5.5}$$

and using trigonometric relationships one can obtain

$$v_2 = \langle \cos(2\phi) \rangle, \tag{5.6}$$

where ϕ is the angle between the $\vec{Q}_T$ and the $\vec{P}_T$ vectors, associated with the azimuthal anisotropy of the gluon distribution in the nuclear target. As mentioned in Section 2.4, several theorists [108] have suggested measuing such an angular correlation. It is important to mention here that although some authors suggest that their calculations are only valid in the so-called "correlation limit", also known as the back-to-back limit or TMD limit ($Pt \gg Q$), the analysis performed in this thesis has all the data with $Pt > Q$, yet it is not much larger. Covering such a region requires much larger statistics or focusing in the lowest Q_T region in this analysis.

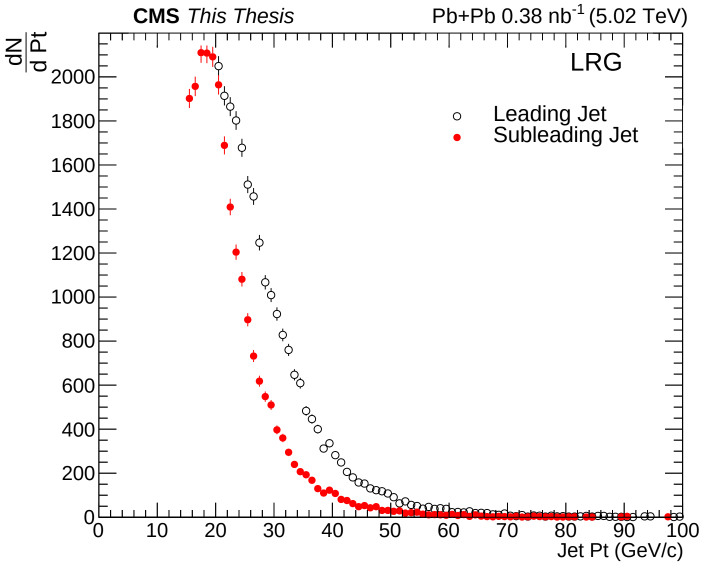

Figure 5.19: Transverse momentum for the leading and subleading jets, after dijet event selection including the large rapidity gap selection (LRG). The LRG selection requires that an event pass either the BRP or FRP selection.

Figure 5.20 is an illustration of the relationship between the dijet vectors $\vec{k}_1$ and $\vec{k}_2$, the vectorial sum $\vec{Q}_T$ and the vectorial difference $\vec{P}_T$, and the correlation angle ϕ.

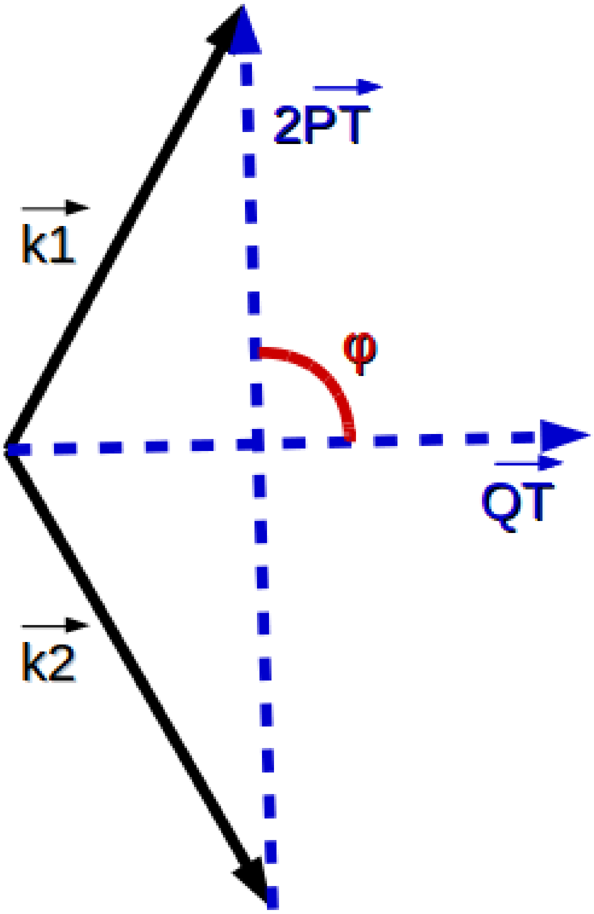

Figure 5.20: Diagram showing the relationship between $\vec{k}_1$,$\vec{k}_2$, $\vec{Q}_T$, $\vec{P}_T$, and ϕ.

As mentioned in Chapter 2, the angular correlation analysis is defined in terms of two variables, namely, the vector sum (Q_T) and the vector difference (P_T) of the leading and sub-leading jets. Figure 5.21 shows the Q_T and P_T of data. In order to study the kinematics of coherent dijets, we have to study the scatter plot between both variables, as shown in Figure 5.22. Note that both the forward-going and backward-going dijets have been merged together in one sample here. We note that most of the events have both low Q_T and low P_T. This is not surprising since the photoproduced events are expected to have a small Q_T.

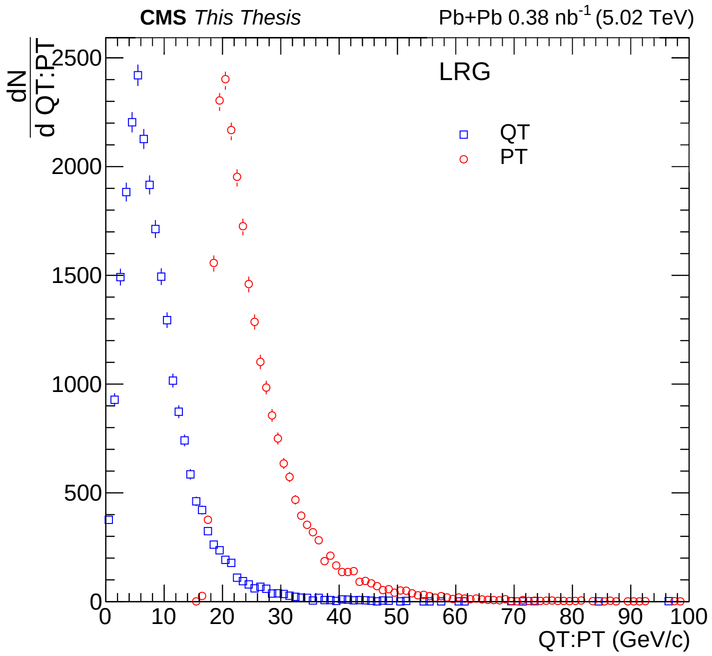

Figure 5.21: Vector sum (Q_T) and vector difference (P_t) of the leading and sub-leading jets for the selected events. Both the forward-going and backward-going dijets have been merged together in one sample.

5.3.1 Raw v_2 distributions

Using the procedure described above, the angular distribution $\frac{dN}{d\phi}$ has been measured. Figure 5.23 shows the angular distribution for coherent dijet events that do not have the large rapidity gap requirement; UPC dijet events that have the large rapidity gap (BRP or FRP), and UPC dijet events where both BRP and FRP configurations have been merged into one sample. One can observe that in all these cases there are events peaked approximately around π which is consistent with longitudinal polarization. This is interesting and somewhat surprising since one would expect that in UPC dijets most of the events will be from transversally polarized photons due to helicity conservation.

In addition, we have studied the distribution for both the generated and reconstructed RAPGAP + STARLIGHT dijet events. Figure 5.24 shows the results for the generated events, and Figure 5.25 shows the results for the reconstructed events.

The comparison between the average v_2 between the reconstructed data, after applying all

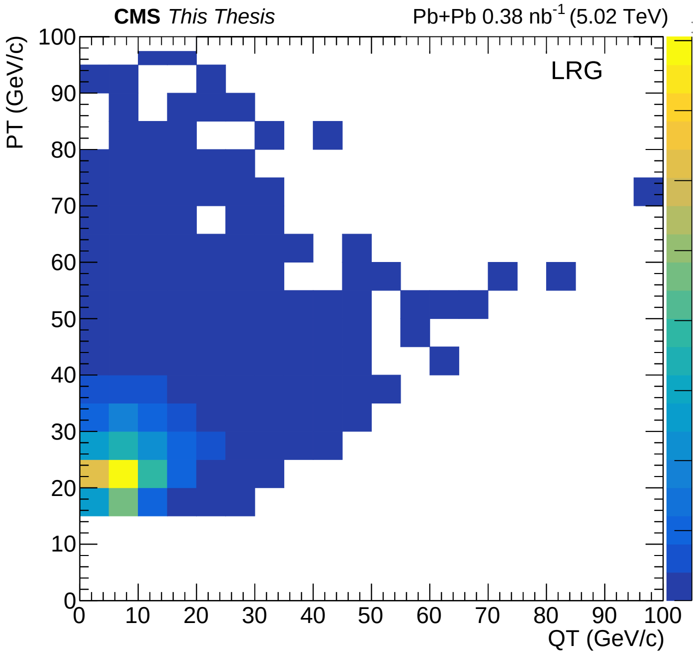

Figure 5.22: Scatter plot between the vector sum (Q_T) and vector difference (P_t) of the leading and sub-leading jets for the selected events. Both the forward-going and backward-going dijets have been merged together in one sample.

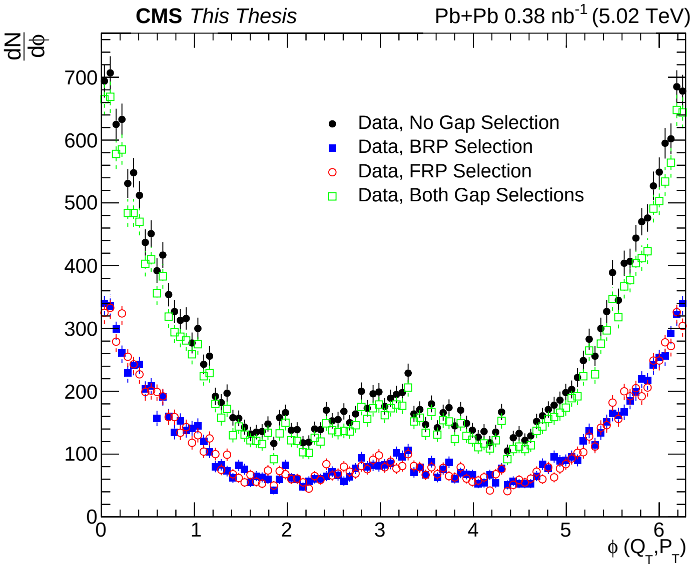

Figure 5.23: Raw ϕ distribution in data for the following cases: no requirement on large rapidity gaps (black points), BRP selection (blue points), FRP selection (red points) and combined BRP and FRP sample (green points).

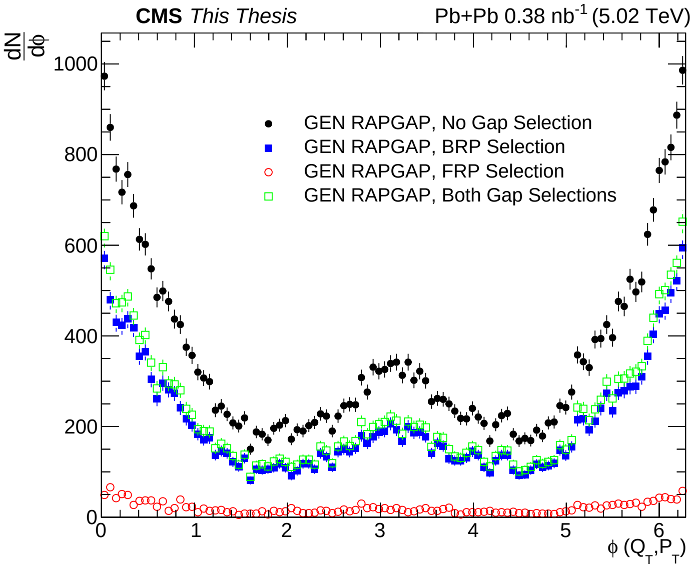

Figure 5.24: Same-event ϕ for the generated RAPGAP + STARLIGHT dijet events.

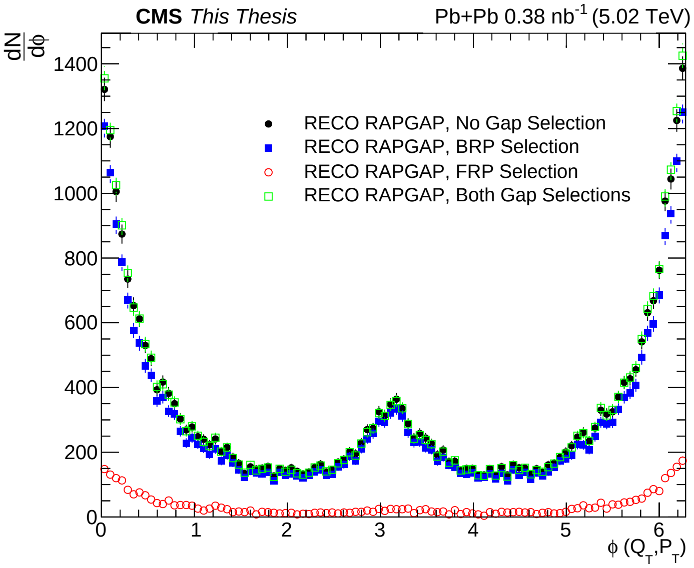

Figure 5.25: Same-event ϕ for the reconstructed RAPGAP + STARLIGHT dijet events.

the event selections mentioned above, and the average v_2 obtained from the generated RAPGAP+STARLIGHT dijet events is shown in Figure 5.26, as a function of the vector sum Q_T. One can see that the average $v2$ value is flat across this variable, and there is a good agreement between the reconstructed data results and the generated events, indicating that the background and resolutions corrections are, in principle, small for the case of the data integrated over P_T.

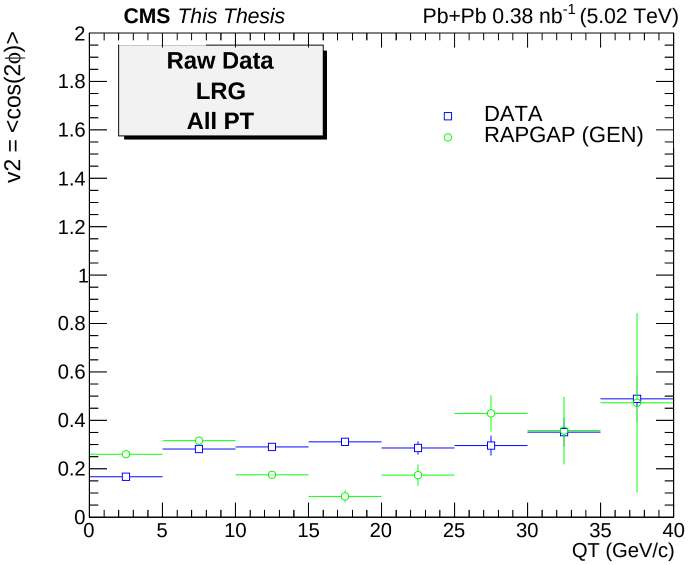

Figure 5.26: Average reconstructed v_2 distribution for data, compared to the generated v_2 distribution obtained from RAPGAP + STARLIGHT.

5.3.2 Mixed event results

In practice v_2 is sensitive to the acceptance of the CMS detector which may produce a non-zero v_2 in the absence of any true physics correlation. The acceptance is accounted for using the event mixing method. Each dijet event is mixed with a series of other events that have a vertex close to the original event and their leading and subleading jets swapped. The mixed events are also subject to the same selection on Q_T as the real events. For the mixed events there is no physical relationship between the leading and subleading jets. Therefore v_2 for mixed events depends only upon the detector acceptance effects. The v_2 of mixed events effects are in turn subtracted from our final result, although results without the mixed-event subtraction are also presented. Each event that passes our selection is mixed with five other events to produce five mixed-dijet candidates. Note that in order to be mixed, each event has to have only one dijet.

Figure 5.27 shows the $\frac{dN}{d\phi}$ distribution for the mixed-events data. Figure 5.28 shows the mixed-event Q_T and P_T distribution, and Figure 5.29 shows the scatter plot between these two variables. The dijet rapidity and the dijet invariant mass distributions for the mixed-event sample are shown in Figure 5.30 and Figure 5.31, respectively. It is interesting to notice that the Q_T distribution for the mixed-event sample is very different from that of the same-event sample, indicating that the analyzed events are indeed from the UPC dijet process and not from a acceptance effect.

The shape of the mixed-event angular distribution originates from the pure kinematics and the analysis requirements. This has been confirmed from studying the a toy MC using a random generator.

It is importnat to notice that the theoretical studies reported in the literature do not make any mention to the angular correlation due to the mixed-event distribution and whether this should be taken into account in the measurement. We have presented some of the results in such a way, following the standard procedure in flow studies in nucleus-nucleus collsions, while this assumption is not fully justified at present.

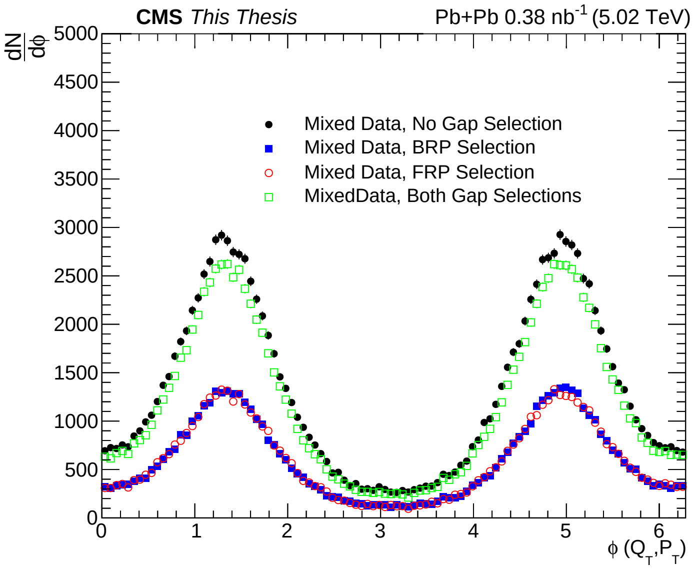

Figure 5.27: ϕ distribution for the mixed-event data for coherent dijet candidates.

From the results shown in Figure 5.27 we have measured the average of the v_2 distribution as a function of Q_T (see Figure 5.32). The subtracted result is given by $v_2^{raw} - v_2^{mixed}$, and the distribution is shown in Figure 5.33.

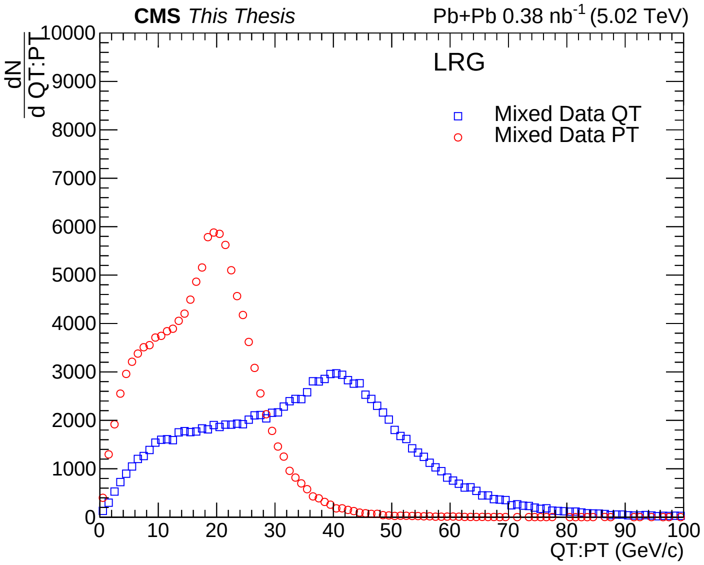

Figure 5.28: Mixed data Q_T and P_T distributions.

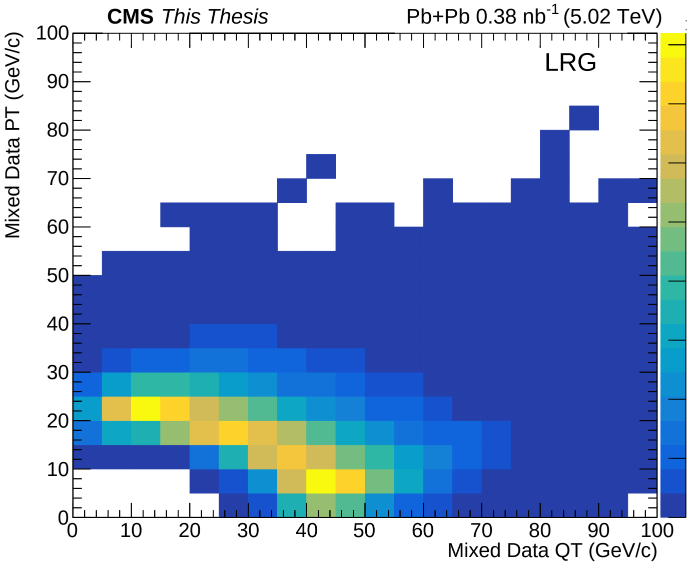

Figure 5.29: Mixed data dijet Q_T and P_T scatter plot.

5.3.3 Resolution correction

To get the true v_2 it is also necessary to apply a correction for the experimental resolution in estimating the ϕ angle. The correction factor R is computed as $(v_2^{Reco} - v_{2,Mixed}^{Reco})/(v_2^{Gen} - v_{2,Mixed}^{Gen})$, where v_2^{Reco} is obtained from reconstructed events, and v_2^{Gen} from generated events. This factor

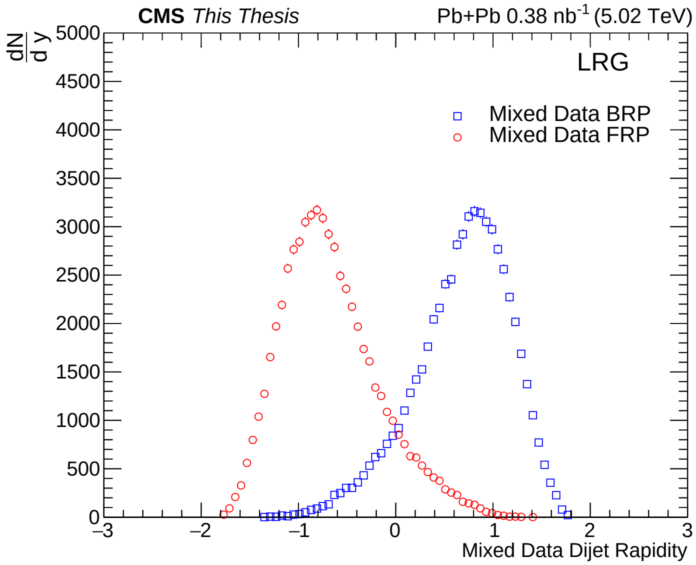

Figure 5.30: Mixed data dijet rapidity distributions.

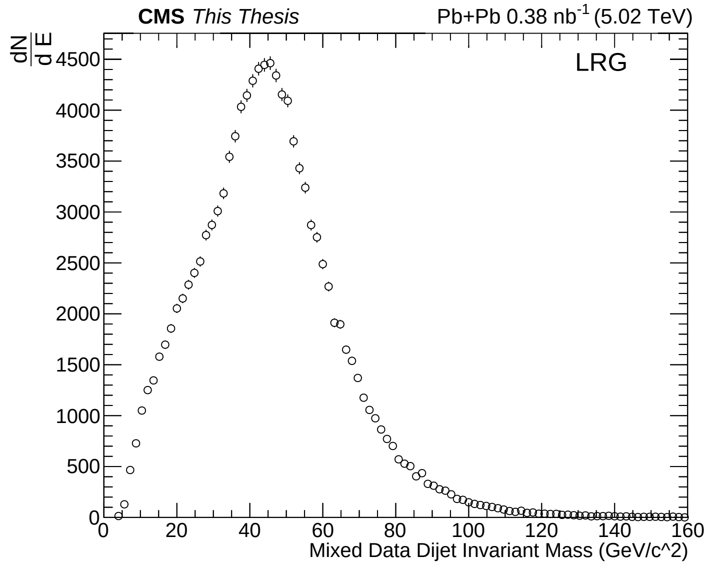

Figure 5.31: Mixed data dijet invariant mass distributions.

is estimated from Monte Carlo studies using RAPGAP and found to be approximately one for the various ϕ region. Figure 5.34 shows the R factor as a function of Q_T for the coherent dijet candidates.

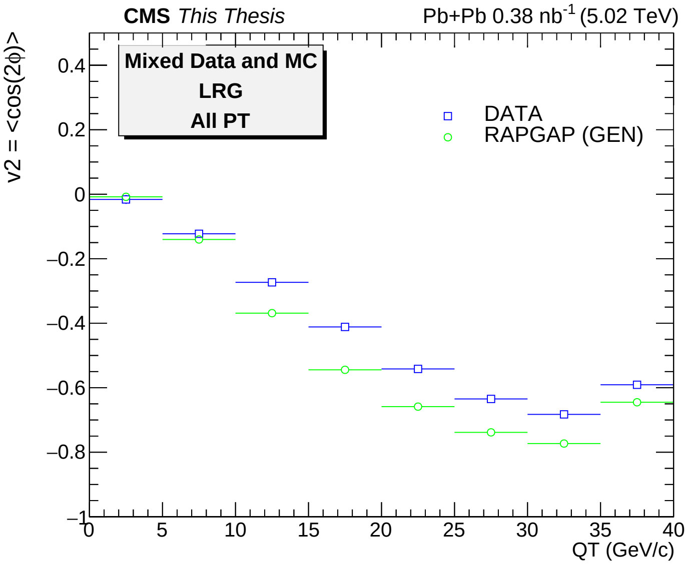

Figure 5.32: Mixed-event result for the average v_2; data is mixed, MC is mixed.

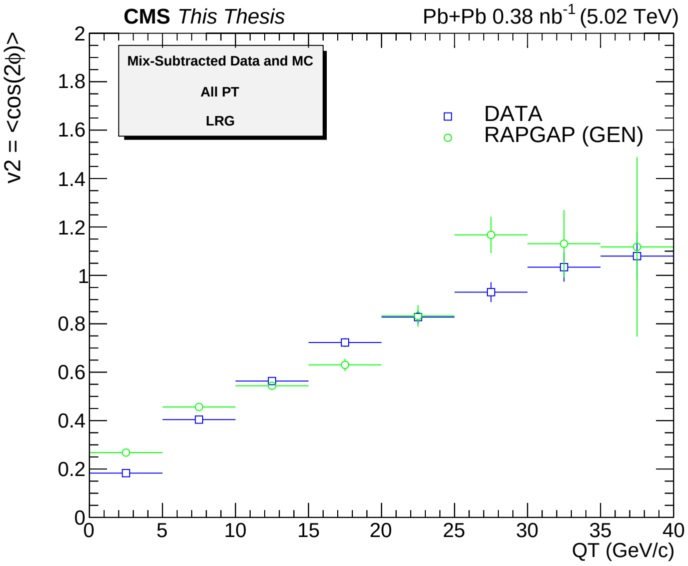

Figure 5.33: Subtracted result; $v_2 = v_2^{raw} - v_2^{mixed}$.

5.3.4 Corrected v_2

Thus, the final value of v_2 is given by $v_2 = \frac{v_2^{raw} - v_2^{mixed}}{R}$, where R is the resolution correction factor. This is shown in Figure 5.35, where each bin in QT is given an R factor.

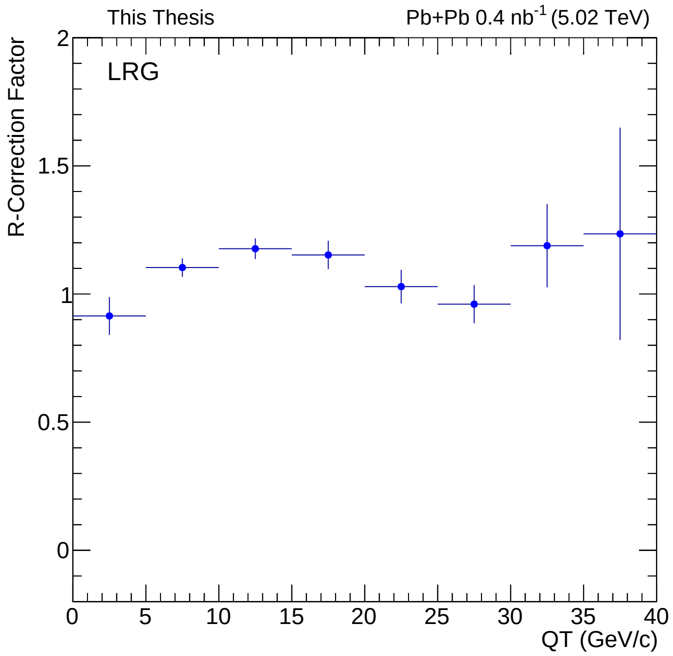

Figure 5.34: Correction factor R.

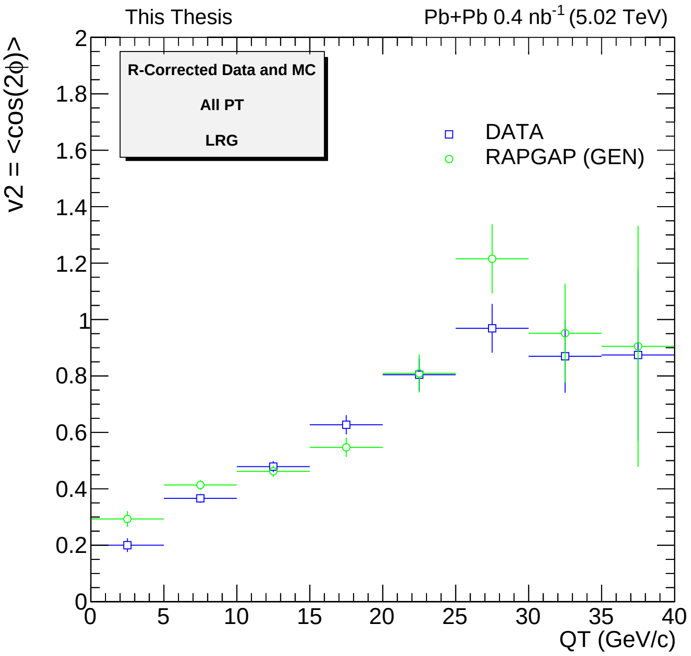

Figure 5.35: Corrected v_2 distribution for the coherent dijet candidates.

5.4 v_2 differential analysis

Before discussing the assessment of the systematic uncertainties, we will apply some kinematic selections on the UPC dijet candidates. In particular, the UPC dijets are required to have a $Q_T < 20$ GeV and a $P_T < 40$ GeV since this is the region where most of the events are present in data.

Furthermore, the angular correlation analysis will depend on the energy of the photon-lead center-of-mass system ($W_{\gamma+Pb}$). This can be estimated using the following equation

$$W_{\gamma+Pb} = 2E_{Pb}M_{Inv}e^{-y}, \tag{5.7}$$

where E_{Pb} is the energy of the target, M_{Inv} is the invariant mass of the dijet system, and y is the dijet rapidity. As shown in this formula there is a two-fold ambiguity in the photon direction at $y \neq 0$. Since we have the dijet samples in the forward-going or backward-going directions, any energy-dependent analyses will have to be done separately for each direction.

The scatter plot between the invariant mass and the rapidity for the UPC dijets is shown in Figure 5.36 for the BRP selection, and in Figure 5.37 for the FRP selection. In addition, the equivalent plot for the RAPGAP + STARLIGHT sample is shown in Figure 5.38.

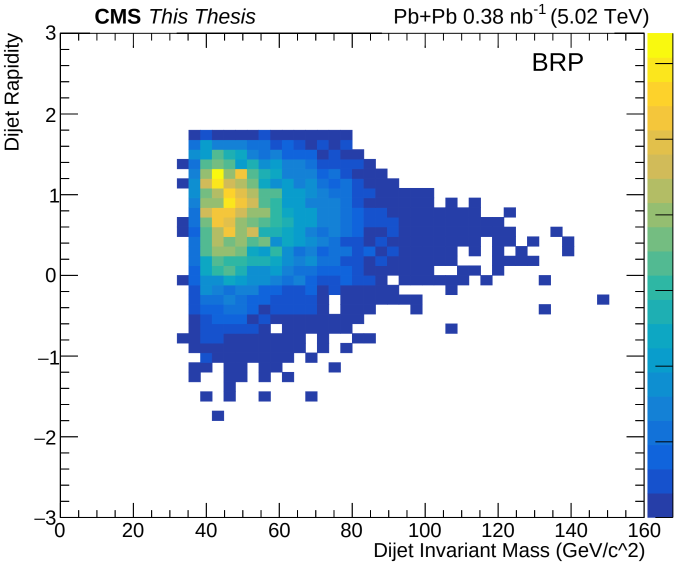

Figure 5.36: Scatter plot between the dijet rapidity and dijet invariant mass for BRP in data and requiring $Q_T < 20$ GeV and $P_T < 40$ GeV.

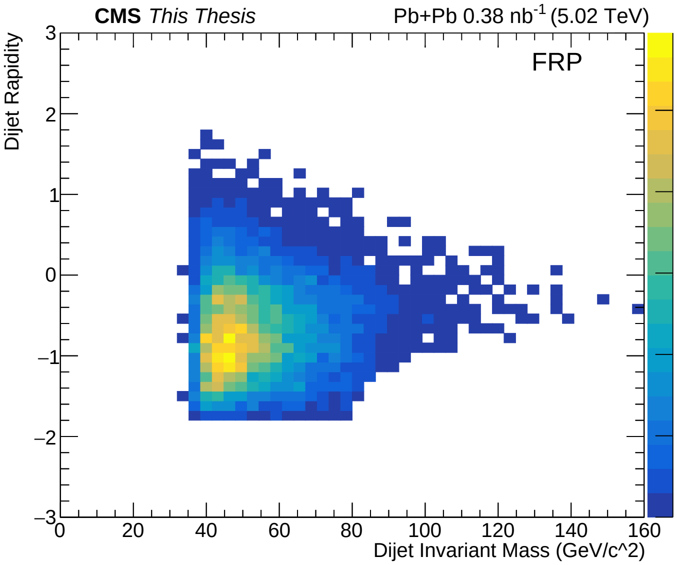

Figure 5.37: Scatter plot between the dijet rapidity and the dijet invariant mass for FRP in data and requiring $Q_T < 20$ GeV and $P_T < 40$ GeV.

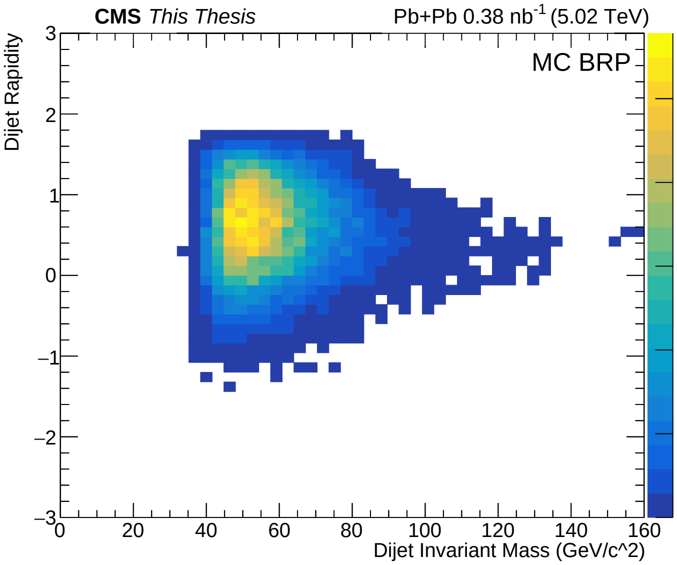

Figure 5.38: Scatter plot between the dijet rapidity and dijet invariant mass for BRP in the RAPGAP+STARLIGHT and requiring $Q_T < 20$ GeV and $P_T < 40$ GeV.

From these results and using the formula mentioned above, we have decided to focus in the following three different kinematic regions:

- Region I: BRP region with $Q_T < 20$ GeV and $P_T < 40$ GeV;

- Region II: BRP region with $Q_T < 20$ GeV and $P_T < 40$ GeV, and $40 < M_{Inv} < 60$ GeV, and $-1.8 < y < 0$, and
- Region III: BRP region with $Q_T < 20$ GeV and $P_T < 40$ GeV, and $40 < M_{Inv} < 60$ GeV, and $0 < y < 1.8$.

By studying Region II and Region III, it is possible to study the energy dependence of the angular correlations in the kinematic region with the larger sample size. Since the results for BRP and FRP are consistent to each other, and for the simplicity of the presentation of the results, all the following studies are carried out for the BRP region only. In the section related to the systematic uncertainties we provide further comparisons between the BRP and FRP regions.

5.4.1 Raw v_2 distributions

Figure 5.39 shows the raw v_2 results as a function of Q_T (top plots) and P_T (bottom plots) for Region I (left), Region II (middle) and Region III (right). We observe that the raw v_2 results are flat as a function of Q_T. We also note that the raw v_2 results as a function of P_T tend to increase as P_T increases. In particular in Region III in the interval between 30 and 35 in P_T, the value of raw v_2 reaches 1.

5.4.2 Mixed event results

Figure 5.40 shows the mixed-event v_2 results as a function of Q_T (top) and P_T (bottom) for Region I (left), Region II (middle) and Region III (right). For the mixed-event v_2 as a function of Q_T, we observe that v_2 decreases as Q_T increases. This is in contrast to the mixed-event v_2 as function of P_T that increases as P_T increases going from -1 to 1. Note that these values correspond to back-to-back events.

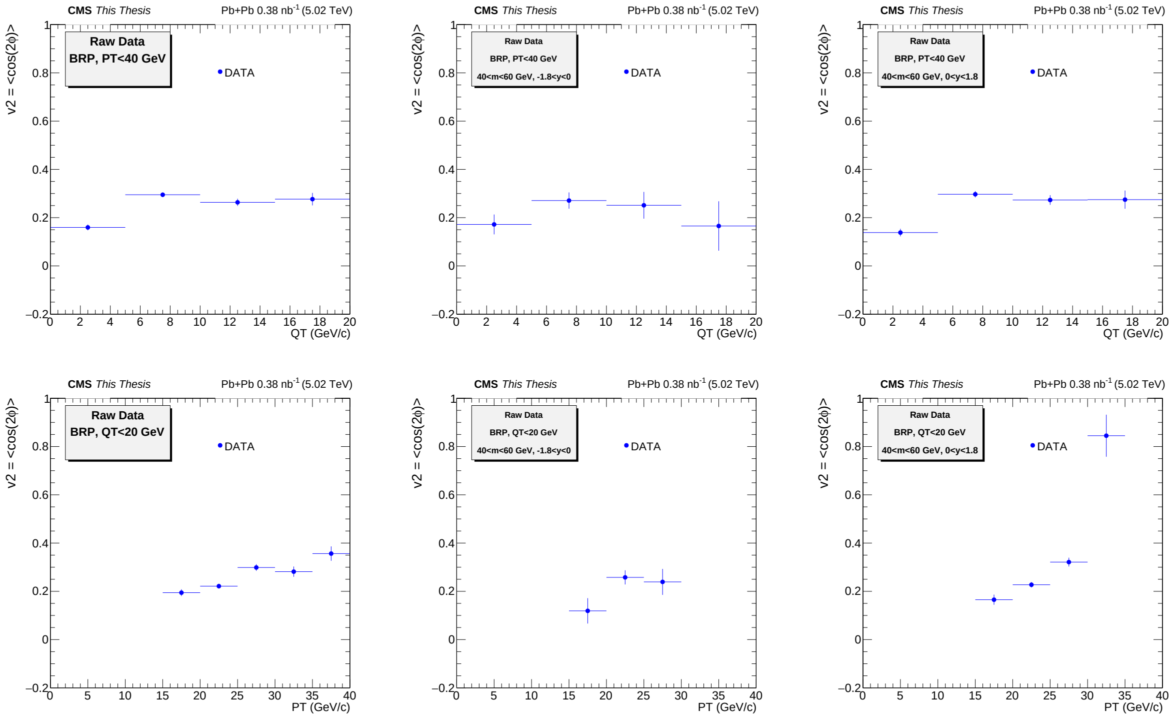

Figure 5.39: Raw v_2 distributions for Regions I, II, and III.

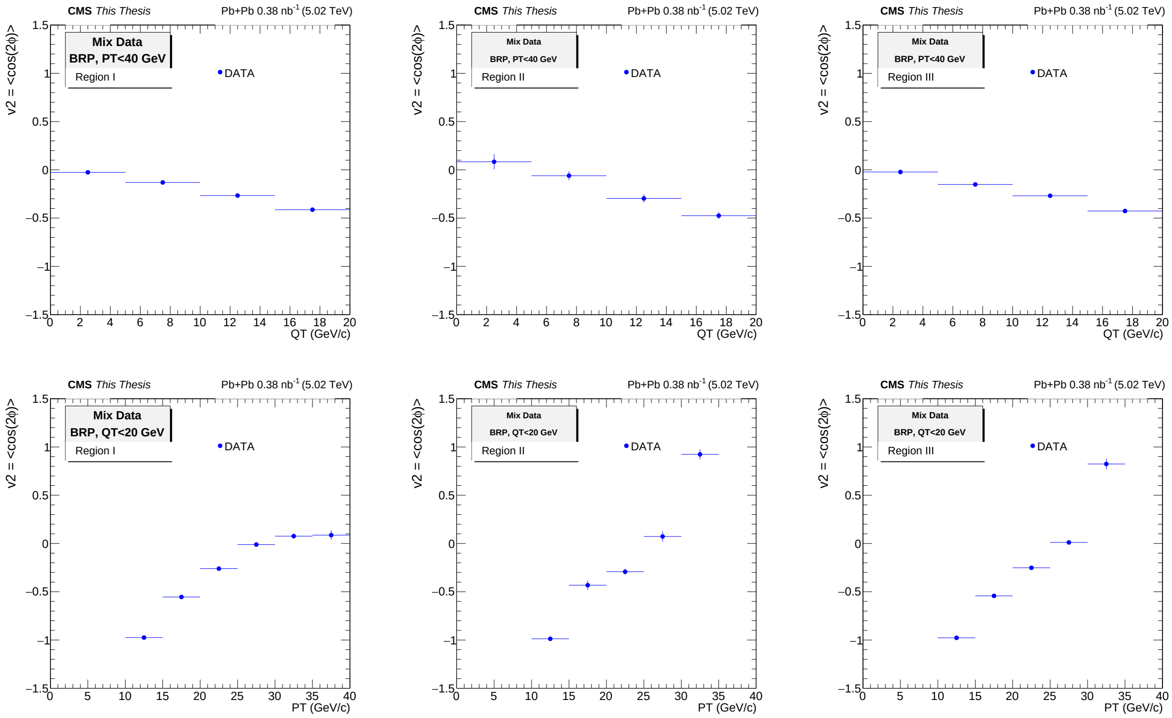

Figure 5.40: Mixed v_2 distributions for Regions I, II, and III.

5.4.3 Subtracted event results

Figure 5.41 shows the v_2 results (raw v_2 subtracted by the mixed-event v_2) as a function of Q_T (top plots) and P_T (bottom plots) for Region I (left corner), Region II (middle plots) and Region III (right corner). The subtracted results show the same trend reported above. We do not observe a significant difference in any of the so-called regions.

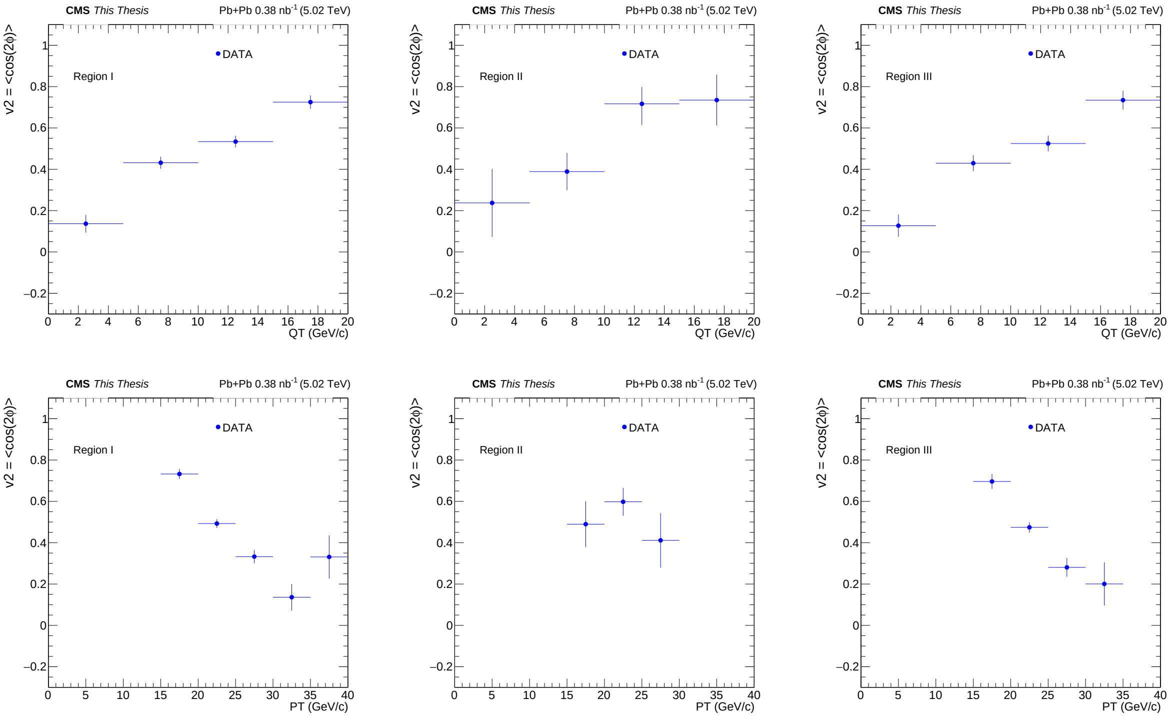

Figure 5.41: Mix-subtracted v_2 distributions for Regions I, II, and III.

5.4.4 Resolution correction

Figure 5.42 shows the resolution correction factor, defined above, as a function of Q_T (top) and P_T (bottom) for Region I (left), Region II (middle) and Region III (right). Notice that, for the bottom right plot, corresponding to the resolution correction as a function of P_T in Region III, the 30 - 35 GeV/c bin is empty. The bin is empty because the RAPGAP+STARLIGHT sample has no events in this specific kinematic region. As such, this bin will be empty in this region for corrected v_2 plots.

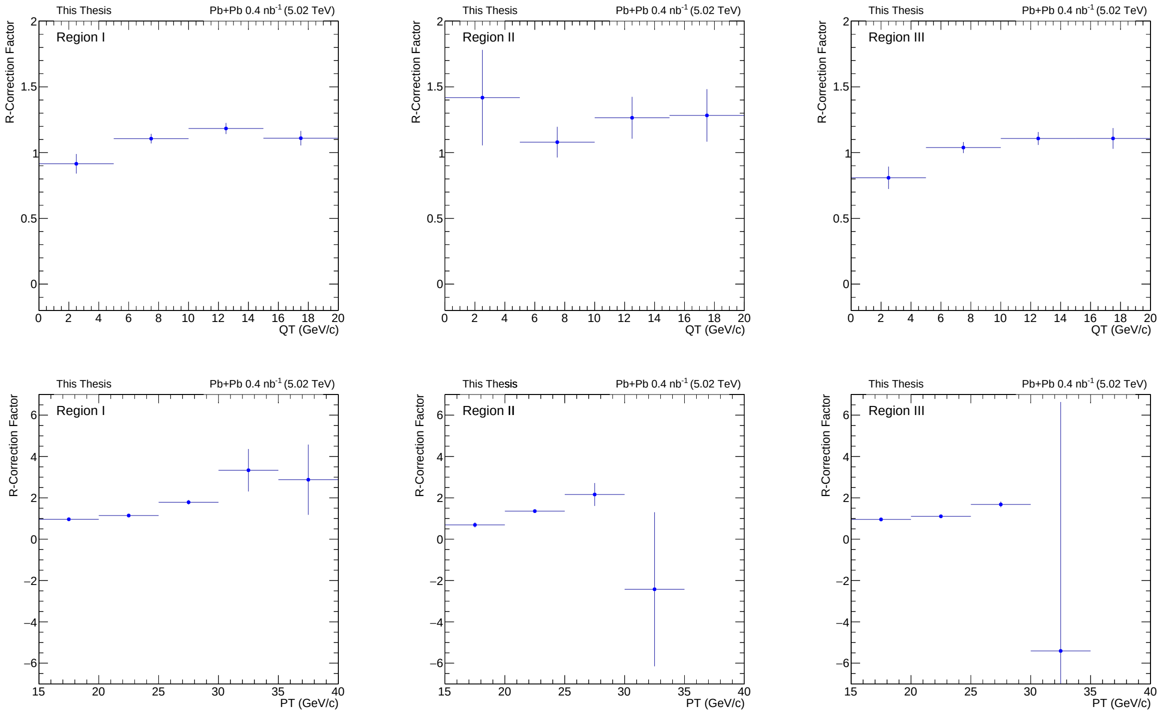

Figure 5.42: Resolution correction of v_2 distributions for Regions I, II, and III.

5.4.5 Corrected v_2

Figure 5.43 shows the corrected v_2 results as a function of Q_T (top) and P_T (bottom) for Region I (left), Region II (middle) and Region III (right). Before discussing these results, let us discuss the assessment of the systematic uncertainties in the next section.

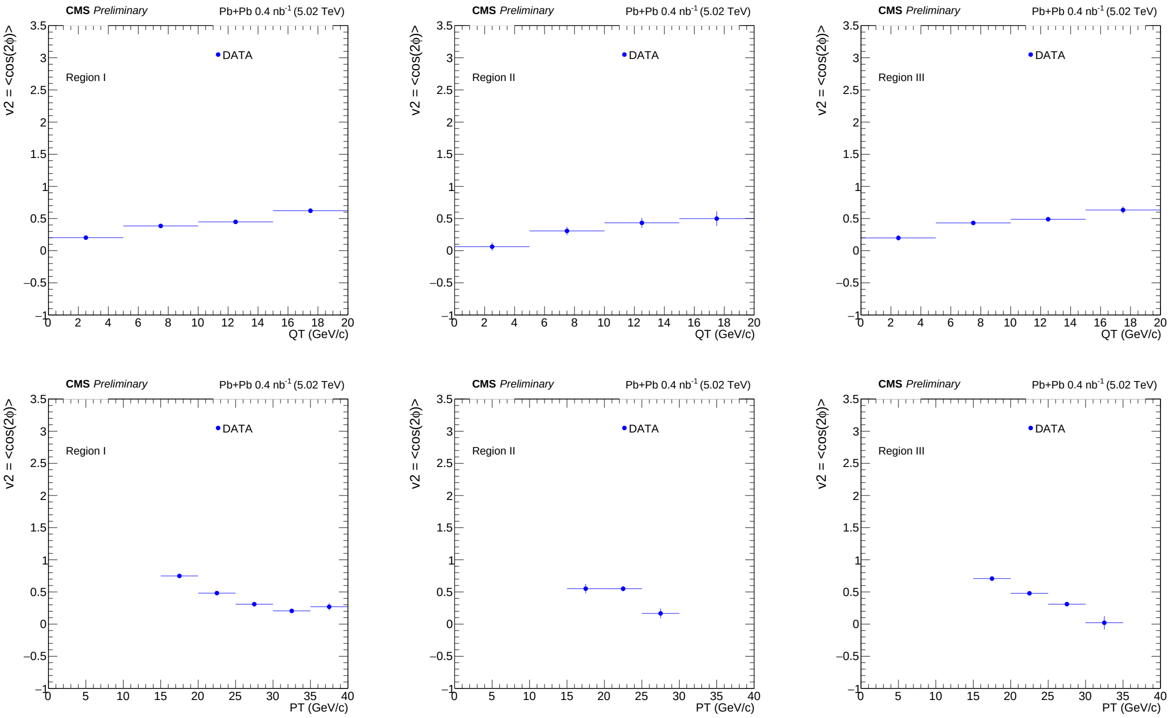

Figure 5.43: Corrected v_2 distributions for Regions I, II, and III.

Chapter 6

Systematic uncertainties

Several cross checks are preformed to test the robustness of the analysis, and the following sources of systematic uncertainties are assessed: detector symmetry, vertex selection, jet p_T selection, and resolution correction factor.

6.1 Detector symmetry

The symmetry of the detector is estimated by comparing events with jets at positive rapidity to those with jets at negative rapidity (comparison between the BRP and FRP results). No significant change in v_2 is observed, as can be observed in Figure 6.1. Table 6.1 contains the v_2 systematic error from detector symmetry. The percent systematic error here was calculated by taking the difference of the v_2 calculated for the BRP and FRP regions.

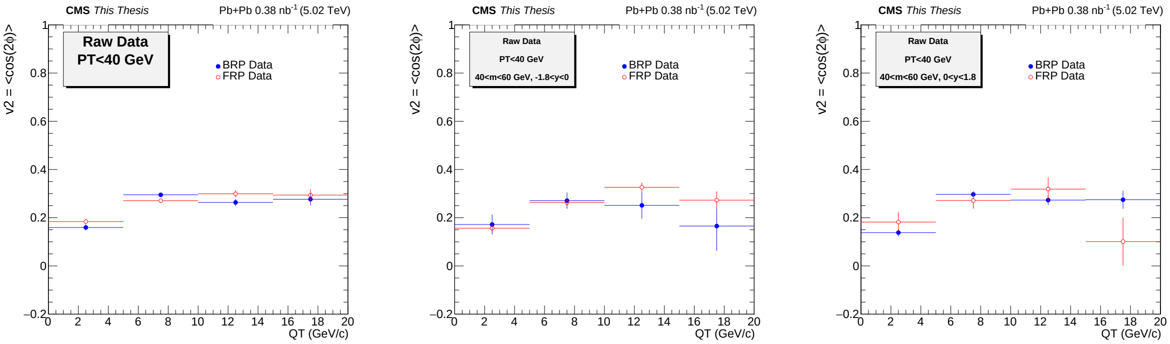

Figure 6.1: Raw data, differential analysis regions, LRG selection systematics on v_2. The BRP results (blue points) and the FRP results (red points) are compared.

QT Bin (in GeV/c)	Region I (%)	Region II (%)	Region III (%)
1-5	4.7	6.7	10.1
5-10	4.0	1.8	3.9
10-15	5.7	12.2	7.1
15-20	2.2	12.3	21.7

Table 6.1: Table of v_2 systematic uncertainties from LRG selection.

6.2 Vertex requirement

The vertex requirement is tightened from ± 20 cm to ±7 cm. Figure 6.3 shows v_2 as a function of Q_T calculated from the nominal event selection (black solid points) and by a selection varying the vertex selection (red hollow points); to vary the vertex selection, we reduced the vertex z-position cut from $|vz| < 20$ cm to $|vz| < 13$ cm. Table 6.2 shows a table of the v_2 systematic uncertainties from the vertex selection.

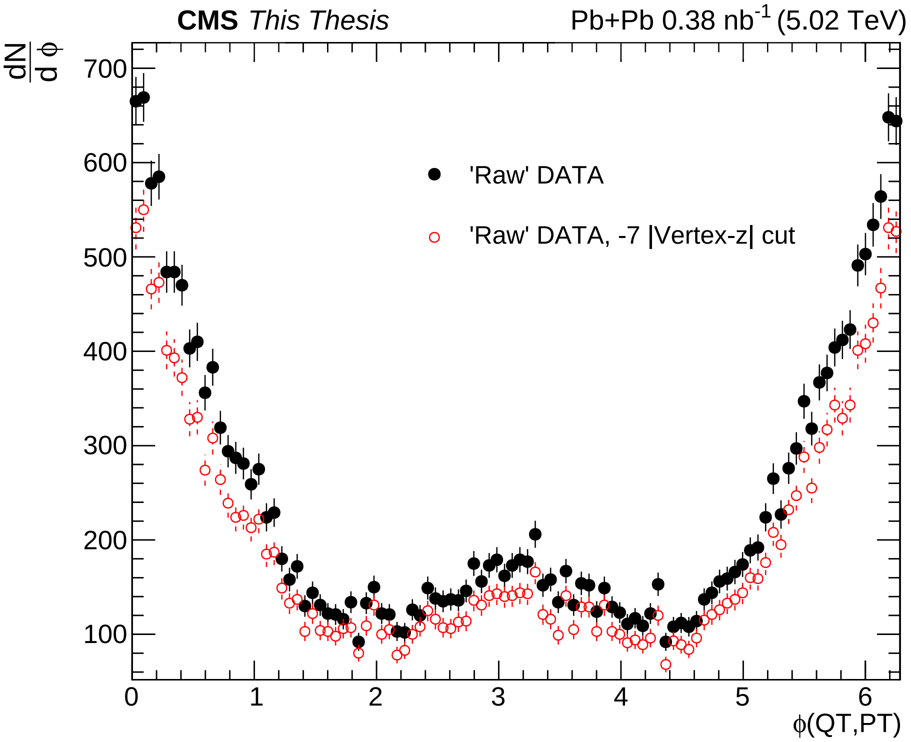

Figure 6.2: Angular correlation for the nominal analysis, and after changing the vertex requirement from ± 20 cm to ± 7 cm.

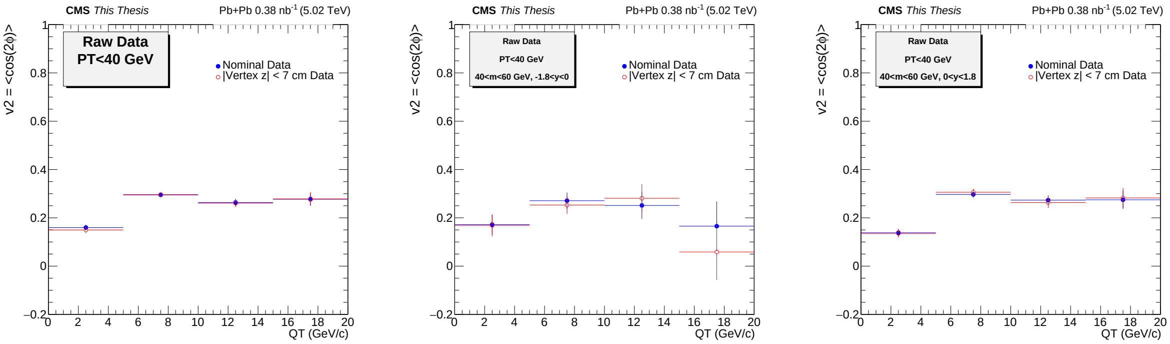

Figure 6.3: Raw data, differential analysis regions, vertex selection systematics on v_2. The nominal results (blue points) and the vertex-cut varying results (red points) are compared.

QT Bin (in GeV/c)	Region I (%)	Region II (%)	Region III (%)
1-5	1.9	1.5	0.7
5-10	0.2	4.2	1.4
10-15	0.5	4.8	1.5
15-20	0.2	12.2	1.0

Table 6.2: Table of v_2 systematic uncertainties from the vertex selection.

6.3 Energy scale

The p_T thresholds for the leading and subleading jets are changed by $+1$ GeV/c. Figure 6.4 shows the ϕ distribution for the nominal event selection, and by a selection that increases the jet p_t cuts by 1 GeV/c. Figure 6.5 shows the v_2 as a function of Q_T under the nominal event selection, and after varying the jet p_t cuts. Table 6.3 shows the v_2 systematic uncertainties from the jet p_t selection. Note that Region II has low statistics at high QT.

QT Bin (in GeV/c)	Region I (%)	Region II (%)	Region III (%)
1-5	0.3	15.0	6.3
5-10	0.1	1.5	1.0
10-15	1.3	10.5	3.5
15-20	2.4	10.0	8.3

Table 6.3: Table of v_2 systematic uncertainties from the jet p_t selection.

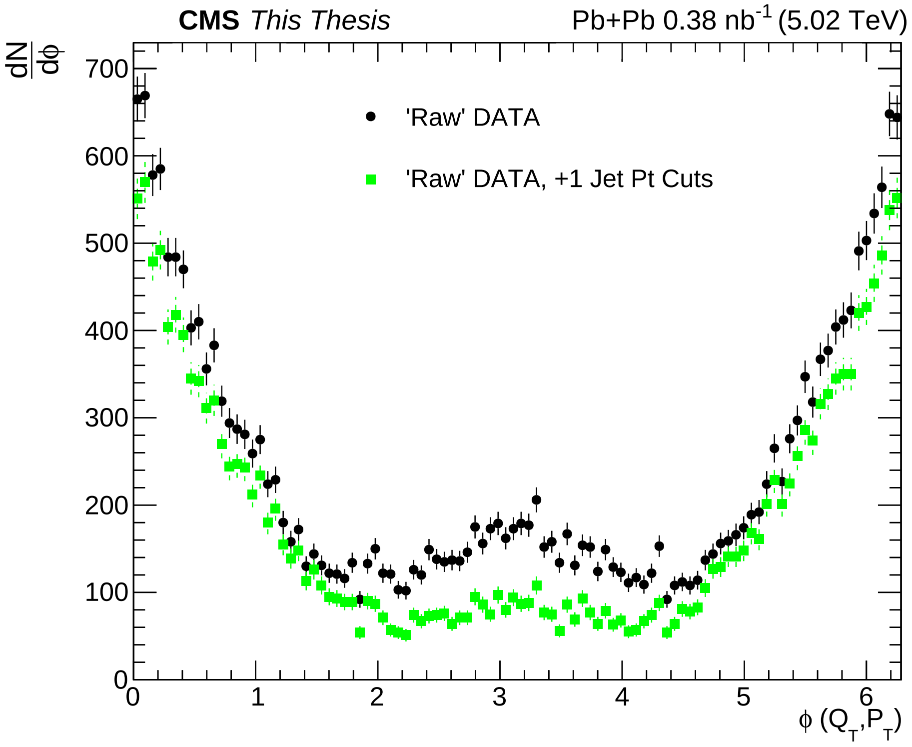

Figure 6.4: Angular correlation of the UPC dijet analysis for the nominal analysis, and that after increasing by 1 GeV both the leading and subleading p_t of the jets.

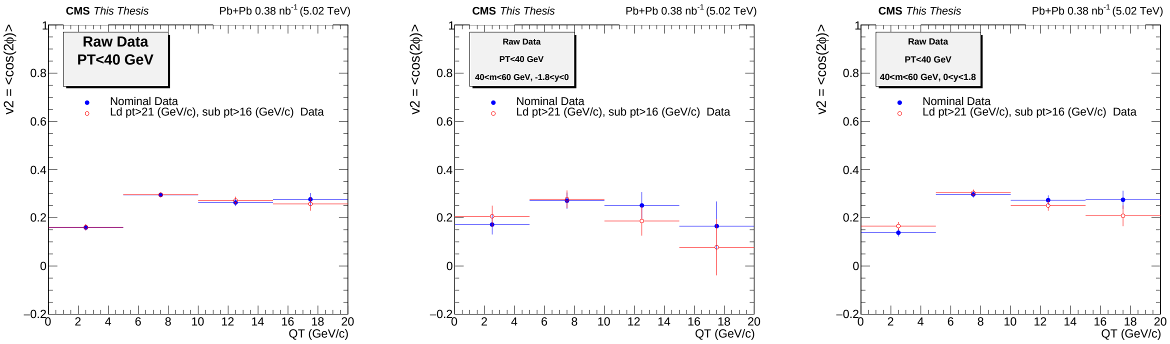

Figure 6.5: Raw data, differential analysis regions, jet p_t systematics on v_2. The nominal results (blue points) and the results after varying the jet p_t cut (red points) are compared.

6.4 Resolution correction factor systematics

We have added to the resolution correction factor as a systematic uncertainty a 50% variation of the MC closure, which is an approach used in other CMS jet analyses. Figure 6.6 shows the different in ϕ measured in terms of Q_T and P_T for the MC sample (RAPGAP + STARLIGHT, defined above, as a function of Q_T for Region I (left corner), Region II (middle plots) and Region III (right corner).

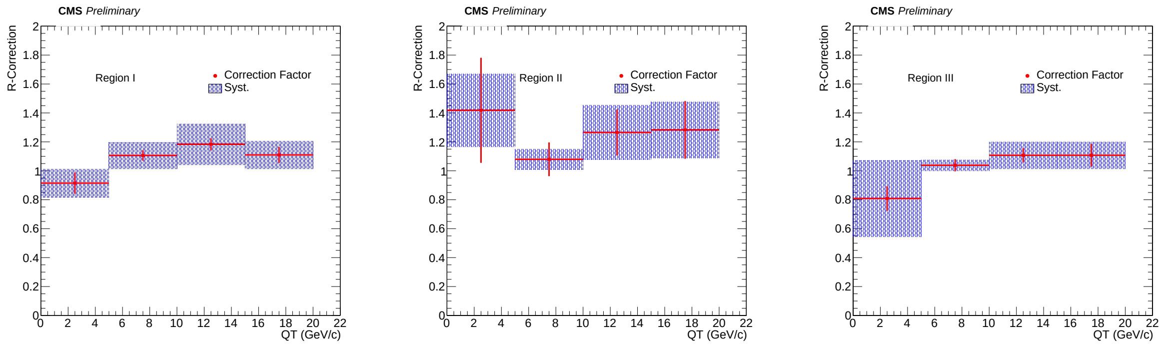

Figure 6.6: Resolution factor (R) including the systematic uncertainty for Regions I, II, and III (see text for details).

6.5 Total systematic uncertainty

The systematic uncertainties from the LRG, vertex, and jet p_t selection are added in quadrature to produce the total systematic uncertainty. Table 6.4 shows the total systematic uncertainties for the differential analysis regions. The systematic uncertainty on the R resolution factor are negligible compared to the sources presented.

QT Bin (in GeV/c)	Region I (%)	Region II (%)	Region III (%)
1-5	5.1	16.5	11.9
5-10	4.0	4.8	4.3
10-15	5.9	16.9	8.1
15-20	3.3	20.0	23.2

Table 6.4: Table of total v_2 systematic uncertainties.

Chapter 7

Results

The results presented in this thesis have been divided into two sections. We first present the results after applying the mixed-event subtraction, and then present the corresponding results without it.

Although in typical flow analyses in high-energy nucleus-nucleus collisions the event-mixed subtraction technique is applied, in this analysis it is questionable. First, the angular correlation studied here is not the laboratory frame as for the standard flow analyses, and all the theoretical predictions reported do not mention the need to subtract the mixed-event distribution.

When subtracting the data, as mentioned in this thesis, we have considered that the mixed-events are additive. And this is an assumption that has not been justified fully at present.

Presenting both results is important since the $v2$ results, in particular, the Q_T dependance has a different shape and magnitude whether the mixed-event v_2 is subtracted or not, particularly for the low p_T region which corresponds to most of the data analyzed.

7.1 Results using mixed event subtraction

Table 7.1, Table 7.2, and Table 7.3 show the v_2 values from the corrected data in the differential analysis regions as a function of Q_T for the differential analysis regions. The FRP selection is used as a systematic cross-check of the BRP selection. These regions encompass $Q_T < 20$ GeV and $P_T < 40$ GeV. The analysis regions are used to study the energy $W_{\gamma Pb}$ dependence of v_2. To this end, Region I covers the full rapidity range of the analysis; Region II covers the backward rapidity scattered jets; and Region III covers the forward rapidity scattered jets. These results are shown in Figure 7.1 for Region I, in Figure 7.2 for Region II, and in Figure 7.3 for Region III. The corrected

v_2 increases as Q_T increases from about 0.5 reaching about 1. The comparison between the Region II and Region III results is shown in Figure 7.4.

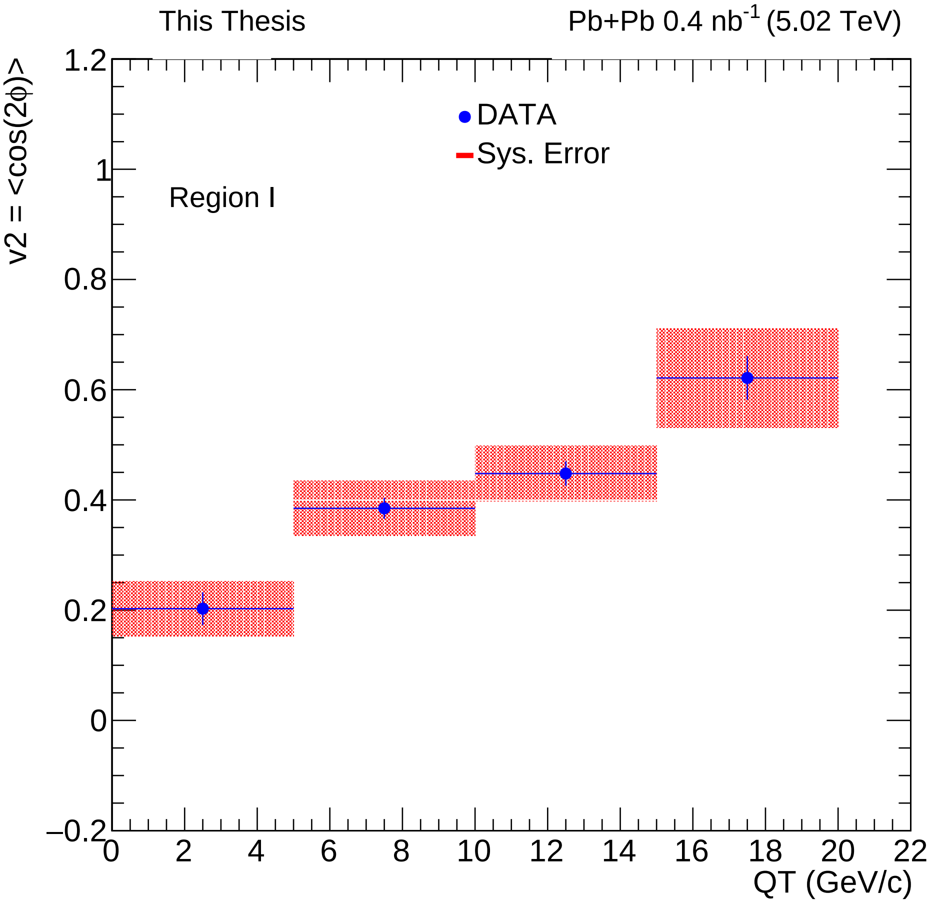

Figure 7.1: Corrected data, differential analysis region I, v_2 with systematic uncertainty, for BRP selection.

Figure 7.4 compares the corrected data v_2 measured in Region II and Region III for the BRP selection. In addition, the generated RAPGAP + STARLIGHT and been compared to the corrected v_2 results. Figure 7.5, Figure 7.6 and Figure 7.7 show this comparison for Region I, Region II and Region III, respectively. The overall trend of v_2 increasing as Q_T increases is seen in the generated RAPGAP + STARLIGHT sample, although the values are somewhat below the corrected data for most intervals.

Figure 7.8 shows the corrected v_2 distribution of Region I, with an additional requirement that $P_T > 30$ GeV. We have made this selection to study the impact of the mixed-event subtraction. At

Table 7.1: Region 1

Bin (GeV)	Mix Sub. V2	Mix Sub. V2 Stat.	Mix Sub. V2 Sys.	R-Corr.	R-Corr. Stat.	R-Corr. Sys.	Corr. V2	Total Uncert.
0<QT<5	0.19	0.02	0.03	0.92	0.07	0.10	0.20	0.05
5<QT<10	0.43	0.02	0.02	1.11	0.04	0.09	0.39	0.05
10<QT<15	0.53	0.02	0.04	1.18	0.04	0.14	0.45	0.05
15<QT<20	0.69	0.03	0.03	1.11	0.06	0.09	0.62	0.09

Table 7.2: Region 2

Bin (GeV)	Mix Sub. V2	Mix Sub. V2 Stat.	Mix Sub. V2 Sys.	R-Corr.	R-Corr. Stat.	R-Corr. Sys.	Corr. V2	Total Uncert.
0<QT<5	0.09	0.09	0.04	1.42	0.36	0.25	0.06	0.07
5<QT<10	0.33	0.06	0.02	1.08	0.12	0.07	0.31	0.14
10<QT<15	0.55	0.07	0.10	1.26	0.16	0.19	0.43	0.11
15<QT<20	0.64	0.11	0.19	1.28	0.20	0.20	0.50	0.19

Table 7.3: Region 3

Bin (GeV)	Mix Sub. V2	Mix Sub. V2 Stat.	Mix Sub. V2 Sys.	R-Corr.	R-Corr. Stat.	R-Corr. Sys.	Corr. V2	Total Uncert.
0<QT<5	0.16	0.03	0.05	0.81	0.09	0.26	0.20	0.08
5<QT<10	0.45	0.02	0.03	1.04	0.04	0.04	0.43	0.12
10<QT<15	0.54	0.02	0.05	1.11	0.05	0.09	0.49	0.06
15<QT<20	0.70	0.04	0.19	1.11	0.08	0.09	0.63	0.19

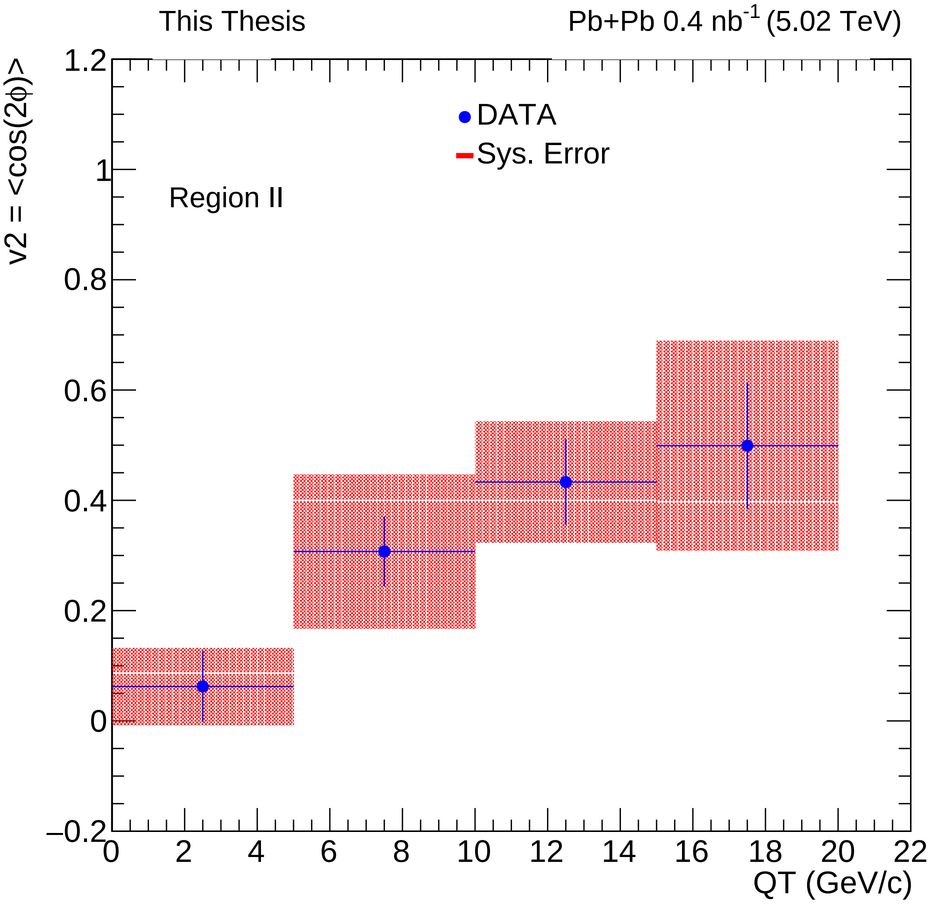

Figure 7.2: Corrected data, differential analysis region II, v_2 with systematic uncertainty, for BRP selection.

low P_T the impact of the subtraction is the largest, as discussed above, and by requiring $P_T > 30$ GeV we observe that the measured v_2 is still non-zero across the Q_T intervals studied.

7.2 Results without mixed-event subtraction

As mentioned in the introduction of this chapter, there are some caveats in justifying a mixed-event v_2 subtraction and in its implementation. For this reason, we have also measured v_2 without subtracting for the mixed-event distribution.

The corrected v_2, without mixed event subtraction, are presented in Figure 7.9, Figure 7.10, and Figure 7.11 as a function of Q_T for Region I, Region II, and Region III.

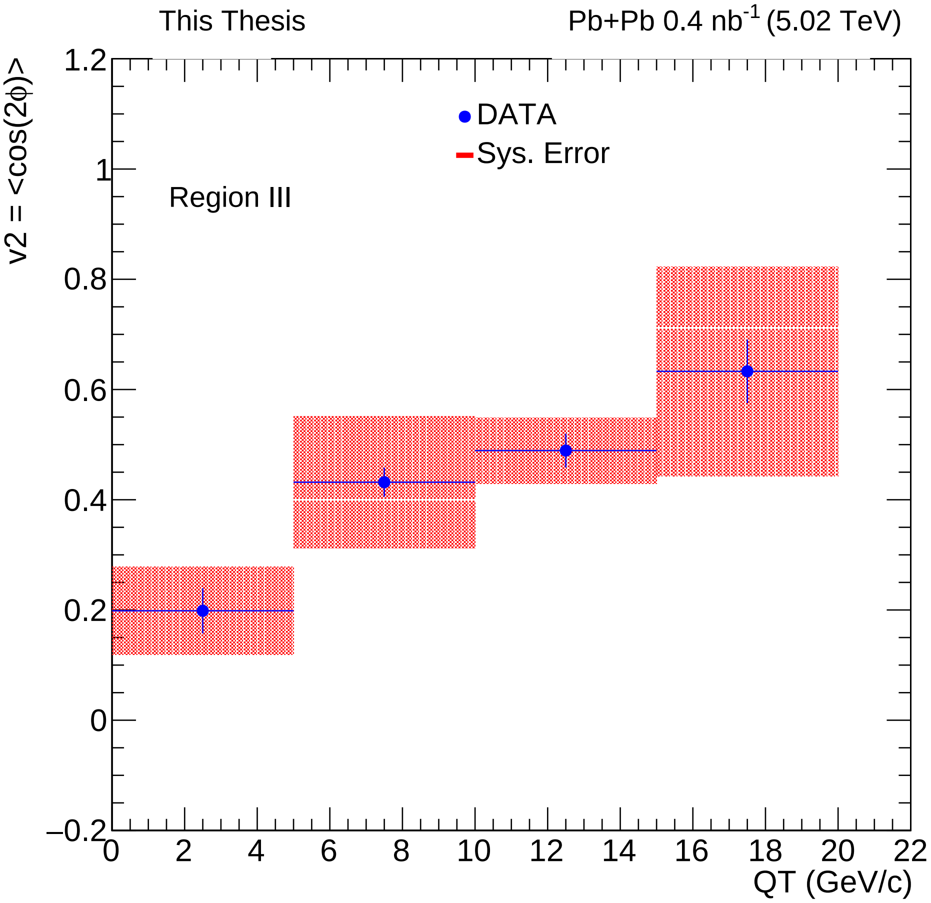

Figure 7.3: Corrected data, differential analysis region III, v_2 with systematic uncertainty, for BRP selection.

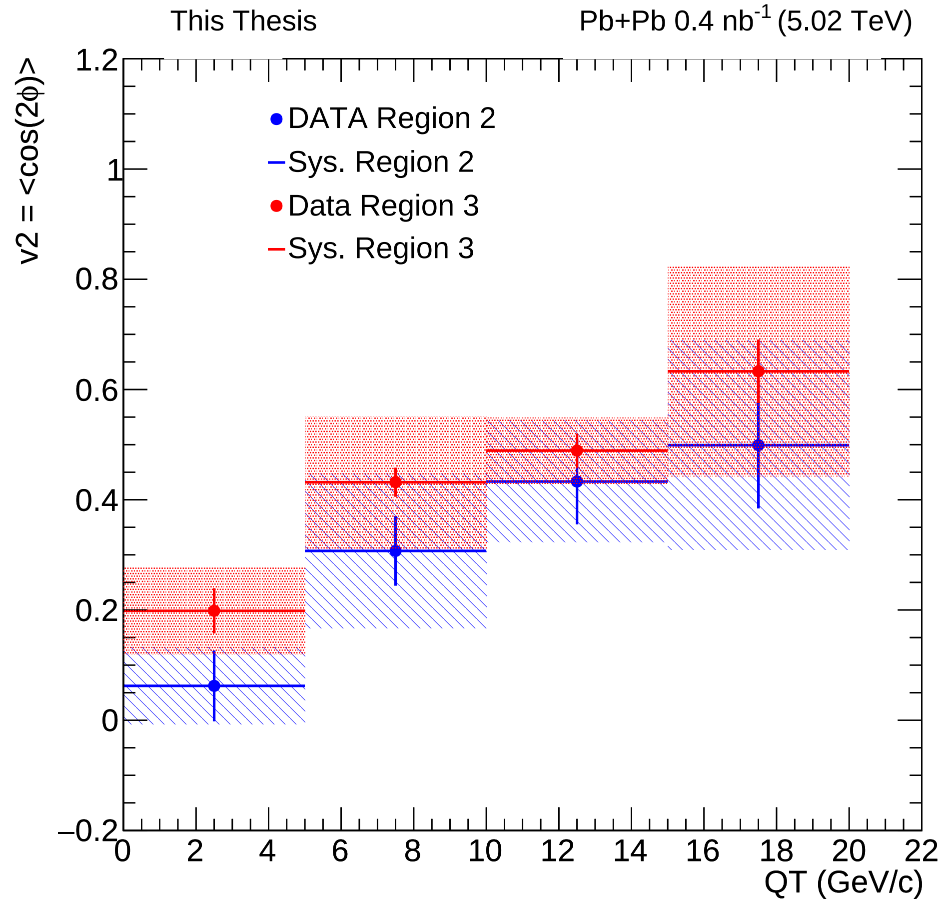

Figure 7.4: Corrected data, differential analysis region II (red) and region III (black), v_2 as a function of Q_T for the BRP selection.

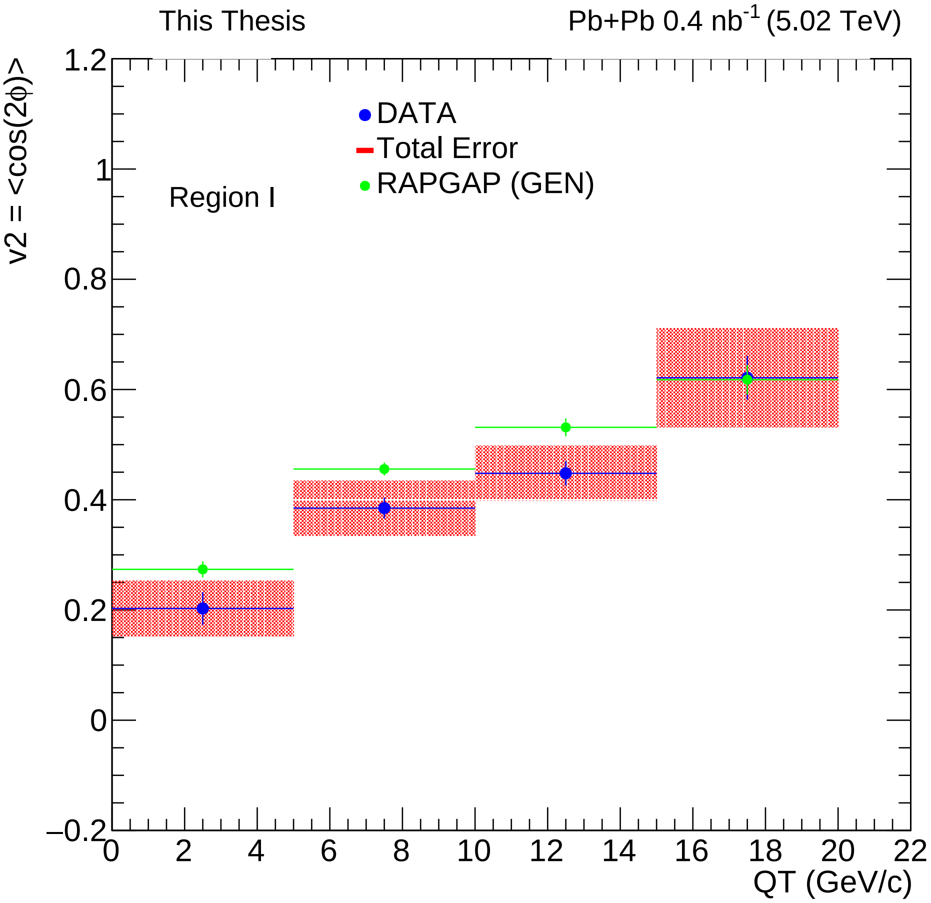

Figure 7.5: Corrected data, differential analysis region I, v_2 with systematic uncertainty, for BRP selection. The corresponding RAPGAP+STARLIGHT sample has been overlaid.

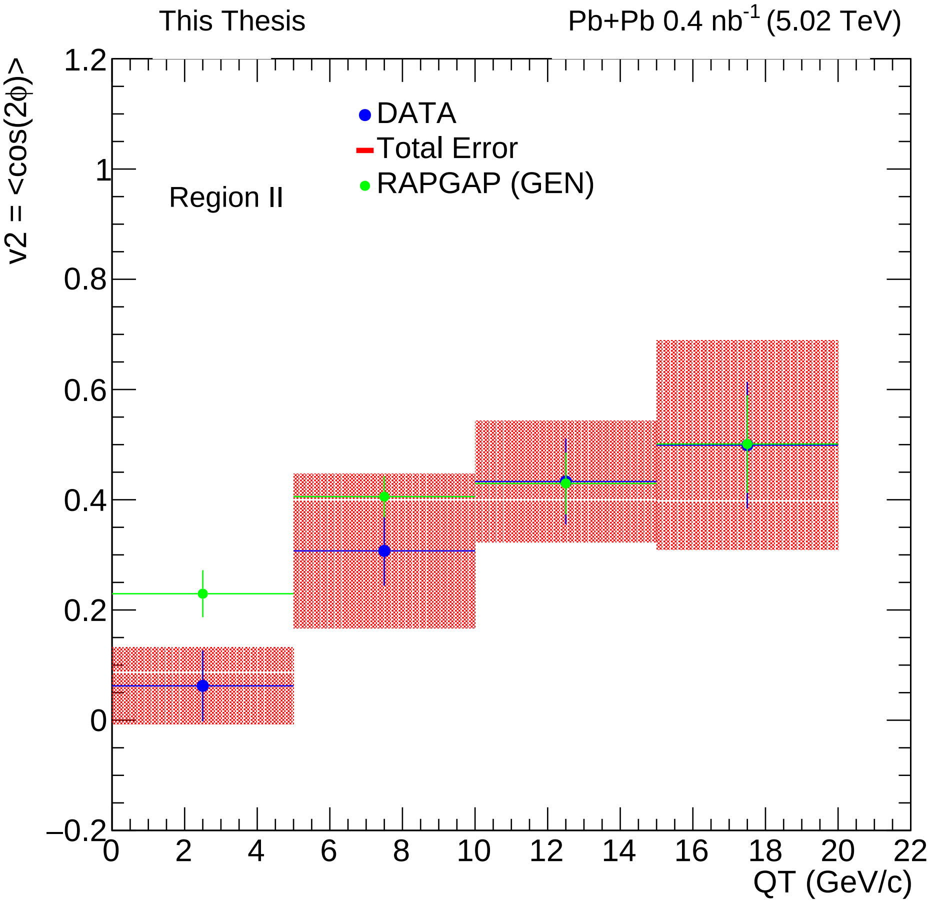

Figure 7.6: Corrected data, differential analysis region II, v_2 with systematic uncertainty, for BRP selection. The corresponding RAPGAP+STARLIGHT sample has been overlaid.

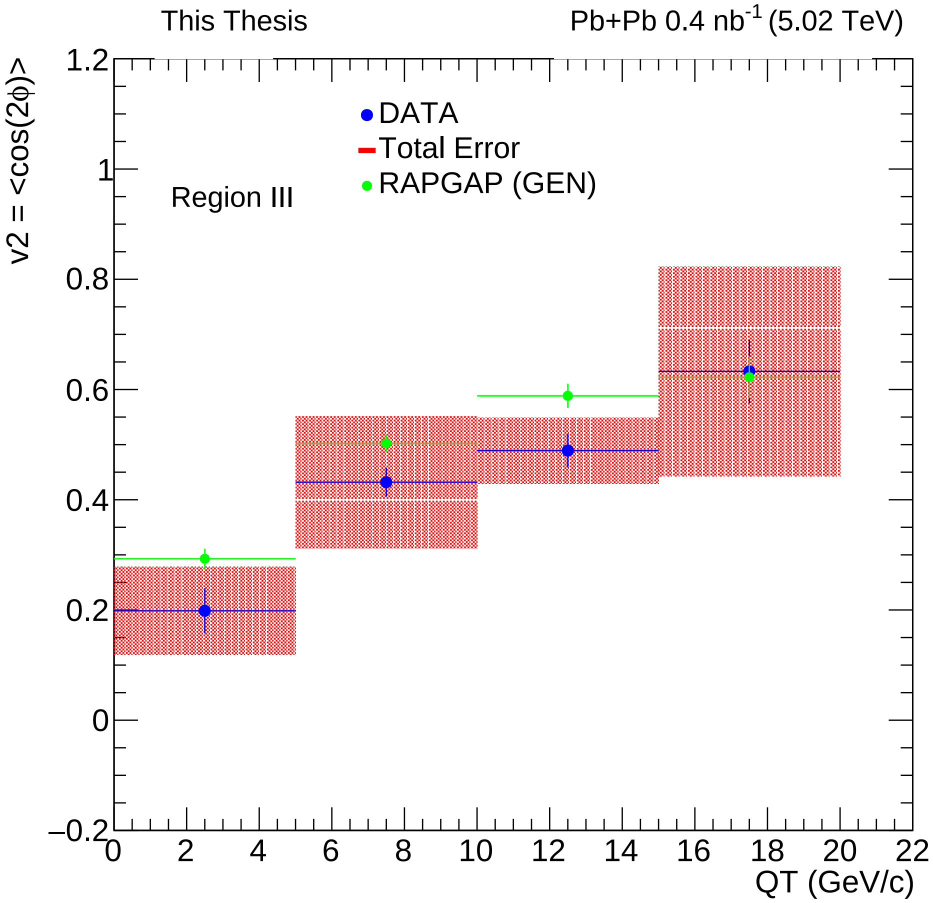

Figure 7.7: Corrected data, differential analysis region III, v_2 with systematic uncertainty, for BRP selection. The corresponding RAPGAP+STARLIGHT sample has been overlaid.

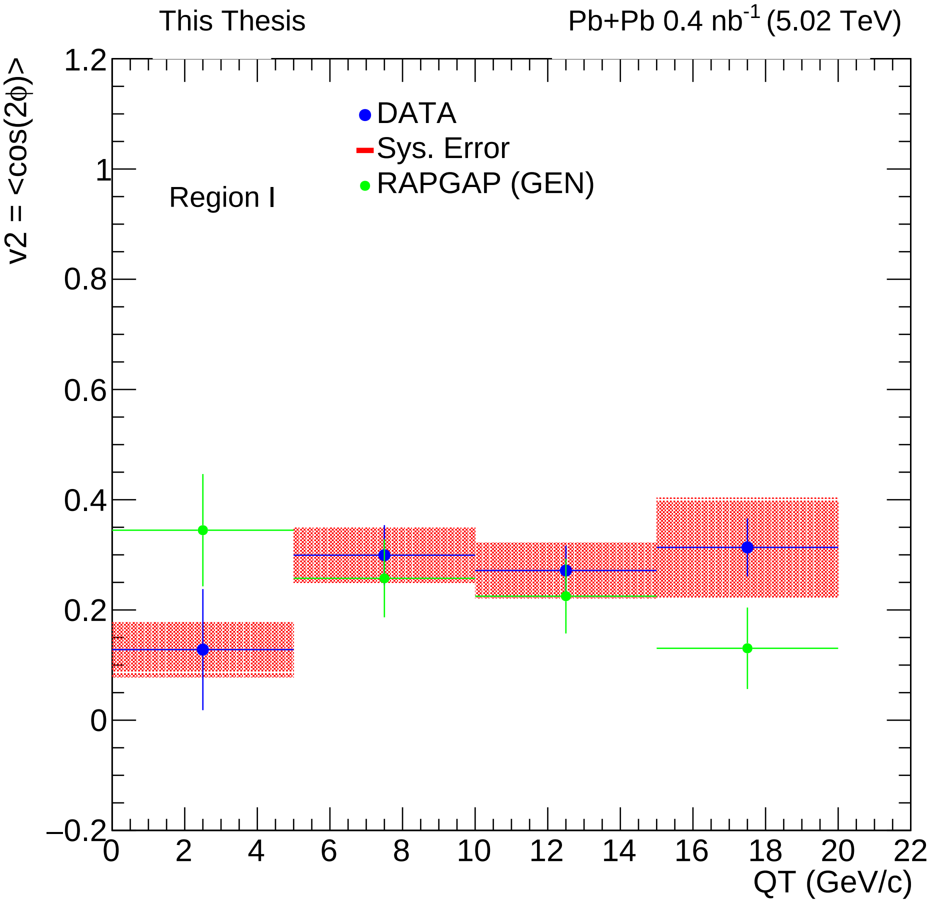

Figure 7.8: Corrected v_2 distribution, for Region I, with additional cut on $P_T > 30$ GeV.

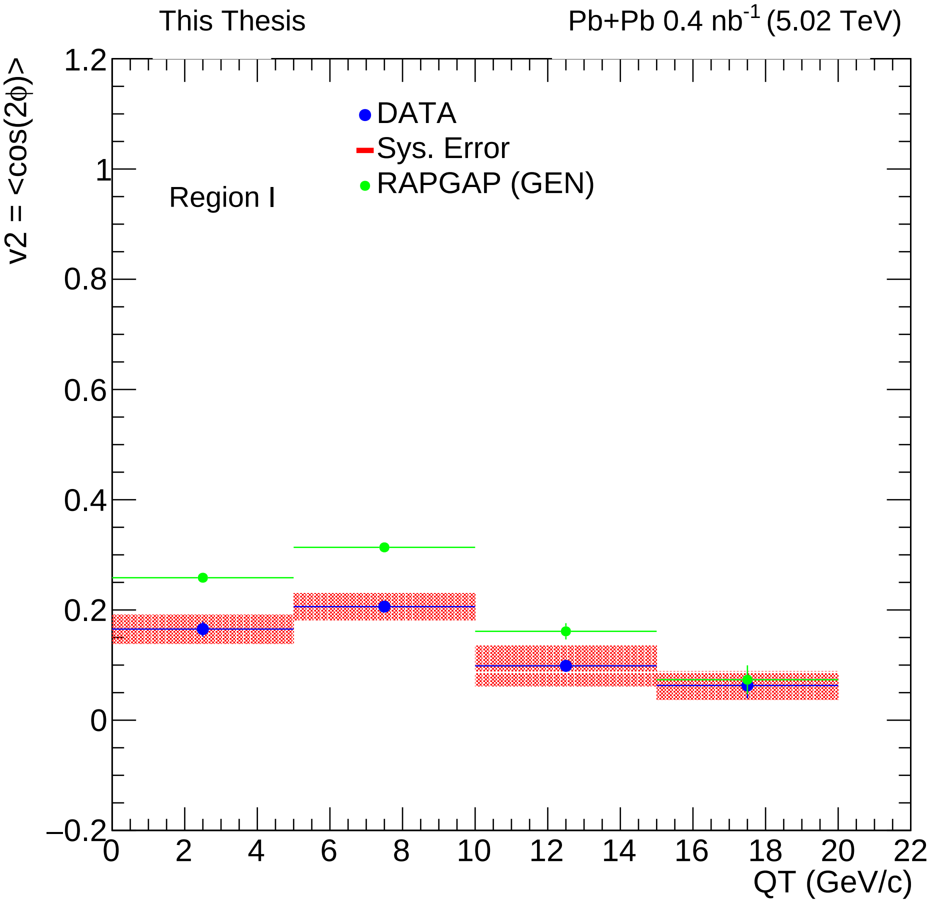

Figure 7.9: Corrected v_2 distributions, without mixed event subtraction, for Regions I.

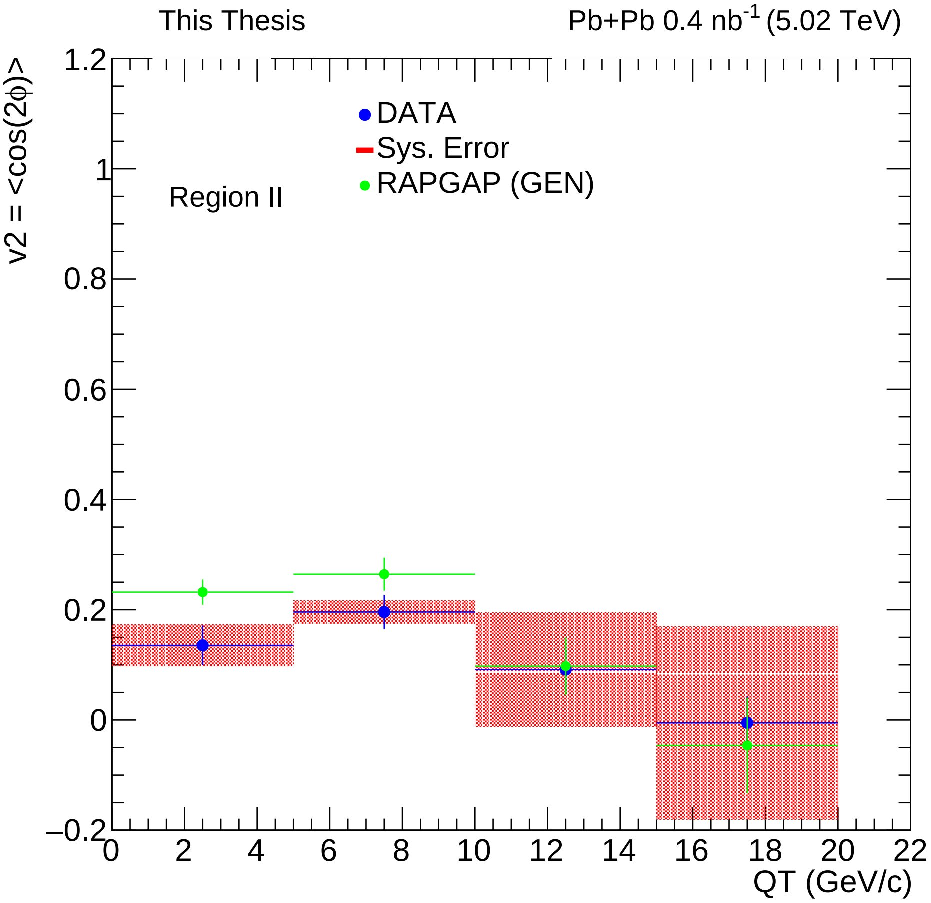

Figure 7.10: Corrected v_2 distributions, without mixed event subtraction, for Regions II.

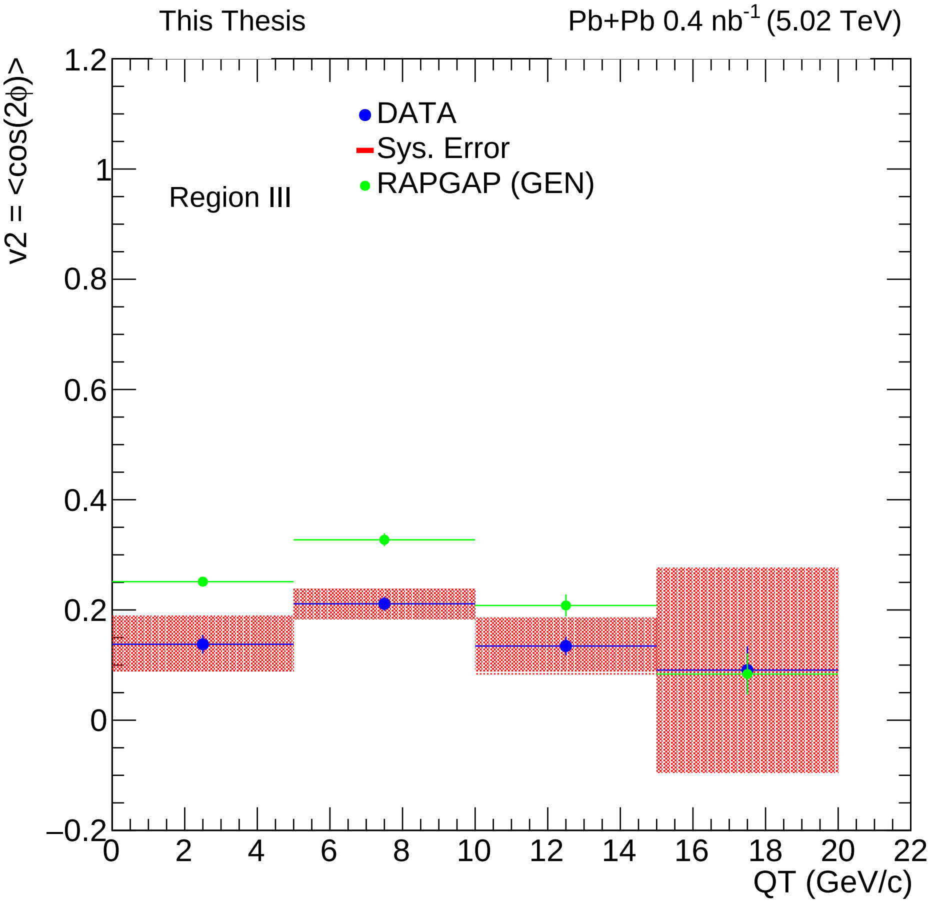

Figure 7.11: Corrected v_2 distributions, without mixed event subtraction, for Regions III.

Chapter 8

Summary

High-energy photon-nucleon (nucleus) collisions offer a unique opportunity to study hadron structure and low Bjorken-x gluon dynamics at photon intensities and energies that are unavailable elsewhere. The study of such reactions has received renewed interest following recent studies of ultra-peripheral collisions (UPCs) involving ions and protons at RHIC and the LHC. In UPCs, photon-induced interactions predominantly occur when the colliding hadrons are separated by a distance larger than the sum of their radii. For this subset of collisions hadronic interactions are highly suppressed. Because of Lorentz contraction, the electromagnetic field of a relativistic heavy-ion is equivalent to a flux of virtual photons. In UPCs, one of the hadrons may emit a quasi-real photon that fluctuates into a quark-antiquark pair with the photon quantum numbers. The interaction proceeds via the exchange of the vacuum quantum numbers, the so-called pomeron exchange. The momentum transferred at the proton vertex is quantified by the Mandelstam variable t. The Fourier transform of t gives access to the transverse profile of the target. In a similar way, the Fourier components of the angular distribution are expected to signal the orbital motion of the target.

The study of coherent dijet photoproduction in ultra-peripheral heavy-ion collisions has recently been suggested as a probe of the gluon Wigner distribution, which is considered the most fundamental gluon distribution. The dijet kinematics express the azimuthal anisotropy (v_2) of the gluon distribution in the nuclear target. Such “elliptic" gluons originate from the intrinsic orbital momentum of the target. Measuring v_2 from coherent dijets is expected to give access, for the first time, to the gluon Wigner distribution.

The analysis presented in this thesis focused on the study of angular correlations of dijets in ultra-peripheral PbPb collisions at $\sqrt{s_{NN}} = 5.02$ TeV. The dijets are produced by the interaction of a photon with the lead nuclear target, where the photon is emitted from one of the two colliding particles. We present, for the first time, the measurement of the second harmonic of the angular distribution, v_2, which is believed to originate from the orbital angular momentum of the gluonic matter within the lead target. At the same time, analysis presented in this thesis covers a wider Q_T region, and while P_T is always larger than Q_T, P_T is not as large as required by the theoretical calculations mentioned in the literature.

Indeed, some caveats are important before proceeding to the interpretation of the results presented in this thesis; for example, the justification of the subtraction of the mixed-event data, which is not discussed in the theoretical studies cited in this work. For this reason, we presented the measured v_2 with and without the mixed-event v_2 subtraction. In addition, the theorists are interested in studying the coherent photoproduction of dijets, while there are also some non-zero correlations for high Q_T dijets which are consistent to a hard-scattering process. Developing an analysis technique for utilizing these events in the low Q_T region is important as they could be a background-type process. Furthermore, the high Q_t dijets are from a hard-scattering process which can in principle be computed using perturbative QCD. No detailed calculations about this process exist in the literature at present. Refined studies of the jet energy scale correlation will lower the conservative estimate of systematic uncertainty presented here. The jet energy scale correction on the Q_T bins has not been applied, yet this is not expected to change the shape of the Q_T dependence of the results.

The data collected by CMS in this thesis, together with the forthcoming PbPb data in Fall 2018, will allow physicists to study a wide variety of processes involving jets, using jets coming from charm or bottom quarks. We have also prepared triggers and collected pPb data in 2016 to study dijet photoproduction, offering the opportunity to study the process in photon-proton interactions at higher energies.

The precise measurement of the elliptic gluon distribution relies on the extraction of longitudinal polarization. The method for doing so in hadronic colliders, such as the LHC, is not yet developed. Most of the theoretical predictions of the elliptic gluon distribution have been done for the future U.S.-based Electron-Ion Collider. Altogether, the results presented in this thesis are expected to provide new insights into the gluon dynamics in nuclei at high energies, and trigger discussion among the nuclear physics community interested in angular correlations of dijets both at LHC and EIC energies.

References

[1] J. Rafelski, “Connecting QGP-Heavy Ion Physics to the Early Universe,” 2013. [Nucl. Phys. Proc. Suppl.243-244,155(2013)].

[2] I. Arsene *et al.*, “Quark gluon plasma and color glass condensate at RHIC? The Perspective from the BRAHMS experiment,” *Nucl. Phys.*, vol. A757, pp. 1–27, 2005.

[3] “The Frontiers of Nuclear Science, A Long Range Plan,” 2008.

[4] Y. Hagiwara, Y. Hatta, and T. Ueda, “Wigner, Husimi, and generalized transverse momentum dependent distributions in the color glass condensate,” *Phys. Rev.*, vol. D94, no. 9, p. 094036, 2016.

[5] J. G. Contreras and J. D. Tapia Takaki, “Ultra-peripheral heavy-ion collisions at the LHC,” *Int. J. Mod. Phys.*, vol. A30, p. 1542012, 2015.

[6] C. von Weizsacker, “Radiation emitted in collisions of very fast electrons,” *Z.Phys.*, vol. 88, pp. 612–625, 1934.

[7] E. Williams, “Nature of the high-energy particles of penetrating radiation and status of ionization and radiation formulae,” *Phys.Rev.*, vol. 45, pp. 729–730, 1934.

[8] F. J. Dyson and A. Lenard, “Stability of matter. I,” vol. 8, pp. 423–434, Mar. 1967.

[9] K. Huang, *Statistical Mechanics*. John Wiley & Sons, 2 ed., 1987.

[10] F. Halzen and A. D. Martin, *Quarks and Leptons: An Introductory Course In Modern Particle Physics*. 1984.

[11] M. E. Peskin and D. V. Schroeder, *An Introduction to quantum field theory*. Reading, USA: Addison-Wesley, 1995.

[12] Y. Hatta, B.-W. Xiao, and F. Yuan, "Probing the Small- x Gluon Tomography in Correlated Hard Diffractive Dijet Production in Deep Inelastic Scattering," *Phys. Rev. Lett.*, vol. 116, no. 20, p. 202301, 2016.

[13] D. Griffiths, *Introduction to elementary particles*. 2008.

[14] R. Bouchendira, P. Clade, S. Guellati-Khelifa, F. Nez, and F. Biraben, "New determination of the fine structure constant and test of the quantum electrodynamics," *Phys. Rev. Lett.*, vol. 106, p. 080801, 2011.

[15] G. Abbiendi *et al.*, "Measurement of the running of the QED coupling in small-angle Bhabha scattering at LEP," *Eur. Phys. J.*, vol. C45, pp. 1–21, 2006.

[16] M. Gell-Mann, "A Schematic Model of Baryons and Mesons," *Phys. Lett.*, vol. 8, pp. 214–215, 1964.

[17] R. Brock *et al.*, "Handbook of perturbative QCD: Version 1.0," *Rev. Mod. Phys.*, vol. 67, pp. 157–248, 1995.

[18] F. Wilczek, "QCD made simple," *Phys. Today*, vol. 53N8, pp. 22–28, 2000.

[19] T. Schäfer, "Phases of QCD," in *20th Annual Hampton University Graduate Studies Program (HUGS 2005) Newport News, Virginia, May 31-June 17, 2005*, 2005.

[20] S. Bethke, "Experimental tests of asymptotic freedom," *Prog. Part. Nucl. Phys.*, vol. 58, pp. 351–386, 2007.

[21] A. Deur, S. J. Brodsky, and G. F. de Teramond, "The QCD Running Coupling," *Prog. Part. Nucl. Phys.*, vol. 90, pp. 1–74, 2016.

[22] J. D. Bjorken, “Asymptotic Sum Rules at Infinite Momentum,” *Phys. Rev.*, vol. 179, pp. 1547–1553, 1969.

[23] M. Thomson, *Modern particle physics*. New York: Cambridge University Press, 2013.

[24] D. d’Enterria, “Hard spectra and qcd matter: Experimental review,” *J. Phys.*, vol. G30, pp. S767–S774, 2004.

[25] J. Bjorken, “Highly Relativistic Nucleus-Nucleus Collisions: The Central Rapidity Region,” *Phys.Rev.*, vol. D27, pp. 140–151, 1983.

[26] S. Shimizu, “Low Q**2 Structure Functions including the Longitudinal Structure Function,” in *QCD and high energy interactions. Proceedings, 44th Rencontres de Moriond, La Thuile, Italy, March 14-21, 2009*, pp. 301–304, 2009.

[27] A. Martin, W. Stirling, R. Thorne, and G. Watt, “Parton distributions for the LHC,” *Eur.Phys.J.*, vol. C63, pp. 189–285, 2009.

[28] K. J. Eskola, H. Paukkunen, and C. A. Salgado, “An Improved global analysis of nuclear parton distribution functions including RHIC data,” *JHEP*, vol. 0807, p. 102, 2008.

[29] J. Pumplin, D. Stump, J. Huston, H. Lai, P. M. Nadolsky, *et al.*, “New generation of parton distributions with uncertainties from global QCD analysis,” *JHEP*, vol. 0207, p. 012, 2002.

[30] S. Chatrchyan *et al.*, “J/ψ and ψ(2s) production in pp collisions at $\sqrt{s} = 7$ tev,” *Journal of High Energy Physics*, vol. 2012, no. 2, 2012.

[31] P. Paakkinen, “Nuclear parton distribution functions,” in *Old and New Strong Interactions from LHC to Future Colliders (LFC17) Trento, Italy, September 11-15, 2017*, 2018.

[32] L. McLerran, “The Color Glass Condensate and Glasma,” 2008.

[33] A. Accardi, V. Guzey, A. Prokudin, and C. Weiss, “Nuclear physics with a medium-energy Electron-Ion Collider,” *Eur. Phys. J.*, vol. A48, p. 92, 2012.

[34] H. Satz, “The SPS heavy ion programme,” *Phys.Rept.*, vol. 403-404, pp. 33–50, 2004.

[35] P. Steinberg, “Relativistic heavy ion physics: Results from AGS to RHIC,” *eConf*, vol. C020620, p. FRBT03, 2002.

[36] H. Song, S. A. Bass, U. Heinz, T. Hirano, and C. Shen, “200 a gev $\mathrm{Au}+\mathrm{Au}$ collisions serve a nearly perfect quark-gluon liquid,” *Phys. Rev. Lett.*, vol. 106, p. 192301, May 2011.

[37] R. S. Bhalerao, “Relativistic heavy-ion collisions,” pp. 219–239. 21 p, Apr 2014. Comments: Updated version of the lectures given at the First Asia-Europe-Pacific School of High-Energy Physics, Fukuoka, Japan, 14-27 October 2012. Published as a CERN Yellow Report (CERN-2014-001) and KEK report (KEK-Proceedings-2013-8), K. Kawagoe and M. Mulders (eds.), 2014, p. 219. Total 21 pages.

[38] S. Hands, “The Phase diagram of QCD,” *Contemp.Phys.*, vol. 42, pp. 209–225, 2001.

[39] A. Bandyopadhyay, *Non-perturbative study of spectral function and its application in Quark Gluon Plasma*. PhD thesis, Saha Inst., 2017.

[40] E. Witten, “Cosmic Separation of Phases,” *Phys.Rev.*, vol. D30, pp. 272–285, 1984.

[41] M. Gyulassy and M. Plumer, “Jet Quenching in Dense Matter,” *Phys.Lett.*, vol. B243, pp. 432–438, 1990.

[42] T. Matsui and H. Satz, “J/ψ Suppression by Quark-Gluon Plasma Formation,” *Phys.Lett.*, vol. B178, p. 416, 1986.

[43] S. Margetis, K. Safarik, and O. Villalobos Baillie, “Strangeness production in heavy-ion collisions,” *Ann.Rev.Nucl.Part.Sci.*, vol. 50, pp. 299–342, 2000.

[44] B. Alver *et al.*, “Importance of correlations and fluctuations on the initial source eccentricity in high-energy nucleus-nucleus collisions,” *Phys. Rev. C*, vol. 77, p. 014906, Jan 2008.

[45] S. Chatrchyan *et al.*, “Multiplicity and transverse momentum dependence of two- and four-particle correlations in pPb and PbPb collisions,” *Phys.Lett.*, vol. B724, pp. 213–240, 2013.

[46] F. Karsch, E. Laermann, and A. Peikert, “Quark mass and flavor dependence of the QCD phase transition,” *Nucl.Phys.*, vol. B605, pp. 579–599, 2001.

[47] B. Abelev *et al.*, “Long-range angular correlations on the near and away side in *p*-Pb collisions at $\sqrt{s_{NN}} = 5.02$ TeV,” *Phys.Lett.*, vol. B719, pp. 29–41, 2013.

[48] J.-Y. Ollitrault, “Anisotropy as a signature of transverse collective flow,” *Phys.Rev.*, vol. D46, pp. 229–245, 1992.

[49] P. Sorensen, “Elliptic Flow: A Study of Space-Momentum Correlations In Relativistic Nuclear Collisions,” 2009.

[50] R. Bhalerao, N. Borghini, and J. Ollitrault, “Genuine collective flow from Lee-Yang zeroes,” *Phys.Lett.*, vol. B580, pp. 157–162, 2004.

[51] N. Borghini, P. M. Dinh, and J.-Y. Ollitrault, “Flow analysis from cumulants: A Practical guide,” 2001.

[52] K. Ackermann *et al.*, “Elliptic flow in Au + Au collisions at (S(NN))**(1/2) = 130 GeV,” *Phys.Rev.Lett.*, vol. 86, pp. 402–407, 2001.

[53] N. Borghini, R. Bhalerao, and J. Ollitrault, “Anisotropic flow from Lee-Yang zeroes: A Practical guide,” *J.Phys.*, vol. G30, pp. S1213–S1216, 2004.

[54] U. W. Heinz, “The Strongly coupled quark-gluon plasma created at RHIC,” *J. Phys.*, vol. A42, p. 214003, 2009.

[55] H. Wang, *Study of particle ratio fluctuations and charge balance functions at RHIC*. PhD thesis, Michigan State U., 2012.

[56] J. D. Bjorken, "Highly relativistic nucleus-nucleus collisions: The central rapidity region," *Phys. Rev. D*, vol. 27, pp. 140–151, Jan 1983.

[57] R. Vogt, "Quark-Gluon Plasma Signatures," 1998.

[58] G. Roland, K. Safarik, and P. Steinberg, "Heavy-ion collisions at the LHC," *Prog.Part.Nucl.Phys.*, vol. 77, pp. 70–127, 2014.

[59] L. Frankfurt, M. Strikman, and C. Weiss, "Small-x physics: From hera to lhc and beyond," *Ann. Rev. Nucl. Part. Sci.*, vol. 55, pp. 403–465, 2005.

[60] R. Vogt, "Heavy quark production in heavy ion colliders," *Heavy Ion Phys.*, vol. 18, pp. 11–20, 2003.

[61] A. Baltz, G. Baur, D. d'Enterria, L. Frankfurt, F. Gelis, *et al.*, "The Physics of Ultraperipheral Collisions at the LHC," *Phys.Rept.*, vol. 458, pp. 1–171, 2008.

[62] J. D. Jackson, *Classical electrodynamics*. New York, NY: Wiley, 3rd ed. ed., 1999.

[63] C. A. Bertulani, S. R. Klein, and J. Nystrand, "Physics of ultra-peripheral nuclear collisions," *Ann.Rev.Nucl.Part.Sci.*, vol. 55, pp. 271–310, 2005.

[64] J. Nystrand, "Electromagnetic interactions in nucleus nucleus and proton proton collisions," *Nucl. Phys.*, vol. A752, pp. 470–479, 2005.

[65] M. Wilde, "Measurement of direct photons in pp and pb–pb collisions with {ALICE}," *Nuclear Physics A*, vol. 904–905, no. 0, pp. 573c – 576c, 2013. The Quark Matter 2012 Proceedings of the {XXIII} International Conference on Ultrarelativistic Nucleus-Nucleus Collisions.

[66] V. Rebyakova, M. Strikman, and M. Zhalov, "Coherent rho and J/psi photoproduction in ultraperipheral processes with electromagnetic dissociation of heavy ions at RHIC and LHC," *Phys.Lett.*, vol. B710, pp. 647–653, 2012.

[67] S. Chekanov *et al.*, "Exclusive photoproduction of J / psi mesons at HERA," *Eur.Phys.J.*, vol. C24, pp. 345–360, 2002.

[68] M. Klasen, "Hard photoproduction at hera," 2007.

[69] H. Emling, "Electromagnetic excitation of the two phonon giant dipole resonance," *Prog.Part.Nucl.Phys.*, vol. 33, pp. 729–786, 1994.

[70] E. de Passos, M. Hussein, L. Canto, and B. Carlson, "The Mean energy, strength and width of triple giant dipole resonances," *Phys.Rev.*, vol. C65, p. 034326, 2002.

[71] M. Ryskin, "Diffractive J / psi electroproduction in LLA QCD," *Z.Phys.*, vol. C57, pp. 89–92, 1993.

[72] M. Goldhaber and E. Teller, "On nuclear dipole vibrations," *Phys.Rev.*, vol. 74, pp. 1046–1049, 1948.

[73] V. Goncalves and M. Machado, "Vector Meson Production in Coherent Hadronic Interactions: An update on predictions for RHIC and LHC," *Phys.Rev.*, vol. C84, p. 011902, 2011.

[74] C. Adler *et al.*, "Coherent ρ^0 production in ultra-peripheral heavy ion collisions," *Phys. Rev. Lett.*, vol. 89, p. 272302, 2002.

[75] V. Guzey and M. Zhalov, "Rapidity and momentum transfer distributions of coherent J/ψ photoproduction in ultraperipheral pPb collisions at the LHC," *JHEP*, vol. 1402, p. 046, 2014.

[76] L. Frankfurt, M. Strikman, and M. Zhalov, "Large t diffractive ρ-meson photoproduction with target dissociation in ultraperipheral p a and a a collisions at lhc," 2006.

[77] A. J. Baltz, S. R. Klein, and J. Nystrand, "Coherent vector meson photoproduction with nuclear breakup in relativistic heavy ion collisions," *Phys. Rev. Lett.*, vol. 89, p. 012301, 2002.

[78] S. R. Klein and J. Nystrand, "Photoproduction of quarkonium in proton proton and nucleus nucleus collisions," *Phys. Rev. Lett.*, vol. 92, p. 142003, 2004.

[79] S. R. Klein, J. Nystrand, J. Seger, Y. Gorbunov, and J. Butterworth, "STARlight: A Monte Carlo simulation program for ultra-peripheral collisions of relativistic ions," *Comput. Phys. Commun.*, vol. 212, pp. 258–268, 2017.

[80] B. Abelev *et al.*, "Coherent J/ψ photoproduction in ultra-peripheral Pb-Pb collisions at $\sqrt{s_{NN}} = 2.76$ TeV," *Phys.Lett.*, vol. B718, pp. 1273–1283, 2013.

[81] V. Khachatryan *et al.*, "Coherent J/ψ photoproduction in ultra-peripheral PbPb collisions at $\sqrt{s_{NN}} = 2.76$ TeV with the CMS experiment," *Phys. Lett.*, vol. B772, pp. 489–511, 2017.

[82] S. Klein and J. Nystrand, "Ultraperipheral nuclear collisions," *Phys. Today*, vol. 70, no. 10, pp. 40–47, 2017.

[83] A. Adeluyi and C. A. Bertulani, "Gluon distributions in nuclei probed at energies available at the CERN large hadron collider," *Phys. Rev. C*, vol. 84, p. 024916, Aug 2011.

[84] B. B. Abelev *et al.*, "Exclusive J/ψ photoproduction off protons in ultra-peripheral p-Pb collisions at $\sqrt{s_{NN}}$=5.02 TeV," 2014.

[85] S. J. Brodsky, L. Frankfurt, J. Gunion, A. H. Mueller, and M. Strikman, "Diffractive leptoproduction of vector mesons in QCD," *Phys.Rev.*, vol. D50, pp. 3134–3144, 1994.

[86] M. L. Miller, K. Reygers, S. J. Sanders, and P. Steinberg, "Glauber modeling in high energy nuclear collisions," *Ann.Rev.Nucl.Part.Sci.*, vol. 57, pp. 205–243, 2007.

[87] V. Guzey, E. Kryshen, M. Strikman, and M. Zhalov, "Evidence for nuclear gluon shadowing from the ALICE measurements of pbpb ultraperipheral exclusive production," *Physics Letters B*, vol. 726, no. 1–3, pp. 290 – 295, 2013.

[88] K. Eskola, H. Paukkunen, and C. Salgado, "EPS09: A New Generation of NLO and LO Nuclear Parton Distribution Functions," *JHEP*, vol. 0904, p. 065, 2009.

[89] L. Frankfurt, V. Guzey, and M. Strikman, “Leading Twist Nuclear Shadowing Phenomena in Hard Processes with Nuclei,” *Phys.Rept.*, vol. 512, pp. 255–393, 2012.

[90] A. Adeluyi and T. Nguyen, “Coherent photoproduction of ψ and Υ mesons in ultraperipheral pPb and PbPb collisions at the CERN Large Hadron Collider at $\sqrt{S_{NN}} = 5$ TeV and $\sqrt{S_{NN}} = 2.76$ TeV,” *Phys. Rev. C*, vol. 87, p. 027901, Feb 2013.

[91] A. Cisek, W. Schafer, and A. Szczurek, “Exclusive coherent production of heavy vector mesons in nucleus-nucleus collisions at LHC,” *Phys.Rev.*, vol. C86, p. 014905, 2012.

[92] S. R. Klein, “Ultra-peripheral collisions and hadronic structure,” *Nucl. Phys.*, vol. A967, pp. 249–256, 2017.

[93] V. Guzey, M. Strikman, and M. Zhalov, “Disentangling coherent and incoherent J/ψ photoproduction on nuclei by neutron tagging in ultraperipheral ion collisions at the LHC,” 2013.

[94] M. Strikman, M. Tverskoy, and M. Zhalov, “Neutron tagging of quasielastic J/psi photoproduction off nucleus in ultraperipheral heavy ion collisions at RHIC energies,” *Phys.Lett.*, vol. B626, pp. 72–79, 2005.

[95] V. Rebyakova, M. Strikman, and M. Zhalov, “Coherent ρ and J/Ψ photoproduction in ultraperipheral processes with electromagnetic dissociation of heavy ions at RHIC and LHC,” *Physics Letters B*, vol. 710, no. 4–5, pp. 647 – 653, 2012.

[96] I. A. Pshenichnov, J. P. Bondorf, I. N. Mishustin, A. Ventura, and S. Masetti, “Mutual heavy ion dissociation in peripheral collisions at ultrarelativistic energies,” *Phys. Rev. C*, vol. 64, p. 024903, Jul 2001.

[97] I. A. Pshenichnov, I. N. Mishustin, J. P. Bondorf, A. S. Botvina, and A. S. Iljinov, “Particle emission following coulomb excitation in ultrarelativistic heavy-ion collisions,” *Phys. Rev. C*, vol. 60, p. 044901, Sep 1999.

[98] P. Chomaz, “Collective excitations in nuclei,” 1997.

[99] M. Chiu, A. Denisov, E. Garcia, J. Katzy, A. Makeev, M. Murray, and S. White, “Measurement of mutual coulomb dissociation in $\sqrt{s_{\mathrm{NN}}} = 130\mathrm{GeV}$ $au + au$ collisions,” *Phys. Rev. Lett.*, vol. 89, p. 012302, Jun 2002.

[100] V. Andreev *et al.*, “Diffractive Dijet Production with a Leading Proton in *ep* Collisions at HERA,” *JHEP*, vol. 05, p. 056, 2015.

[101] L. Frankfurt, M. Strikman, and M. Zhalov, “Elastic and large t rapidity gap vector meson production in ultraperipheral proton-ion collisions,” *Phys.Lett.*, vol. B640, pp. 162–169, 2006.

[102] C. Alexa *et al.*, “Elastic and Proton-Dissociative Photoproduction of J/psi Mesons at HERA,” *Eur.Phys.J.*, vol. C73, p. 2466, 2013.

[103] A. Aktas *et al.*, “Diffractive photoproduction of ρ mesons with large momentum transfer at hera,” *Phys. Lett.*, vol. B638, pp. 422–431, 2006.

[104] F. D. Aaron *et al.*, “Measurement of the cross section for diffractive deep-inelastic scattering with a leading proton at HERA,” *Eur. Phys. J.*, vol. C71, p. 1578, 2011.

[105] F. D. Aaron *et al.*, “Diffractive Dijet Photoproduction in ep Collisions at HERA,” *Eur. Phys. J.*, vol. C70, pp. 15–37, 2010.

[106] A. V. Belitsky, X.-d. Ji, and F. Yuan, “Quark imaging in the proton via quantum phase space distributions,” *Phys. Rev.*, vol. D69, p. 074014, 2004.

[107] M. Diehl, “Generalized parton distributions,” *Phys. Rept.*, vol. 388, pp. 41–277, 2003.

[108] Y. Hatta, B.-W. Xiao, and F. Yuan, “Gluon Tomography from Deeply Virtual Compton Scattering at Small-x,” *Phys. Rev.*, vol. D95, no. 11, p. 114026, 2017.

[109] L. Evans and P. Bryant, “LHC Machine,” *JINST*, vol. 3, p. S08001, 2008.

[110] G. Aad *et al.*, “The ATLAS Experiment at the CERN Large Hadron Collider,” *JINST*, vol. 3, p. S08003, 2008.

[111] K. Aamodt *et al.*, “The ALICE experiment at the CERN LHC,” *JINST*, vol. 3, p. S08002, 2008.

[112] J. Alves, A. Augusto *et al.*, “The LHCb Detector at the LHC,” *JINST*, vol. 3, p. S08005, 2008.

[113] V. Andreev, X. Aslanoglou, A. Azman, M. Bakirci, S. Basegmez, *et al.*, “Performance studies of a full-length prototype for the CASTOR forward calorimeter at the CMS experiment,” *Eur.Phys.J.*, vol. C67, pp. 601–615, 2010.

[114] G. Bayatian *et al.*, “CMS technical design report, volume II: Physics performance,” *J.Phys.*, vol. G34, pp. 995–1579, 2007.

[115] D. G. d’Enterria *et al.*, “CMS physics technical design report: Addendum on high density QCD with heavy ions,” *J. Phys.*, vol. G34, pp. 2307–2455, 2007.

[116] L. R. F. Castillo, “The ATLAS and CMS detectors,” in *The Search and Discovery of the Higgs Boson*, 2053-2571, pp. 4–1 to 4–8, Morgan and Claypool Publishers, 2015.

[117] *The CMS tracker: addendum to the Technical Design Report*. Technical Design Report CMS, Geneva: CERN, 2000.

[118] S. Chatrchyan *et al.*, “Alignment of the CMS Silicon Tracker during Commissioning with Cosmic Rays,” *JINST*, vol. 5, p. T03009, 2010.

[119] A. Benaglia, “The CMS ECAL performance with examples,” *JINST*, vol. 9, p. C02008, 2014.

[120] S. Baffioni, C. Charlot, *et al.*, “Electron reconstruction in cms,” *CMS NOTE 2006/40*, 2006.

[121] G. L. Bayatian *et al.*, “CMS Physics,” 2006.

[122] G. Baiatian *et al.*, "Design, Performance, and Calibration of CMS Hadron-Barrel Calorimeter Wedges," 2007.

[123] M. M. I. Bloch, E. J. A., E. D. Barge, C. Campagnari, P. Kalavase, V. Krutelyov, D. Kovalskyi, J. Ribnik, and N. Amapane, "Muon identification in cms," *CMS Note*, vol. 2008/098, 2008.

[124] T. C. collaboration, "Performance of cms muon reconstruction in pp collision events at *sqrts* = 7 tev," *Journal of Instrumentation*, vol. 7, no. 10, p. P10002, 2012.

[125] C. Albajar, J. de Troconiz, J. Rohlf, and G. Wrochna, "Conceptual design of an improved CMS RPC muon trigger using the hadron outer scintillators," *Nucl.Instrum.Meth.*, vol. A545, pp. 97–113, 2005.

[126] O. A. Grachov *et al.*, "Status of zero degree calorimeter for CMS experiment," *AIP Conf.Proc.*, vol. 867, pp. 258–265, 2006.

[127] A. J. Baltz, C. Chasman, and S. N. White, "Correlated forward–backward dissociation and neutron spectra as a luminosity monitor in heavy-ion colliders," *Nuclear Instruments and Methods in Physics Research Section A: Accelerators, Spectrometers, Detectors and Associated Equipment*, vol. 417, no. 1, pp. 1 – 8, 1998.

[128] S. Dasu *et al.*, "CMS. The TriDAS project. Technical design report, vol. 1: The trigger systems," 2000.

[129] P. Sphicas, "CMS: The TriDAS project. Technical design report, Vol. 2: Data acquisition and high-level trigger," 2002.

[130] V. Khachatryan *et al.*, "The CMS trigger system," *JINST*, vol. 12, no. 01, p. P01020, 2017.

[131] F. Beaudette, "The CMS Particle Flow Algorithm," in *Proceedings, International Conference on Calorimetry for the High Energy Frontier (CHEF 2013): Paris, France, April 22-25, 2013*, pp. 295–304, 2013.

[132] A. M. Sirunyan *et al.*, "Particle-flow reconstruction and global event description with the CMS detector," *JINST*, vol. 12, no. 10, p. P10003, 2017.

[133] S. D. Ellis and D. E. Soper, "Successive combination jet algorithm for hadron collisions," *Phys. Rev.*, vol. D48, pp. 3160–3166, 1993.

[134] S. Agostinelli *et al.*, "GEANT4: A Simulation toolkit," *Nucl. Instrum. Meth.*, vol. A506, pp. 250–303, 2003.

[135] H. Jung, "Hard diffractive scattering in high-energy e p collisions and the Monte Carlo generator RAPGAP," *Comput. Phys. Commun.*, vol. 86, pp. 147–161, 1995.

[136] S. R. Klein, J. Nystrand, J. Seger, Y. Gorbunov, and J. Butterworth, "STARlight: A Monte Carlo simulation program for ultra-peripheral collisions of relativistic ions," *Comput. Phys. Commun.*, vol. 212, pp. 258–268, 2017.

[137] T. Sjostrand, S. Mrenna, and P. Z. Skands, "PYTHIA 6.4 Physics and Manual," *JHEP*, vol. 05, p. 026, 2006.

[138] D. Bourilkov, R. C. Group, and M. R. Whalley, "LHAPDF: PDF use from the Tevatron to the LHC," in *TeV4LHC Workshop - 4th meeting Batavia, Illinois, October 20-22, 2005*, 2006.

[139] C. Collaboration, "CMS Luminosity Based on Pixel Cluster Counting - Summer 2013 Update," 2013.

[140] S. Chatrchyan *et al.*, "Measurement of CMS Luminosity," 2010.

[141] M. W. Krasny, J. Chwastowski, and K. Slowikowski, "Luminosity measurement method for lhc: The theoretical precision and the experimental challenges," 2006.

[142] A. Kornmayer, "The CMS pixel luminosity telescope," *Nucl. Instrum. Meth.*, vol. A824, pp. 304–306, 2016.

[143] M. Guthoff, “Instrumentation for beam radiation and luminosity measurement in the CMS experiment using novel detector technologies,” *Nucl. Instrum. Meth.*, vol. A845, pp. 565–569, 2017.

[144] S. van der Meer, “Calibration of the Effective Beam Height in the ISR,” 1968.

Appendix A

Monte Carlo Generation and Reconstruction

The Monte Carlo (MC) for this analysis was generated using the RAPGAP software package. RAPGAP is a generator for electron-proton collisions. The structure functions measured at HERA are used to model a variety of diffractive processes. Each event has a characteristic energy for the virtual photon exchanged by the electron and proton. This photon energy is used to reweigh the MC to model the energy distribution of the Weizacker Williams photon flux.

$$w(E) = \frac{\mathrm{d}N_\gamma^{eff}}{\mathrm{d}E} / \frac{\mathrm{d}N_\gamma^{RAPGAP}}{\mathrm{d}E} \tag{A.1}$$

$\mathrm{d}N_\gamma^{RAPGAP}/\mathrm{d}E$ is obtained by fitting the formula for the total electron-proton cross-section, $\sigma_{\gamma p}$ to the RAPGAP MC's energy distribution.

$$\frac{\mathrm{d}^2\sigma_{ep}}{\mathrm{d}y\,\mathrm{d}Q^2} = \frac{\alpha}{2\pi Q^2}\left(\frac{1+(1-y)^2)}{y} - \frac{2(1-y)}{y}\cdot\frac{Q^2_{min}}{Q^2}\right)\cdot\sigma^{tot}_{\gamma^* p}(W_{\gamma^* p}), \tag{A.2}$$

where

$$Q^2_{min} \approx \frac{m_e^2\,y^2}{1-y}. \tag{A.3}$$

In this context, y is the energy fraction carried away from the electron by the mediating virtual photon, Q^2 is the photon virtuality, m_e is the electron mass, $\sigma^{tot}_{\gamma^* p}(W_{\gamma^* p})$ is the total photon-proton cross section, and $W_{\gamma^* p}$ is the center of mass energy of the photon-proton collision. The Feynman diagram of the RAPGAP process – boson-gluon fusion – is given in figure A.1. The photon energy-fraction, according to RAPGAP and STARLIGHT, is shown in figure A.2.

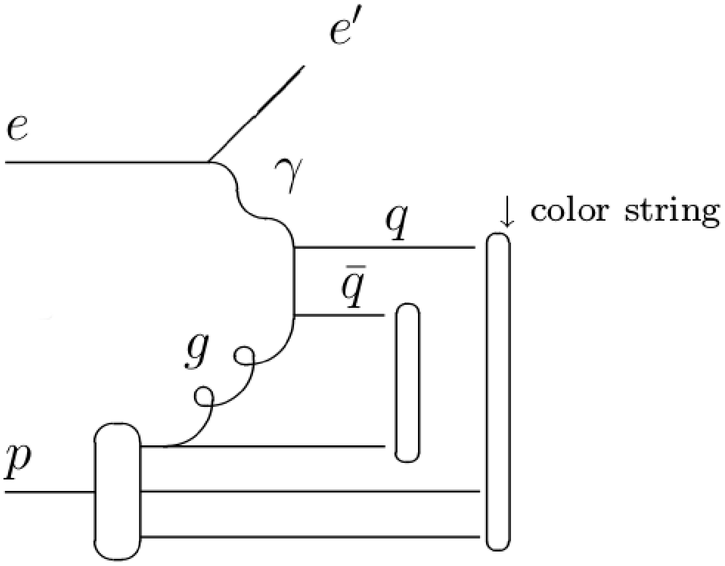

Figure A.1: RAPGAP process: boson-gluon fusion.

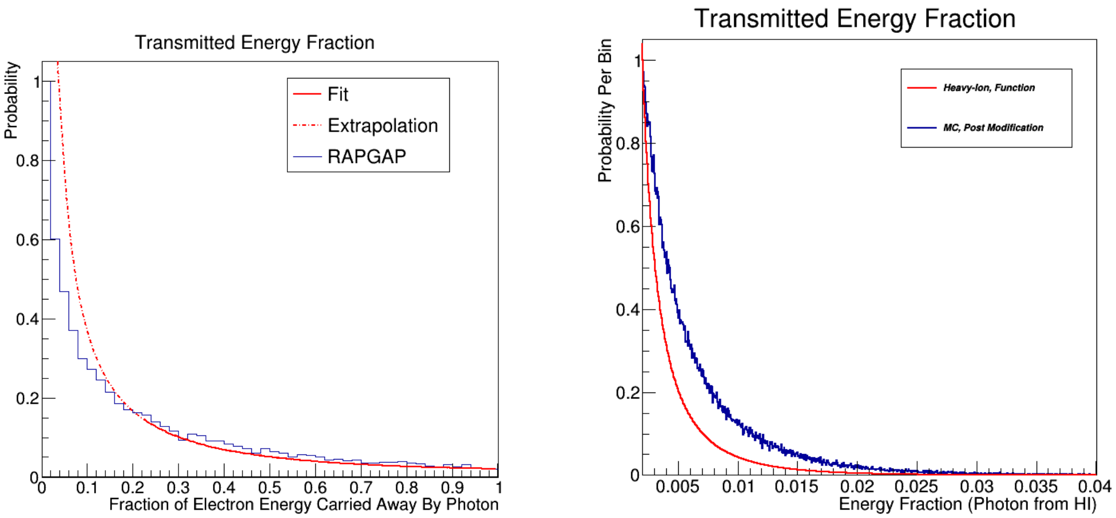

Figure A.2: Left: photon energy-fraction distribution before fitting, with RAPGAP(blue), fitting function (red solid), and the extrapolation of the fitting function (red dotted). Right: photon energy-fraction of RAPGAP after reweighing (blue) and according to STARLIGHT (red).

Appendix B

Measuring luminosity

Although the analysis results presented in this thesis do not require a precise knowledge of the measured luminosity since it is an angular correlation study, it is important to introduce this quantify since the author contributed in this direction and it is essential information needed during data-taking.

B.1 Instantaneous luminosity

One of the most important quantities measured by CMS is luminosity, which quantifies how many collisions are occurring in the detector. Luminosity is necessary to convert the number of events detected, for a given channel into a collision cross section. Collision cross sections are among the primary observables predicted by theoretical physicists. For particle physics, the collision cross-section of a process is typically measured through the relation:

$$\sigma = \frac{R}{L}, \tag{B.1}$$

where σ is the cross section, R is the rate at which the process occurs per collision, and L is the instantaneous luminosity. L is measured via the rate of a given luminometer and taking into account the acceptance A

$$L = \frac{R}{\sigma_o(E)A(t,\mu,n_b,...)}. \tag{B.2}$$

The denominator is typically measured as the visible cross section, σ_{vis},

$$\sigma_{vis} = \sigma_o(E)A(t,\mu,n_b,...), \tag{B.3}$$

where $\sigma_o(E)$ comes from separating out the dependence of σ_{vis} on collision energy E. σ_{vis} ideally has no dependence on time or experimental conditions i.e., it is constant with respect to pile-up and invariant to the filling scheme. For example, activity in the HF scales with the instantaneous luminosity. Therefore, the visible cross-section – which has no time dependence – can be used as a calibration constant for converting the rate of HF activity into instantaneous luminosity. Every luminometer should have its own characteristic visible cross section. In this way, multiple independent luminometers can cross check each other. $A(t,\mu,n_b,...)$ is the detector acceptance as a function of time (t), pileup (μ), and filling scheme n_b [139–141].

B.2 Luminometers

Within CMS, the Beam Radiation and Luminosity (BRIL) group is responsible for providing luminosity measurements and studying the radiation levels for the various detectors. There are two kinds of CMS luminometer: online and offline. Online luminometers readout the luminosity per bunch in real time. As of 2015 there are three online luminometers: the pixel luminosity telescope (PLT), the HF, and the beam conditions monitor (BCM1f). There is a high-rate, independent data-acquisition system for each of the online luminometers. Offline luminometers measure the rate of reconstructed objects. The primary offline lumimoneter is the pixel tracker. In general, the offline luminometers have better stability over time. [140]

The online and offline luminometers complement each other for high precision data analysis. Specifically, the offline data can be used to calibrate out imperfections in the online data.

In addition to these hardware luminometers, CMS can use physics processes as luminosity benchmarks. For example, measuring the Z-boson cross-section to a high accuracy and high precision is an alternative.

B.2.1 Pixel luminosity telescope

The pixel luminosity telescope (PLT) is one of the online luminometers of CMS. The PLT consists of 8 pixel telescopes arranged around the beamline on either side of the CMS interaction point. Each telescope has three layers of silicon pixel detector. Triple coincidences in these telescopes

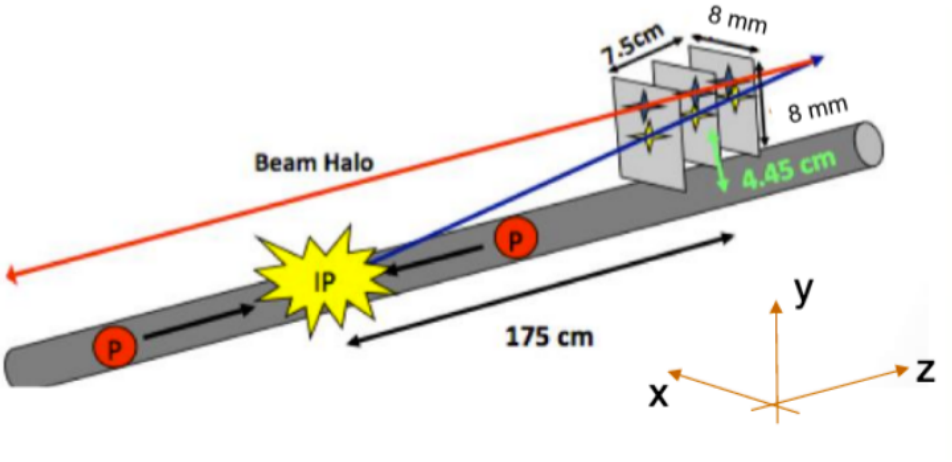

Figure B.1: PLT triple coincidence.

are measured as luminosity on a bunch-by-bunch basis. A cartoon of a triple coincidence track in the PLT is given in figure B.1. As an independent luminometer, the PLT data are also useful for reducing the systematic uncertainty of the luminosity delivered to CMS.

The PLT detector was installed as part of the CMS Run-2 upgrades. The hardware of the pixel sensors and the readout chip are similar to those used by the pixel tracker. However, the readout chips (ROC) of the PLT are capable of delivering fast-OR formatted data; the pixel tracker cannot do this. The fast-OR readout is optimized for delivering triple-coincidence data; whereas the standard pixel data readout has a maximum frequency of 100 kHz, the PLT fast-OR readout maxes out at an orders-of-magnitude greater frequency, of 40 Mhz [142].

B.2.2 Hadronic forward calorimeter

As mentioned before in section 3.2.3.1, the hadronic forward calorimeter (HF) of CMS is capable of measuring luminosity. Because of the high flux of particles through the forward region, the HF-luminosity is less subject to statistical uncertainty than the PCC-luminosity. The HF can measure luminosity per bunch through its own dedicated high-rate acquisition system (HTR) that is separate from the CMS DAQ. Within the HF, the HTR boards each have an additional HF luminosity transmission circuit (HLX). The HLX are mounted in one of the mezzanine expansion slots of the HTR.

The HF luminosity is subject to two difficulties. Because the PMTs require a calibrated voltage, the accumulation of gain changes over long periods of time will cause calibration drifts. Furthermore, the HF detector response has been shown to be nonlinear with respect to vertex pile-up. Substantial data analysis goes into calculating the corrections to these two sources of error [139].

B.2.3 Fast Beam Conditions Monitor

The CMS Beam Conditions and Radiation Monitoring System (BRM) provides a wide variety of information on the accumulated radiation dosage into CMS. This information is essential for protecting CMS from radiation damage. There are many subcomponents to the BRM system, one of which is the Fast Beam Conditions Monitor (BCM1F). The BCM1F is capable of measuring the beam-halo background and the flux from collision products. Similar to the PLT, BCM1F is located close to the beam pipe; however, BCM1F uses diamonds instead of silicon pixels. The readout from BCM1F is not digital, but an analog signal sent through optical fibers.

There are 24 single crystal diamond sensors in the BCM1F system. The BCM1F is located very close to interaction point, specifically 1.8 m on either side. This location is chosen specifically to take advantage of the 25 ns between bunch crossings. From the BCM1F vantage point there is a 12.5 ns delay between particle fluxes from the machine-induced-background and those coming from actual collisions. Thus the BCM1F can use timing to distinguish between signal and background [143].

B.2.4 Pixel cluster counting

One of the primary methods of measuring instantaneous luminosity is through pixel cluster counting (PCC) in the pixel-tracker. The collision rate is linked to instantaneous luminosity L via the total inelastic cross-section σ_T

$$\nu\mu = L\sigma_T, \tag{B.4}$$

where $v = 11246$ Hz is the beam revolution frequency and μ is the number of collisions per bunch crossing. We define the average number of pixel clusters per event, $\langle n \rangle$, as

$$\langle n \rangle = \mu n_1, \tag{B.5}$$

and the visible cross section σ_{vis} as

$$\sigma_{vis} = \sigma_T n_1, \tag{B.6}$$

where n_1 is the average number of pixel clusters per inelastic collision. Leveraging the previous two equations, the instantaneous luminosity reduces to

$$L = \frac{v \langle n \rangle}{\sigma_{vis}}, \tag{B.7}$$

such that L can be calculated after measuring the actual $\langle n \rangle$ of the data [139].

B.3 van de Meer scanning calibration

The luminometers of CMS produce signals proportional to the instantaneous luminosity of the LHC beam. However, these signals need to be properly calibrated with respect to a known visible cross-section for each luminometer. This calibration is accomplished via van de Meer (vdM) scanning [144]. The opposing beams of LHC are moved back and forth in the transverse plane, in particular, the separate X and Y planes of the CMS coordinate system. During the scan, the detector response is measured as a function of beam displacement. The beam widths are calculated from Gaussian fits to the detector response. The visible cross-section of the luminometer in question is then derived from the width of the beams, and acts as the calibration of the detector response. Figure B.2 presents the fitting of the vdM scan in the X and Y planes [139]. The visible cross section, in terms of vdM scan variables, is

$$\sigma_{vis} = \frac{2\pi \Sigma_x \Sigma_y v \langle n \rangle_{\Delta=0}}{N_1 N_2}, \tag{B.8}$$

where $\Sigma_x \Sigma_y$ is the beam overlap, v is the revolution frequency, $\langle n \rangle_{\Delta=0}$ is the amplitude of the vdM rate profile, and $N_1 N_2$ is the product of the number of protons (or heavy-ions) in the beams.

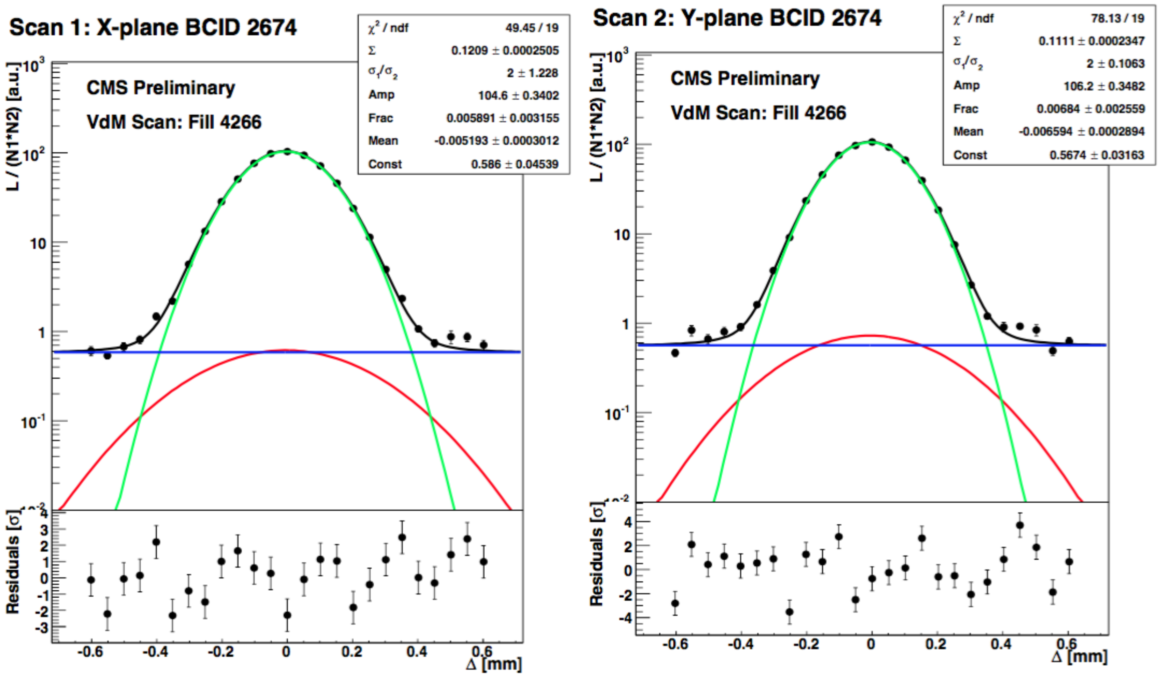

Figure B.2: vdM scan curves recorded by PCC for bunch crossing 2674; for the x-axis scan (left) and the y-axis scan (right). A double-Gaussian plus constant function (lines) is fit to data (black) [139].

B.4 Corrections to vdM scans

Several corrections must be applied to vdM scan data before calculating the visible cross section. These corrections are considered uncorrelated, i.e., it does not matter in what order they are applied. The results of the vdM scan must be corrected for the following phenomena: the length scale, the ghosts and satellite background, the growth in beam emittance, orbit drift, and beam-beam electromagnetic effects. These affect the normalization of the vdM scans, and so the corrections take the form of calibration constants derived from additional scans and beam monitoring subdetectors [139].

The length scale correction is derived by comparing the effects of a length scan to the response of the tracker; checking the difference between the reported beam displacement and that seen in the tracker. In addition to the circulating bunches, the LHC beams can be polluted by foreign particles that were not intended for injection by LHC commissioning. The presence of these foreign particles – fleeting "ghosts" and persistent "satellites" – can be detected by comparing the total beam current, measured by the DC beam current transformer, against the per bunch current measured by the Fast Beam Current Transformers (FBCT). The FBCT, because it is timed for bunch crossings, is less likely to interact with ghosts and satellites. Variations in beam emittance affect the vdM scans by changing the amplitude and width of the rate profile. The orbit drift correction is based on data from the Beam Position Monitors (BPM), which measure the position of the beam orbit in the LHC. Lastly, beam-beam effects refer to the electromagnetic forces that the beams exert on each other; for example, when the beams are transversely separated there is a small, but statistically significant, induced magnetic force.

B.5 Systematic uncertainty

Table B.1 displays the systematic uncertainties associated with the delivered luminosity. The "normalization" uncertainties are for the visible cross section, σ_{vis}. The "integration" uncertainties are for the integrated luminosity that is calculated using the σ_{vis}. The stability uncertainty is calculated from comparing the relative contributions of pixel tracker layers to the total number of pixel clusters measured in a span of time. From run to run, each pixel layer contribution varies by no more than 1%. It is possible for the rate of high track multiplicity events to exceed the temporary storage capacity of the tracker read-out buffer; the resulting inefficiencies are mainly found in the first barrel layer of the tracker. The "afterglow" refers to background noise associated with electrical excitations in the detector material, and warrants a correction factor to the integrated luminosity.

B.6 Author's contributions

The 2015 PbPb run itself recorded about 1.4 $pb-1$ in integrated luminosity. This integrated luminosity is reconstructed into data on the order of petabytes. Table B.2 presents the 2015 PbPb LHC run luminosity information, and presents for each fill the peak instantaneous luminosity, delivered integrated luminosity, and recorded integrated luminosity. The last column, EffbyLumi, is the ratio of the delivered to recorded integrated luminosities.

	Systematic	correction (%)	uncertainty (%)
Integration	Stability	-	1
	type 1	$7-9$	0.6
	type 2	$0-4$	0.7
	CMS deadtime	-	0.5
	Dynamic Inefficiency	-	0.4
Normalization	XY-Correlations	1.1	1.5
	Beam current calibration	-	0.3
	Ghosts and satellites	-	0.2
	Length scale	-3.2	1.5
	Orbit Drift	-	0.4
	Beam-beam deflection	1.8	0.4
	Dynamic-β	-	0.5
	Total		2.7

Table B.1: Systematic uncertainty during the 2015 pp run [139].

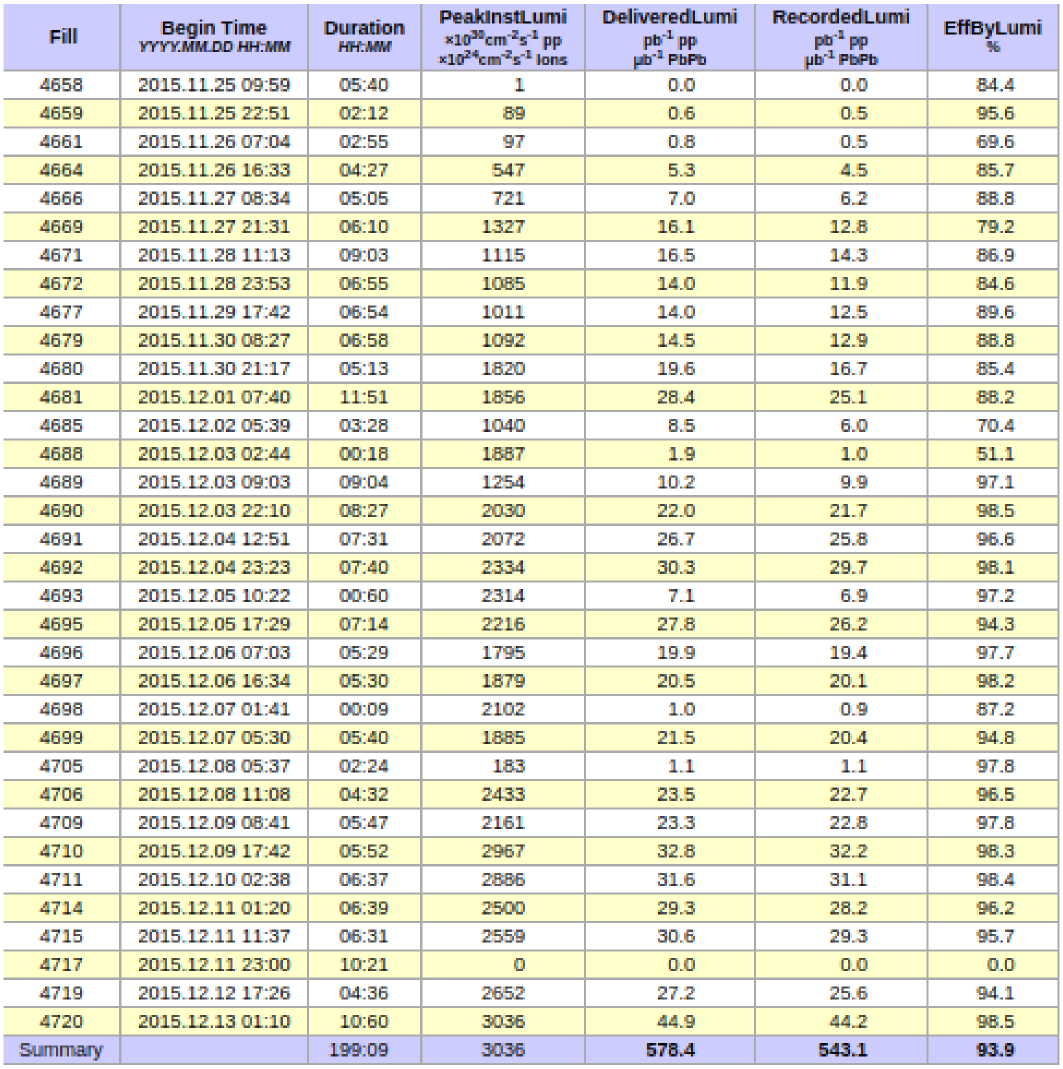

Fill	Begin Time YYYY.MM.DD HH:MM	Duration HH:MM	PeakInstLumi $\times10^{30}$cm^{-2}s^{-1} pp $\times10^{24}$cm^{-2}s^{-1} Ions	DeliveredLumi pb^{-1} pp μb^{-1} PbPb	RecordedLumi pb^{-1} pp μb^{-1} PbPb	EffByLumi %
4658	2015.11.25 09:59	05:40	1	0.0	0.0	84.4
4659	2015.11.25 22:51	02:12	89	0.6	0.5	95.6
4661	2015.11.26 07:04	02:55	97	0.8	0.5	69.6
4664	2015.11.26 16:33	04:27	547	5.3	4.5	85.7
4666	2015.11.27 08:34	05:05	721	7.0	6.2	88.8
4669	2015.11.27 21:31	06:10	1327	16.1	12.8	79.2
4671	2015.11.28 11:13	09:03	1115	16.5	14.3	86.9
4672	2015.11.28 23:53	06:55	1085	14.0	11.9	84.6
4677	2015.11.29 17:42	06:54	1011	14.0	12.5	89.6
4679	2015.11.30 08:27	06:58	1092	14.5	12.9	88.8
4680	2015.11.30 21:17	05:13	1820	19.6	16.7	85.4
4681	2015.12.01 07:40	11:51	1856	28.4	25.1	88.2
4685	2015.12.02 05:39	03:28	1040	8.5	6.0	70.4
4688	2015.12.03 02:44	00:18	1887	1.9	1.0	51.1
4689	2015.12.03 09:03	09:04	1254	10.2	9.9	97.1
4690	2015.12.03 22:10	08:27	2030	22.0	21.7	98.5
4691	2015.12.04 12:51	07:31	2072	26.7	25.8	96.6
4692	2015.12.04 23:23	07:40	2334	30.3	29.7	98.1
4693	2015.12.05 10:22	00:60	2314	7.1	6.9	97.2
4695	2015.12.05 17:29	07:14	2216	27.8	26.2	94.3
4696	2015.12.06 07:03	05:29	1795	19.9	19.4	97.7
4697	2015.12.06 16:34	05:30	1879	20.5	20.1	98.2
4698	2015.12.07 01:41	00:09	2102	1.0	0.9	87.2
4699	2015.12.07 05:30	05:40	1885	21.5	20.4	94.8
4705	2015.12.08 05:37	02:24	183	1.1	1.1	97.8
4706	2015.12.08 11:08	04:32	2433	23.5	22.7	96.5
4709	2015.12.09 08:41	05:47	2161	23.3	22.8	97.8
4710	2015.12.09 17:42	05:52	2967	32.8	32.2	98.3
4711	2015.12.10 02:38	06:37	2886	31.6	31.1	98.4
4714	2015.12.11 01:20	06:39	2500	29.3	28.2	96.2
4715	2015.12.11 11:37	06:31	2559	30.6	29.3	95.7
4717	2015.12.11 23:00	10:21	0	0.0	0.0	0.0
4719	2015.12.12 17:26	04:36	2652	27.2	25.6	94.1
4720	2015.12.13 01:10	10:60	3036	44.9	44.2	98.5
Summary		199:09	3036	**578.4**	**543.1**	**93.9**

Table B.2: Luminosity by CMS fill.

I contributed to CMS luminosity validation and performed studies on the long-term stability of the BRIL luminometers. On a week by week basis, I would examine the data from online and offline luminometers and certify that it met the quality standards of CMS. If the data exhibited non-linear behavior, I would de-certify the corresponding lumi-sections in the BRIL files, which are in the JSON format.

All CMS data have to go through a data certification work flow. Data certification insures that only valid data is used in CMS analyses. Decisions on data certification are recorded in two systems: the DQM Run Registry, shown here in Figure B.3, and the normtag JSON files of the BRIL group. There are occasions when the sub-detectors of CMS might record poor quality data. For example, the software reading out data from the PLT could crash and thus compromise the output. In this case the certification workers would record the lumi sections during which the PLT software crashed. These lumi sections would be removed from the certifying JSON file passed on to the BRIL group. If all the luminometers are malfunctioning, a whole run could be invalidated in the run registry.

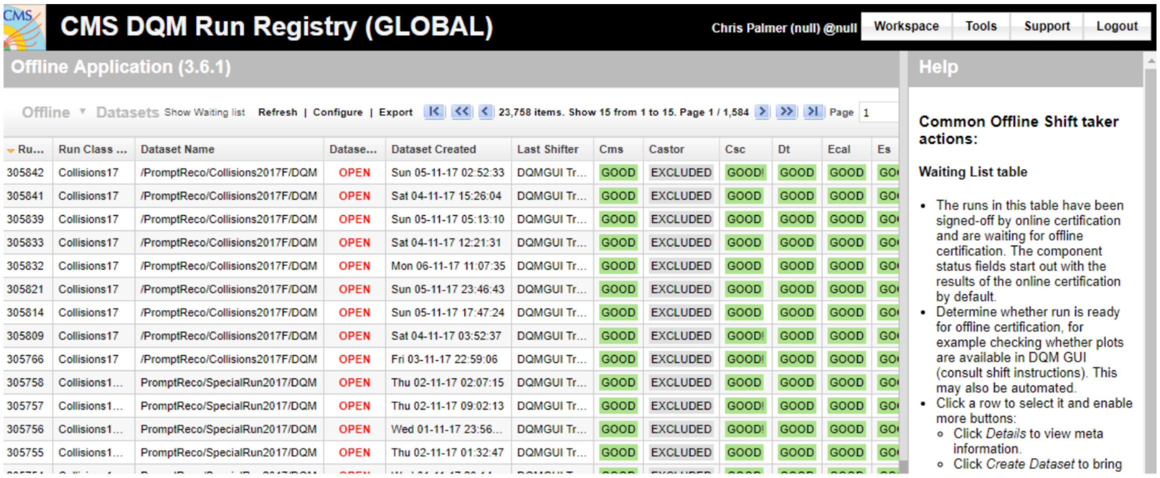

Ru...	Run Class ...	Dataset Name	Datase...	Dataset Created	Last Shifter	Cms	Castor	Csc	Dt	Ecal	Es
305842	Collisions17	/PromptReco/Collisions2017F/DQM	OPEN	Sun 05-11-17 02:52:33	DQMGUI Tr...	GOOD	EXCLUDED	GOOD!	GOOD	GOOD	GO
305841	Collisions17	/PromptReco/Collisions2017F/DQM	OPEN	Sat 04-11-17 15:26:04	DQMGUI Tr...	GOOD	EXCLUDED	GOOD	GOOD	GOOD	GO
305839	Collisions17	/PromptReco/Collisions2017F/DQM	OPEN	Sun 05-11-17 05:13:10	DQMGUI Tr...	GOOD	EXCLUDED	GOOD	GOOD	GOOD	GO
305833	Collisions17	/PromptReco/Collisions2017F/DQM	OPEN	Sat 04-11-17 12:21:31	DQMGUI Tr...	GOOD	EXCLUDED	GOOD	GOOD	GOOD	GO
305832	Collisions17	/PromptReco/Collisions2017F/DQM	OPEN	Mon 06-11-17 11:07:35	DQMGUI Tr...	GOOD	EXCLUDED	GOOD	GOOD	GOOD	GO
305821	Collisions17	/PromptReco/Collisions2017F/DQM	OPEN	Sun 05-11-17 23:46:43	DQMGUI Tr...	GOOD	EXCLUDED	GOOD	GOOD	GOOD	GO
305814	Collisions17	/PromptReco/Collisions2017F/DQM	OPEN	Sun 05-11-17 17:47:24	DQMGUI Tr...	GOOD	EXCLUDED	GOOD	GOOD	GOOD	GO
305809	Collisions17	/PromptReco/Collisions2017F/DQM	OPEN	Sat 04-11-17 03:52:37	DQMGUI Tr...	GOOD	EXCLUDED	GOOD!	GOOD	GOOD	GO
305766	Collisions17	/PromptReco/Collisions2017F/DQM	OPEN	Fri 03-11-17 22:59:06	DQMGUI Tr...	GOOD	EXCLUDED	GOOD!	GOOD	GOOD	GO
305758	Collisions1...	PromptReco/SpecialRun2017/DQM	OPEN	Thu 02-11-17 02:07:15	DQMGUI Tr...	GOOD	EXCLUDED	GOOD	GOOD	GOOD	GO
305757	Collisions1...	PromptReco/SpecialRun2017/DQM	OPEN	Thu 02-11-17 09:02:13	DQMGUI Tr...	GOOD	EXCLUDED	GOOD!	GOOD	GOOD	GO
305756	Collisions1...	PromptReco/SpecialRun2017/DQM	OPEN	Wed 01-11-17 23:56...	DQMGUI Tr...	GOOD	EXCLUDED	GOOD!	GOOD	GOOD	GO
305755	Collisions1...	PromptReco/SpecialRun2017/DQM	OPEN	Thu 02-11-17 01:32:47	DQMGUI Tr...	GOOD	EXCLUDED	GOOD	GOOD	GOOD	GO

Common Offline Shift taker actions:

Waiting List table

- The runs in this table have been signed-off by online certification and are waiting for offline certification. The component status fields start out with the results of the online certification by default.
- Determine whether run is ready for offline certification, for example checking whether plots are available in DQM GUI (consult shift instructions). This may also be automated.
- Click a row to select it and enable more buttons:
  - Click *Details* to view meta information.
  - Click *Create Dataset* to bring

Figure B.3: CMS Run Registry.

In addition to data certification, I reviewed the long-term stability of the BRIL luminometers during the 2015 and 2016 proton-proton runs. Stability refers to the comparative performance of the different luminometers. Ideally, the ratio of the instantaneous luminosity reported by separate luminometers should be a constant ratio, but in fact there is a tendency for this ratio to drift as a result of radiation damage to the luminometers. This drift can be seen in plotting the average ratio as a function of interaction rate and of the different measures of LHC time: runs, lumi-sections, and bunch-crossings. Instantaneous luminosity, in theory, should be independent of machine conditions like acceptance and efficiency. Figure B.4 records the sum of the delivered and recorded integrated luminosity for each day of the 2015 PbPb run.

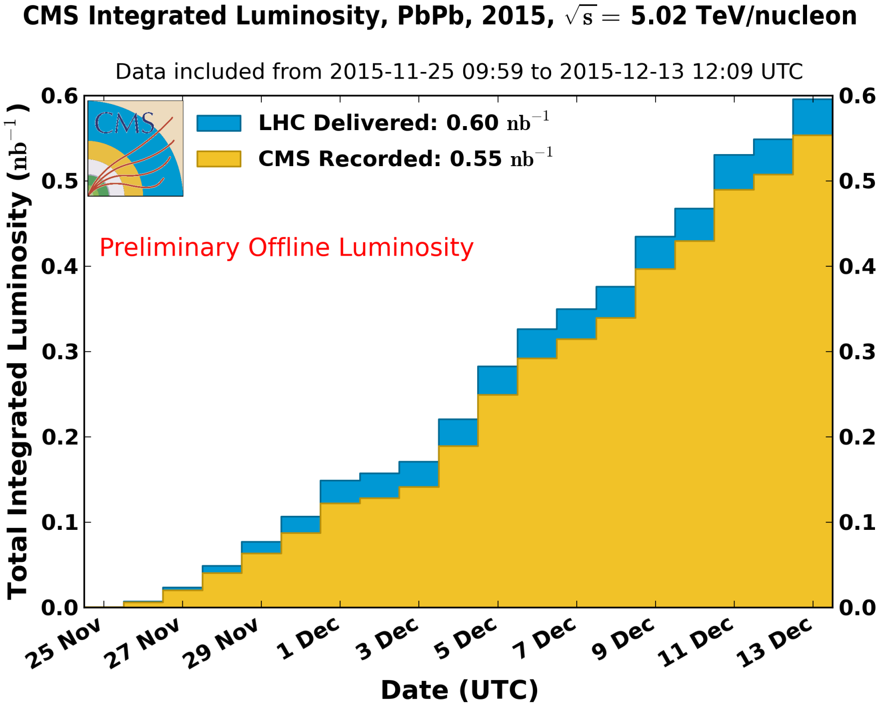

Figure B.4: CMS luminosity during the 2015 PbPb run.

Figure B.5 is the CMS-recorded integrated luminosity for each proton-proton era of the LHC. Notice that as the collision energy increases, the recorded luminosity grows at a steeper and steeper rate. This acceleration in the recorded luminosity is consistent with the higher multiplicity of the high energy collisions. As the LHC pushes the energy frontier, high quality luminosity analyses will become even more fundamental for the continued performance of CMS. The "High Luminosity Large Hadron Collider" (HL-LHC) is a project to increase the design luminosity of LHC by an order of magnitude by 2025. To fully leverage the power of this increased luminosity, particularly for studying possible anomalous couplings, CMS must continue providing measures of luminosity with tightly controlled systematic uncertainty.

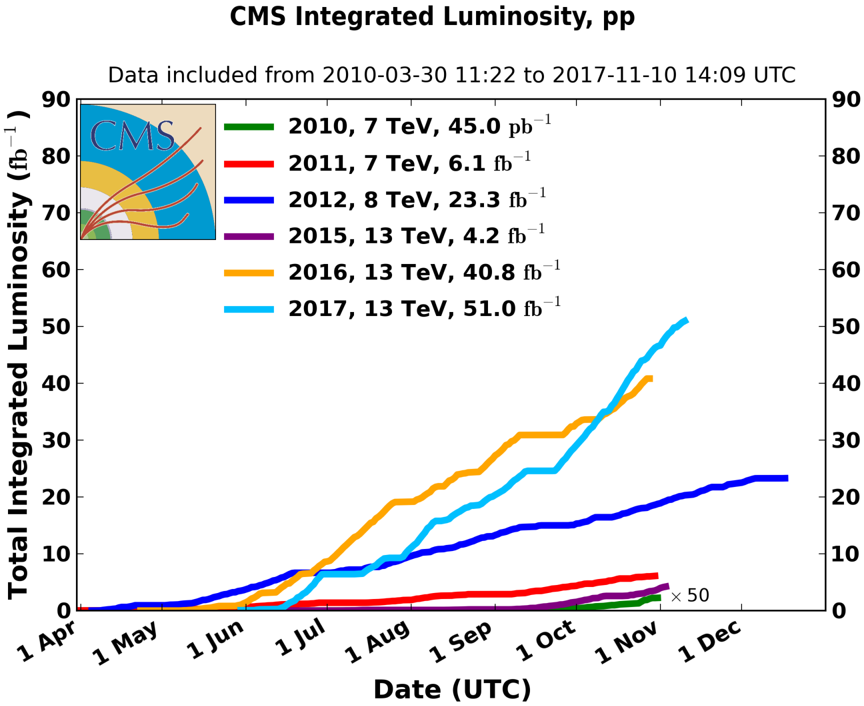

Figure B.5: Total integrated luminosity for the various pp periods from 2010 until 2017.